DIGITAL TRANSFORMATION OF MEDICAL IMAGING: FROM QUANTITATIVE DIAGNOSTIC TO SURGICAL TRAINING

Riccardo Forni

September 2025

Department of Engineering, School of Technology
Reykjavík University

Ph.D. Dissertation

ISBN: 978-9935-539-91-5 Electronic version

ISBN: 978-9935-539-90-8 Print version

ORCID Riccardo Forni

Digital Transformation of Medical Imaging: from quantitative diagnostic to surgical training

by

Riccardo Forni

Dissertation submitted to the Department of Engineering, School of Technology
at Reykjavík University in partial fulfillment
of the requirements for the degree of
Doctor of Philosophy

September 2025

Thesis Committee:

Paolo Gargiulo, Supervisor
Professor, Reykjavík University, Iceland

Cristiana Corsi, Co-Supervisor
Associate Professor, University of Bologna, Italy

Emanuele Domenico Giordano, Co-advisor
Associate Professor, University of Bologna, Italy

Magnus Kjartan Gislason, Co-advisor
Associate Professor, Reykjavik University, Iceland

Paolo Bifulco, Examiner
Professor, Federico II University of Naples, Italy

The undersigned hereby certify that they recommend to the Department of Engineering, School of Technology, Reykjavík University, that this dissertation entitled **Digital Transformation of Medical Imaging: from quantitative diagnostic to surgical training**, submitted by **Riccardo Forni**, be accepted as partial fulfilment of the requirements for the degree of **Doctor of Philosophy (Ph.D.) in Engineering**

.....
date

.....
Paolo Gargiulo, Supervisor
Professor, Reykjavík University, Iceland

.....
Cristiana Corsi, Co-Supervisor
Associate Professor, University of Bologna, Italy

.....
Emanuele Domenico Giordano, Co-advisor
Associate Professor, University of Bologna, Italy

.....
Magnus Kjartan Gislason, Co-advisor
Associate Professor, Reykjavik University, Iceland

.....

Paolo Bifulco, Examiner
Professor, Federico II University of Naples, Italy

.....
date

.....
Riccardo Forni
Doctor of Philosophy

Digital Transformation of Medical Imaging: from quantitative diagnostic to surgical training

Riccardo Forni

September 2025

Abstract

Medical imaging is the prominent way of knowing internal structure, morphology and functional aspects of a living human body and its widely adopted in clinical practice to diagnose, support and plan treatments. This thesis explores the digital transformation of medical imaging, demonstrating how pixel-intensity analysis and advanced computational methodologies can enhance diagnostic precision and support surgical training. Leveraging data-rich imaging modalities such as computed tomography (CT) and infrared imaging, this work develops and validates quantitative pipelines to extract robust imaging biomarkers and reconstruct anatomically accurate models for both clinical and educational purposes.

From a diagnostic perspective, novel radiodensitometric and radiomic techniques were applied across three clinical domains. First, CT-based quantitative analysis was used to characterize skeletal muscle aging, introducing biomarkers of sarcopenia and fat infiltration. Second, the concept of "virtual cardiac histology" was developed, where high-dimensional radiomic features from cardiac CT enabled the non-invasive differentiation of healthy myocardium from pathological conditions, including hypertrophic cardiomyopathy (HCM) and acute myocardial infarction (AMI). Third, automated meibography analysis was proposed to quantify morphological changes in Meibomian glands from infrared eyelid imaging, offering objective metrics for ocular surface diseases.

From an educational and surgical standpoint, this research introduces the Radio Anatomical Interactive Library (RAIL), an innovative platform that integrates clinical imaging data, 3D reconstructions, and mixed reality tools to support anatomical learning, preoperative planning, and surgical rehearsal. By combining radiological data with immersive technologies, RAIL enhances comprehension of complex anatomies and promotes interactive, case-based training.

Collectively, the studies presented demonstrate that pixel-level analysis of medical images can yield reproducible and clinically meaningful biomarkers, bridging the gap between qualitative interpretation and quantitative, data-driven diagnostics. This thesis highlights the potential of integrating AI-based radiomics, 3D visualization, and extended reality into the healthcare continuum, enabling personalized diagnostics, improving training efficiency, and advancing the paradigm of precision medicine.

Keywords: Medical Imaging, Machine Learning, Aging, Cardiac Diseases, Computed Tomography, Ophthalmology, Surgical Training, 3D Radiology

Stafræn umbreyting læknisfræðilegra mynda: frá mælanlegri greiningu til þjálfunar fyrir skurðaðgerðir

Riccardo Forni

september 2025

Útdráttur

Læknisfræðileg myndgreining er aðal aðferðin til að skoða innri uppbyggingu, form og starfsemi mannslíkamans og er í dag víða notuð í klínískri starfsemi til greiningar og skipulagningar meðferða. Þessi doktorsritgerð nýtir eiginleika stafrænnar umbreytingar læknisfræðilegra mynda og sýnir hvernig notkun á birtugildi myndpunkta með háþróuðum tölvuaðferðum geta aukið nákvæmni greininga og stutt við þjálfun í skurðaðgerðum. Með því að nýta gagnaríkar myndgreiningaraðferðir eins og sneiðmyndatöku (CT) og innrauðar myndir, eru þróaðar og sannreyndar magngreiningarlínur til að draga út áreiðanleg lífmerki úr myndum og endurskapa nákvæm líkön af líffærum til klínískra og fræðslutengdra nota. Frá greiningarsjónarmiði voru nýjar geislaþéttni- og geislaeininga (radiomics) líkön notuð í þremur klínískum vandamálum. Í fyrsta lagi var notuð CT magngreining til að lýsa öldrun beinagrindarvöðva með lífmerkjum sem greina vöðvarýrnun og fituinnskot. Í öðru lagi var þróað hugtakið „sýndarhjartavefjalíffræði“, þar sem þrívíddarlíkan af hjarta-CT myndum gerði kleift að greina heilbrigðan hjartavöðva frá sjúkum eins og ofvöxt í hjartavöðva (e. hyperthrophic cardiomyopathy) og bráðu hjartadrepi (e. acute myocardial infarction). Í þriðja lagi var þróuð sjálfvirk magngreining á formbreytingum í Meibomian-kirtlum augans (e. quantitative meibography) með notkun innrauðra mynda af augnlokum, sem býður upp á hlutlæg viðmið fyrir greiningu á sjúkdómum á yfirborði augans. Á fræðslu- og skurðaðgerðarsviði er kynnt RadioAnatomical Interactive Library (RAIL), sem er vettvangur sem sameinar klínískar upplýsingar, þrívíddarmódel og sýndarveruleika til að styðja við kennslu í líffærafræði, við undirbúning aðgerða og við æfingar. Með því að sameina myndgreiningu við gagnvirka tækni, auðveldar RAIL skilning á flóknum sjúkdóma- og líffæra fyrirbærum og stuðlar að öruggari þjálfun fyrir meðferð á sjúkdómum. Samantekið sýna þessar rannsóknir að útvíkkuð greining á myndpunktum getur skilað klínískt mikilvægum lífmerkjum og brúað bilið á milli eigindlegrar túlkunar og magnbundinnar, gagnadrifinnar greiningar. Ritgerðin undirstrikar möguleika þess að samþætta notkun gervigreindargagna við túlkun stafrænna læknisfræðilegra upplýsinga, þrívíddarmódela og sýndarveruleika í heilbrigðisþjónustu, með áherslu á persónusniðna greiningu, bætta þjálfun heilbrigðistarfsfólks og tækniframfarir í lækningum.

Efnisorð: Læknamyndgreining, Tölvulærdómur, Öldrun, Tölvusneiðmyndataka, Augnlækningar, Skurðlæknaþjálfun, Þrívíddarmyndgreining

Contents

List of Figures

List of Tables

Acknowledgements

Publications Presented in the Thesis

Most of the text of the present PhD thesis has been adapted from some of the publications, of which I, Riccardo Forni, am an author. I am affiliated with the Institute of Biomedical and Neural Engineering in the Engineering Department of Reykjavik University, Iceland and to with the Department of Electrical, Electronic, and Information Engineering "Guglielmo Marconi", Alma Mater Studiorum, University of Bologna, Italy.
All publications have been submitted for peer-review in their respective journals or conferences during the duration of my doctoral studies. All of them are published and are available online, some of them, as indicated, are currently under the peer-review process.
I fully acknowledge that these papers are written in collaboration with my co-authors and that this thesis therefore contains some text and concepts that were conceived in collaboration. I hereby confirm that the inclusion of all previously published text was written either by myself and/or included here with the permission of my co-authors.
The publications list follows a chronological order starting from the most recent:

- Forni, R., Corsi, C., & Gargiulo, P. (2025, September). Multi-Domain Radiomics Analysis of Virtual Cardiac Histology Samples: A Predictive Model for Hypertrophic Cardiomyopathy. In 2025 Computing in Cardiology (CinC). IEEE.

- Forni, R., Colacino, A., Punzo, B., Cavaliere, C., Franzese, M., Ulfarsson, A. O., ... & Gargiulo, P. (2025). Virtual cardiac histology: Towards a radiodensitometric characterization of left ventricular cardiac muscle in healthy and pathological conditions. Computer Methods and Programs in Biomedicine, 108876.

- Forni, R., Maruotto, I., Zanuccoli, A., Nicoletti, R., Trimigno, L., Corbellino, M., ... & Gargiulo, P. (2025). Advancing Meibography Assessment and Automated Meibomian Gland Detection Using Gray Value Profiles. Diagnostics, 15(10), 1199.

- Forni, R., Gargiulo, P., Boretti, G., Quadrelli, M., Baccaglini, T., Morra, A., ... & Masiero, S. (2024). The Impact of Persevering Home Full-Body In-Bed Gym Exercise on Body Muscles in Aging: A Case Report by Quantitative Radio-Densitometric Study Using 3D and 2D Color CT. Diagnostics, 14(24), 2808.

- Forni, R., Gelormini, C., Corsi, C., & Gargiulo, P. (2023, October). Virtual Histology of the Heart Through CT Imaging: Preliminary Results of a Novel Noninvasive Approach for Cardiac Tissue Characterization. In 2023 Computing in Cardiology (CinC) (Vol. 50, pp. 1-4). IEEE.

Prologue

This thesis provides novel approaches and algorithms to study pixels-based features from Computed Tomography, mainly, and Infrared Imaging and illustrates different applications where medical images play a crucial role as diagnostic, prognostic and educational tool. The researches were conducted principally at the Institute of Biomedical and Neural Engineering at Reykjavik University and in collaboration with Alma Mater Studiourum - University of Bologna, SynLab Hospital both in Naples and in Padua and Espansione Group, an Italian MedTech company. This dissertation will focus mainly on the use of local and global pixels brightness variation in medical images to characterize the underlying tissue in aging and cardiac diseases, to detect and quantify morphologies in Meibomian Glands Deficiency and in the reconstruction of patient specific anatomies for medical education and training. The remainder of this thesis is structured in six chapters:

- **Chapter 1:** This chapter introduces medical imaging, its history, physical and functioning principles, the technological advancement and the transition towards digital technology. A brief introduction of the state-of-art clinically used modalities and their diagnostic and prognostic applications. The introduction is tailored to biomedical engineering aspects of medical images and provides a extensive overview of basic concepts used later on in the manuscript.

- **Chapter 2:** This chapter investigates how aging impacts skeletal muscle composition using quantitative computed tomography (CT) imaging. By analyzing Hounsfield Unit (HU) distributions and segmenting muscle and fat tissues, the study quantifies key changes in muscle quality such as fat infiltration (myosteatosis) and density reduction. The approach goes beyond volumetric measures, introducing radiodensitometric biomarkers that capture subtle structural degradation associated with aging. These markers have potential clinical applications in assessing sarcopenia and frailty, offering an objective tool for population studies and longitudinal muscle health monitoring.

- **Chapter 3:** This chapter introduces a novel approach termed "virtual cardiac histology," which leverages radiomics to extract high-dimensional textural and statistical features from cardiac CT images. Focusing on the left ventricular myocardium, the study investigates how image-derived biomarkers can non-invasively characterize underlying tissue pathology. By comparing healthy subjects with those affected by hypertrophic cardiomyopathy (HCM) and acute myocardial infarction (AMI), the chapter demonstrates how radiomic signatures, derived from pixel intensity distributions and texture analysis, can distinguish

fibrotic, hypertrophic, and necrotic changes in myocardial tissue. Advanced feature selection techniques and machine learning classifiers are employed to build predictive models, while SHAP-based interpretability is used to elucidate which imaging features contribute most to classification. This work bridges the gap between radiological imaging and histopathological insight, offering a non-invasive alternative for myocardial tissue characterization in both clinical diagnostics and research settings.

- **Chapter 4:** This chapter presents a novel automated method for analyzing infrared meibography images of the eyelids to quantify Meibomian gland morphology. The technique involves intensity-based segmentation and morphological processing to detect gland structures and assess their atrophy, which is a hallmark of Meibomian Gland Dysfunction (MGD) and dry eye disease. The pipeline is designed to ensure reproducibility and scalability, addressing limitations of subjective clinical grading. Quantitative descriptors such as gland length, area, and dropout percentage are extracted, offering objective metrics for diagnosis, disease monitoring, and treatment evaluation. This study illustrates how targeted image analysis can support ophthalmic diagnostics through accessible and non-invasive tools.

- **Chapter 5:** This chapter explores the integration of digital imaging and mixed reality technologies into surgical training and preoperative planning. Patient-specific CT data are processed to generate high-resolution 3D anatomical models, which are then used in immersive environments to support spatial understanding and rehearsal of complex procedures. The chapter describes a workflow that combines segmentation, model optimization, and deployment on platforms such as augmented or virtual reality headsets. It discusses educational and clinical use cases where enhanced visualization can improve procedural confidence and reduce intraoperative uncertainty. The approach represents a step toward personalized surgical education, leveraging imaging data not only for diagnostics but also for hands-on training.

- **Chapter 6:** The final chapter synthesizes the findings across all studies, emphasizing the unifying theme of leveraging pixel-level intensity data to derive meaningful clinical insights. It reflects on the translational potential of imaging biomarkers, their role in personalized diagnostics, and the implications for future digital healthcare. Common methodological frameworks and limitations are also critically evaluated.

Chapter 1

Introduction

1.1 Computed Tomography: the first imaging modality

The history of medical imaging begins with a moment of serendipity. In 1895, German physicist Wilhelm Conrad Röntgen, while experimenting with cathode rays, observed that a fluorescent screen across his darkened lab began to glow—even though the cathode ray tube was shielded. He had discovered a new type of invisible radiation, capable of passing through flesh and revealing the hidden structures of the human body. He called them X-rays, "X" standing for the unknown.

Röntgen's discovery sent shockwaves through science and medicine. Within weeks, physicians were using X-rays to look inside the human body without making a single incision. The first X-ray image of a human, a photograph of Röntgen's wife Bertha's hand, wedding ring starkly visible around ghostly bones, marked the birth of diagnostic radiology [1].

But while X-rays revolutionized diagnostics, they had their limits. Traditional radiographs are two-dimensional projections, compressing complex anatomy into flat images. Structures could overlap, and depth information was lost. For decades, scientists and clinicians dreamed of ways to go further, to see not just shadows, but slices. That dream became reality in the early 1970s, thanks to the convergence of physics, mathematics, and computing.

Enter Godfrey Hounsfield, a British engineer at EMI (famous for producing Beatles records), who hypothesized that by taking multiple X-ray measurements around an object, one could reconstruct a detailed internal image using a computer [2]. In parallel, Allan Cormack, a South African physicist, had already developed the mathematical theory behind this idea, publishing his results in the 1960s, though they went largely unnoticed at the time [3].

In 1971, Hounsfield unveiled the first clinical CT scanner, and soon after, the first CT scan of a patient's brain revealed a previously undetectable tumor. This marked a paradigm shift in medical imaging: the era of computed tomography. For their pioneering contributions, Hounsfield and Cormack shared the 1979 Nobel Prize in Physiology or Medicine.

1.2 Physical Foundations and Clinical Roles of Modern Imaging Modalities

Medical imaging technologies exploit various physical principles to non-invasively visualize the internal structures and functions of the human body [4]. By categorizing these modalities according to their underlying physics, we gain a clearer understanding of their respective strengths, limitations, and clinical applications. The principal physical mechanisms employed in medical imaging include ionizing radiation, magnetic polarization, acoustic wave reflection, and thermal radiation.

1.2.1 Radiation-Based Imaging Modalities

Ionizing radiation forms the foundation of several widely used medical imaging techniques. These modalities exploit the interactions between high-energy photons and matter, such as absorption, scattering, and emission, to generate images. Depending on how the radiation interacts with different tissues or with radioactive tracers, this category includes both anatomical and functional imaging techniques. The degree of interaction is influenced by tissue composition and photon energy, providing the basis for contrast in radiographic, tomographic, and nuclear medicine applications.

1.2.1.1 X-ray Radiography and Computed Tomography (CT)

X-ray radiography and CT imaging are both based on the differential attenuation of ionizing radiation as it passes through the body. X-rays are high-energy photons generated by accelerating electrons against a metallic target [1]. The resulting beam penetrates the body, and the degree of attenuation is dictated by the linear attenuation coefficient μ, which depends on tissue density, atomic composition, and photon energy [5].

- **Radiography** captures two-dimensional projection images, with contrast primarily arising from variations in tissue density (e.g., bone vs. soft tissue). It is fast, accessible, and widely used in orthopedics and chest imaging.
- **CT** extends this concept into three dimensions, reconstructing cross-sectional images from multiple projections acquired around the patient. CT provides detailed anatomical resolution and is essential in trauma, oncology, and vascular imaging. The use of iodinated contrast media enhances soft tissue differentiation by exploiting the energy-dependent photoelectric effect.

1.2.1.2 Nuclear Medicine: PET and SPECT

Positron Emission Tomography (PET) and Single Photon Emission Computed Tomography (SPECT) rely on the detection of gamma photons emitted from radiotracers administered to the patient. These modalities provide functional and molecular imaging capabilities, offering insights into physiological and metabolic processes [6].

- **PET** detects coincident gamma photons produced by positron annihilation, allowing for high-sensitivity localization of tracer activity (e.g., ^{18}F-FDG in oncology).
- **SPECT** measures single gamma photons emitted from isotopes like ^{99m}Tc, using rotating gamma cameras to reconstruct tomographic images.

Both PET and SPECT are essential for assessing tissue viability, perfusion, receptor binding, and disease progression, particularly in neurology, and oncology [7], [8].

1.2.2 Magnetic Polarization-Based Imaging

Magnetic resonance imaging (MRI) is based on the principles of nuclear magnetic polarization and resonance. When placed in a strong external magnetic field, certain atomic nuclei align with the field and can be excited by specific radiofrequency pulses. The emitted signals as they return to equilibrium are sensitive to tissue-specific parameters and are used to generate high-resolution, contrast-rich images, particularly suited for soft tissue characterization.

1.2.2.1 Magnetic Resonance Imaging (MRI)

Magnetic Resonance Imaging (MRI) exploits the nuclear magnetic properties of hydrogen protons, which possess intrinsic spin and a magnetic moment. When placed within a strong static magnetic field (B_0), these protons align either parallel or antiparallel to the field, resulting in a net magnetization along the longitudinal axis. Application of a radiofrequency (RF) pulse at the Larmor frequency causes the net magnetization vector to tilt into the transverse plane. As the RF pulse is turned off, the protons undergo relaxation—characterized by T1 (longitudinal) and T2 (transverse) decay, emitting RF signals that are spatially encoded using magnetic field gradients [9]. The signal intensity in MRI depends on several tissue-specific parameters, including proton density and relaxation times (T1 and T2), enabling exquisite soft tissue contrast without ionizing radiation. By varying pulse sequences and acquisition protocols, MRI can highlight different anatomical and physiological properties, including perfusion, diffusion, and blood oxygenation. Functional MRI (fMRI) and spectroscopy expand MRI's utility into brain mapping and metabolic analysis [10].

1.2.3 Acoustic Reflection-Based Imaging

Acoustic-based imaging utilizes the propagation and reflection of high-frequency sound waves through biological tissues. Variations in acoustic impedance at tissue boundaries cause partial reflections, which are detected and converted into real-time images. The fundamental physics of wave propagation, reflection, and Doppler shift enables both structural and hemodynamic assessment, making ultrasound a versatile and safe diagnostic tool.

1.2.3.1 Ultrasound Imaging

Ultrasound imaging utilizes high-frequency sound waves (typically 2–15 MHz) that propagate through the body and reflect at interfaces between tissues with different acoustic impedances [11]. The time delay and amplitude of returning echoes are processed to construct real-time images.

Ultrasound is safe, cost-effective, and portable, making it a first-line imaging tool in obstetrics, cardiology, and emergency medicine [12]. Doppler techniques enable the assessment of blood flow and vascular conditions, while advanced modes like elastography and contrast-enhanced ultrasound extend its diagnostic capabilities [13].

1.2.4 Thermal Radiation-Based Imaging

All objects emit electromagnetic radiation as a function of their temperature. Infrared thermography captures this naturally emitted thermal radiation from the body surface,

usually in the mid-infrared range. Although it does not penetrate deep into tissues, it allows for indirect assessment of physiological processes by mapping temperature distribution, with potential clinical relevance in inflammatory and vascular conditions [14].

1.2.4.1 Infrared Thermography

Infrared imaging detects the natural thermal radiation emitted by the body, typically in the wavelength range of 8–14 μm. The intensity of emitted infrared radiation correlates with surface temperature, which can reflect underlying physiological processes such as inflammation, vascular disorders, or abnormal perfusion.

Although not a primary diagnostic tool, infrared thermography is non-contact and its radiation-free nature makes it particularly suitable for continuous or remote monitoring scenarios [15].

Summary

Each imaging modality, rooted in a distinct physical principle, provides complementary information. Radiation-based methods excel at anatomical detail and functional imaging via tracers, while MRI provides rich soft tissue contrast without ionizing exposure. Ultrasound offers dynamic and portable imaging, and infrared thermography reveals surface temperature patterns. The integration of these modalities, either sequentially or in hybrid devices such as PET/CT and PET/MRI, enhances diagnostic accuracy and deepens our understanding of human physiology and pathology. A summary of the major clinical application is reported in Table 1.1

1.3 From Photographic Plates to Pixel Matrices: The Digital Reinvention of Medical Imaging

The acquisition of medical images has undergone a profound transformation—from analog, impression-based techniques to digital, data-driven workflows. This evolution, driven by advances in physics, detector technology, and computational capacity, has enhanced the resolution, reproducibility, and clinical relevance of imaging. As the foundational stage of the imaging pipeline, acquisition converts physical interactions into structured digital representations that serve as substrates for diagnosis, quantitative analysis, and clinical decision-making.

Early imaging modalities, such as conventional X-ray radiography, relied on analog media—primarily photographic films—to capture variations in X-ray attenuation across the body. These images offered high spatial resolution but suffered from limited dynamic range, poor contrast flexibility, and challenges in storage and retrieval [16]. Although revolutionary in their time, analog systems lacked the capability for real-time analysis and digital enhancement.

The digital era of imaging was catalyzed by the development of computed tomography (CT) in the early 1970s. Godfrey Hounsfield and Allan Cormack demonstrated that by collecting multiple X-ray projections from different angles and applying tomographic reconstruction algorithms, it was possible to reconstruct cross-sectional images of internal anatomy with unprecedented clarity [2]. This shift marked a conceptual departure: image formation became an active process of computational inference rather

Table 1.1: Clinical applications of medical imaging modalities categorized by physical principles

Physical Principle	**Imaging Modalities**	**Main Clinical Applications**
Ionizing Radiation	X-ray Radiography	Fracture detection, dental imaging, chest diseases (e.g., pneumonia, tuberculosis), mammography
	Computed Tomography (CT)	Trauma assessment, stroke diagnosis, tumor detection and staging, lung and cardiac imaging, vascular evaluation (CT angiography)
	PET, SPECT	Oncology (tumor metabolism and spread), cardiology (myocardial perfusion), neurology (dementia, epilepsy), infection/inflammation detection
Magnetic Polarization	Magnetic Resonance Imaging (MRI)	Soft tissue imaging (brain, muscles, joints), neuroimaging, spinal cord assessment, cardiovascular and functional imaging (fMRI, perfusion, spectroscopy)
Acoustic Reflection	Ultrasound (US)	Fetal monitoring, abdominal organ imaging, echocardiography, thyroid and breast evaluation, vascular flow analysis (Doppler US)
Thermal Radiation	Infrared Thermography	Peripheral vascular disease, diabetic foot monitoring, inflammation and infection screening, adjunct breast cancer evaluation (experimental)

than a passive photographic recording. A pivotal aspect of the digital transformation in medical imaging lies in the ability to transduce physical signals into digital representations suitable for computational analysis. Early analog detectors have been progressively replaced by digital sensors, including photostimulable phosphor plates (used in computed radiography), solid-state detectors, and flat-panel detectors based on amorphous silicon or complementary metal-oxide semiconductor (CMOS) technology [17]. These detectors convert incident X-ray photons signals directly into digital signals using scintillators and photodiodes, enabling real-time image acquisition and reduced radiation exposure. The direct capture of digital signals has enabled seamless integration with digital storage and processing pipelines, eliminating the need for film scanning and manual archiving. Modern CT systems use solid-state detectors (e.g., scintillator-photodiode arrays or flat-panel detectors) to convert incident X-rays into electrical signals, which are digitized and reconstructed into volumetric datasets. This digital pipeline enables real-time visualization, multiplanar reformations, and quantitative analyses such as Hounsfield Unit (HU)-based tissue characterization [18].

In magnetic resonance imaging (MRI), the acquisition process is fundamentally different. MRI collects signal data in the frequency domain, known as *k-space*, where each point represents a spatial frequency component of the image. The raw signal is acquired using radiofrequency (RF) receiver coils and is digitized via analog-to-digital converters. Spatial encoding is achieved using magnetic field gradients, and final images are reconstructed using Fourier transformation [19], [20]. This approach allows for exquisite soft tissue contrast and flexible contrast modulation through variation of pulse sequences (e.g., T1-, T2-weighted, diffusion, and perfusion imaging).

Ultrasound imaging systems utilize piezoelectric transducers to emit high-frequency sound waves and detect their echoes as they reflect from tissue interfaces with differing acoustic impedance. Modern ultrasound employs electronic beamforming and real-time digital signal processing to produce dynamic 2D and 3D representations of anatomy and hemodynamics. Doppler techniques further enable the visualization of blood flow and vascular resistance [21].

In nuclear medicine, including positron emission tomography (PET) and single photon emission computed tomography (SPECT), image acquisition involves tracking gamma photons emitted from administered radiotracers. Detectors such as scintillation crystals coupled with photomultiplier tubes or solid-state sensors record these emissions. Events are digitized, spatially localized, and reconstructed into tomographic datasets that reflect physiological or molecular activity rather than purely anatomical structures [6].

The advent of digital technologies has profoundly transformed the landscape of medical imaging, marking a paradigm shift from analog image acquisition and manual interpretation to fully integrated digital workflows. This transformation, referred to as the digitalization of medical imaging, encompasses not only the conversion of analog signals into digital data, but also the implementation of advanced computational tools for storage, analysis, visualization, and clinical integration.

With the rise of digital acquisition, the development of standardized communication protocols became critical. The introduction of the Digital Imaging and Communications in Medicine (DICOM) standard established a universal framework for encoding, storing, and exchanging medical images and associated metadata. DICOM ensures interoperability across imaging modalities and vendor platforms, facilitating the construction of comprehensive and connected imaging ecosystems.

1.3.1 DICOM Format and PACS Systems

The DICOM standard, developed by the American College of Radiology (ACR) and the National Electrical Manufacturers Association (NEMA), defines both the file format and the communication protocols required for the management of medical images. Each DICOM file includes two core components: the image data, typically a matrix of intensity values (e.g., grayscale Hounsfield Units in CT or signal amplitudes in MRI)—and a metadata header containing extensive information such as patient demographics, study identifiers, acquisition parameters, and spatial orientation. These metadata elements are essential for consistent image reconstruction, registration, comparison, and clinical interpretation.

DICOM also supports a range of network services for transmitting and managing imaging workflows:

- **Storage Service**: archives image datasets to a PACS server.
- **Query/Retrieve Service**: locates and accesses prior studies.
- **Worklist Management**: synchronizes imaging orders from the hospital information system (HIS/RIS).
- **Modality Performed Procedure Step (MPPS)**: documents the actual execution of an imaging procedure.

Each digital medical image is composed of a two- or three-dimensional array of elements—pixels or voxels—where each element encodes an intensity value representing a physical property such as X-ray attenuation (CT), signal amplitude (MRI), or tracer concentration (PET) [22]. The size of an image matrix depends on the acquisition protocol and modality, typically ranging from 256×256 to 1024×1024 in 2D, or from 128×128 to 512×512 in volumetric datasets [23]. These matrices are associated with spatial resolution parameters including voxel spacing, slice thickness, and field of view (FOV), which together determine the physical size and anisotropy of each voxel [24].

Image intensities are typically stored using 12-bit to 16-bit depth, enabling 4096 to 65536 grayscale levels, far beyond the display capabilities of standard monitors. In CT imaging, pixel values are expressed in Hounsfield Units (HU), calibrated such that water is set to 0 HU and air to -1000 HU, with bone and metal reaching values above thousands. In MRI, the intensity scale is arbitrary and depends on the pulse sequence, relaxation times, and scanner settings. PET and SPECT images are often quantified in terms of standardized uptake values (SUVs), representing tracer concentration normalized by patient and scan parameters [9], [25], [26].

Understanding image matrix properties is essential for any downstream processing, such as segmentation and registration, as variations in resolution, bit depth, and intensity scaling can introduce bias or affect reproducibility. Proper metadata encoding within DICOM headers ensures that spatial and intensity information is preserved and interpretable across platforms and analysis pipelines.

Closely linked to DICOM is the Picture Archiving and Communication System (PACS), a digital infrastructure that handles the storage, retrieval, distribution, and visualization of imaging data. PACS systems interface with acquisition modalities (CT, MRI, ultrasound, etc.) and integrate with hospital and radiology information systems (HIS/RIS) to support a seamless clinical workflow [27]. They also serve as

the foundation for image-based decision-making, enabling radiologists, clinicians, and specialists to access high-resolution datasets from any network-connected workstation.

A typical PACS ecosystem consists of [28]:

1. **Imaging modalities** (e.g., CT, MRI, PET, ultrasound) that generate DICOM-compliant digital images.
2. **A secure network** for transmitting imaging data and metadata.
3. **Archive servers** for long-term storage and redundancy.
4. **Viewing workstations** equipped with diagnostic tools for image interpretation and reporting.

Modern PACS systems have evolved beyond simple image storage. They now support advanced functions such as dynamic reconstructions, multiplanar reformatting, 3D visualization, and integration with AI-assisted diagnostic tools. Moreover, enterprise-level PACS increasingly utilize Vendor Neutral Archives (VNAs) and cloud-based solutions to promote interoperability, scalability, and secure data access across institutional and geographic boundaries.

Within this framework, digital medical images form the substrate for all computational analyses presented in this thesis. The research builds upon this infrastructure to extract quantitative features and construct patient-specific models. These efforts aim to advance the use of digital imaging in precision diagnostics, biomechanical simulation, and surgical planning, contributing to the broader evolution of data-driven, patient-specific clinical care.

1.4 Segmentation as a Gateway to Anatomical Understanding

Segmentation is a central task in medical image analysis, enabling the delineation of anatomically or functionally meaningful structures from background tissue. By isolating regions of interest, segmentation allows for precise quantification, shape analysis, feature extraction, and subsequent diagnostic or prognostic modeling. Rather than organizing the topic as a taxonomy of algorithms, segmentation can be more intuitively introduced by considering the two primary principles that underpin most methods: (1) the spatial coherence of image regions, and (2) the characteristic gray-level distributions of specific tissues or structures [29].

The first principle relies on the observation that anatomical structures are typically formed by pixels or voxels that are spatially contiguous and exhibit similar local appearance. This leads to segmentation strategies based on *spatial proximity* and *regional homogeneity*, where neighboring elements are grouped together if they fulfill a criterion of similarity. Classical methods under this category include:

- **Region Growing**, which iteratively aggregates pixels starting from seed points, expanding the region based on predefined similarity thresholds [30].
- **Watershed Algorithms**, which interpret the image as a topographic surface and segment it by simulating the flooding of basins from local minima [31].

- **Connected Component Labeling**, often used after binary thresholding to separate distinct clusters of similar intensity [32].

- **Clustering-based methods** such as *k-means* or *mean shift*, which assign pixels to groups based on proximity in feature space (e.g., intensity, texture, or coordinates) [33], [34].

These approaches are particularly useful in cases where structural boundaries are defined by smooth transitions or continuous regions, such as parenchymal organs in abdominal imaging or ventricular cavities in cardiac MRI.

The second principle centers on the idea that different tissues or pathologies often exhibit characteristic *intensity values* in medical images. For instance, in CT imaging, bone, muscle, fat, and air can be readily distinguished based on their Hounsfield Unit (HU) ranges. Similarly, in MRI, tissue contrast is governed by relaxation properties and acquisition parameters, producing distinct signal intensities for cerebrospinal fluid, white matter, or lesions. Segmentation methods leveraging this principle include:

- **Thresholding**, both global and adaptive, which classifies pixels by comparing their intensities to one or more thresholds [35].

- **Histogram-based methods**, which detect peaks in intensity distribution to separate tissues [35].

- **Statistical classifiers**, such as *Gaussian Mixture Models (GMMs)*, *Expectation-Maximization (EM)*, or *Bayesian approaches*, which model the intensity distribution of different classes and assign membership probabilities [36].

- **Level-set methods**, which use evolving contours driven by intensity gradients or region-based statistics to delineate boundaries between structures [37], [38].

In practice, these two paradigms are often combined to enhance segmentation performance in the presence of noise, partial volume effects, or anatomical complexity. Hybrid methods, such as Markov Random Fields (MRFs) and Conditional Random Fields (CRFs), incorporate both spatial dependencies and intensity likelihoods into a unified probabilistic framework [39]. Additionally, graph-based methods, such as graph cuts, model segmentation as an energy minimization problem balancing regional fidelity and boundary smoothness [40].

More recently, deep learning-based approaches, particularly convolutional neural networks (CNNs), have revolutionized medical image segmentation by learning complex mappings from image data to labeled regions [41]. Architectures such as U-Net, V-Net, and nnU-Net have demonstrated state of the art performance across a wide range of tasks, leveraging both local texture patterns and global contextual information [42], [43]. These models implicitly encode both proximity and intensity features, and are often trained on large, annotated datasets to generalize across subjects and scanners.

In this thesis, segmentation represents a foundational step, enabling the isolation of anatomical regions of interest from surrounding structures. This facilitates consistent comparison across subjects and time points, and provides a defined spatial context for downstream tasks such as feature extraction, radiomic profiling, or anatomical modeling.

1.5 Applications of Digital Medical Imaging

The digitization of medical imaging has revolutionized healthcare by transforming static images into dynamic, data-rich resources. This evolution has facilitated a multitude of applications across diagnostics, treatment planning, and medical education. Below, we delineate the key domains where digital medical imaging has made significant impacts. A graphical scheme reporting the digital application is drawn in Figure 1.1.

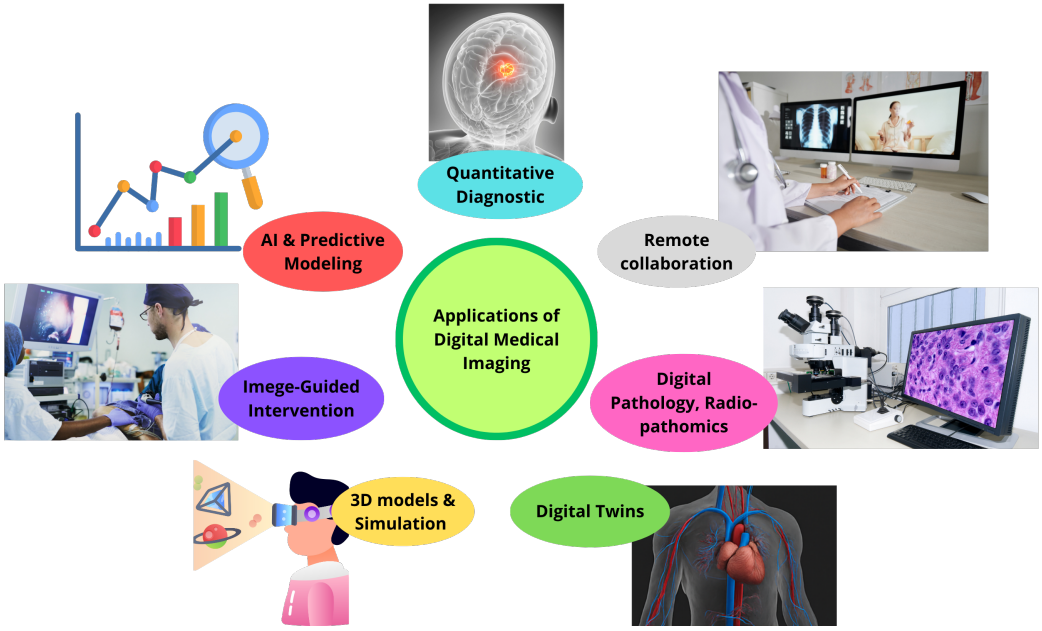

Figure 1.1: Field of Digital Medical Imaging: list of the most important and promising applications of digitalization of imaging in the medical field.

Quantitative Diagnostic The evolution of medical imaging from a purely qualitative modality to a quantitative discipline has significantly enhanced its role in modern diagnostics. Traditionally, image interpretation has relied on visual inspection and subjective assessment by expert radiologists. While this approach remains indispensable, the digitization of medical imaging has enabled the extraction of objective, reproducible, and high-dimensional data, commonly referred to as quantitative imaging biomarkers [44].

Quantitative diagnostics involves the numerical characterization of anatomical, physiological, or pathological features captured in medical images. These features include measurements of shape, size, intensity, volume, texture, and enhancement kinetics. Such parameters can be directly extracted using computational tools or indirectly derived through mathematical modeling and statistical analysis [45].

A key driver of quantitative diagnostics is radiomics, a field that involves high-throughput extraction of large numbers of features from radiological images, followed by feature selection and correlation with clinical outcomes. Radiomic features can capture subtle patterns in tissue heterogeneity that are not apparent to the naked eye, and have been shown to correlate with tumor grade, treatment response, and prognosis in oncology [46], [47].

In oncology, texture and intensity features derived from CT and MRI can be used to non-invasively assess tumor heterogeneity, hypoxia, and angiogenesis [48], [49]. Ra-

diomics has been used in lung, breast, brain, and prostate cancers to predict survival, recurrence risk, and molecular subtypes. The integration of imaging features with clinical, histopathological, and genomic data enables a more comprehensive and individualized diagnostic profile shifting toward precision oncology [50].

In cardiovascular imaging, MRI is the primary tool to assess myocardial tissue composition, detect fibrosis, quantify atherosclerotic plaque burden, and evaluate ventricular function [51]. Hounsfield Unit (HU) in cardiac CT allow for quantification of epicardial fat [52]. Quantitative cine MRI, on the other hand, enables assessment of left ventricular ejection fraction, myocardial strain, and T1/T2 mapping—parameters crucial for diagnosing cardiomyopathies and inflammatory conditions [53].

In musculoskeletal imaging, bone mineral density (BMD) measurements from dual-energy X-ray absorptiometry (DEXA) or quantitative CT are widely used for the diagnosis and monitoring of osteoporosis [54]. MRI-based volume and texture measurements of cartilage and muscle are employed to study osteoarthritis, sarcopenia, and other degenerative disorders. These imaging biomarkers assist clinicians in quantifying disease severity, evaluating response to therapy, and making prognostic predictions [45].

In neurology, quantitative imaging techniques such as voxel-based morphometry (VBM), diffusion tensor imaging (DTI), and quantitative susceptibility mapping (QSM) are employed to assess neurodegeneration, demyelination, and iron deposition in disorders like Alzheimer's disease, multiple sclerosis, and Parkinson's disease [55], [56].

Importantly, the standardization and reproducibility of quantitative measures remain critical for clinical translation. Initiatives such as the Quantitative Imaging Biomarkers Alliance (QIBA) and the Image Biomarker Standardization Initiative (IBSI) have established protocols for feature extraction and validation [57]. These efforts aim to bridge the gap between research-grade quantitative metrics and clinical-grade biomarkers suitable for decision-making.

Overall, quantitative diagnostics transforms medical imaging into a source of structured data, enabling integration with electronic health records, machine learning models, and digital twin platforms. This shift supports a more data-driven, individualized approach to diagnosis, prognosis, and therapeutic guidance across multiple areas of medicine.

These applications are further enhanced by the integration of artificial intelligence and machine learning techniques, which can process large-scale image-derived data and identify complex patterns associated with specific diseases. This thesis contributes to this growing domain by proposing new pipelines for the extraction and interpretation of quantitative imaging biomarkers in both cardiac and musculoskeletal contexts.

Artificial Intelligence and Predictive Modeling The integration of artificial intelligence (AI), particularly deep learning, has revolutionized the field of medical imaging by enabling the automation of complex image interpretation tasks. Convolutional neural networks (CNNs), recurrent neural networks (RNNs), and transformer-based architectures are widely used to perform tasks such as segmentation, lesion detection, tissue classification, and image synthesis with a level of precision approaching expert radiologists [58], [59].

In clinical applications, AI-based models are used to support early diagnosis, assess disease progression, and generate predictive biomarkers. For example, in oncology, deep learning systems can automatically identify tumors on CT and MRI scans, classify

them by histological subtype, and predict treatment response based on radiomic patterns [60]. In cardiology, AI models can estimate ventricular function, detect coronary artery disease, and even simulate functional measures such as fractional flow reserve (FFR) directly from anatomical CT data [61].

AI also facilitates the development of predictive models that integrate imaging features with clinical, genetic, and laboratory data, enabling personalized risk assessment and treatment planning. Furthermore, these models are increasingly embedded into imaging platforms and PACS systems, assisting radiologists through automated triage, prioritization, and report generation [62].

However, challenges remain regarding model generalizability, interpretability, and regulatory validation. Efforts to create standardized datasets and transparent benchmarking frameworks are ongoing to promote safe and equitable AI deployment in clinical imaging [63].

Image-Guided Interventions Preoperative imaging data can be utilized intraoperatively to guide surgical procedures with enhanced precision and confidence. Advances in intraoperative navigation systems allow surgeons to visualize anatomical structures in real time, based on registration with patient-specific preoperative images such as CT or MRI scans. These systems use various tracking technologies—including optical, electromagnetic, or stereophotogrammetric tracking, to correlate surgical tools with 3D anatomical data, creating a dynamic surgical roadmap [64].

In particular, augmented reality (AR) overlays and head-mounted displays are increasingly used to superimpose virtual anatomical structures or planned trajectories directly onto the surgeon's view of the operative field [65]. These technologies are being applied in neurosurgery (e.g., for tumor resection or electrode placement), orthopedics (e.g., for joint replacement and spinal screw placement), and interventional radiology (e.g., for needle guidance or catheter navigation) [66]. When combined with robotic assistance or intraoperative imaging (e.g., cone-beam CT or ultrasound), these image-guided systems improve localization accuracy, reduce operating times, and minimize damage to surrounding tissues.

The integration of image-guided technologies into the surgical workflow represents a key step toward precision surgery, enabling minimally invasive approaches, reproducible procedures, and patient-specific treatment planning.

3D Anatomical Modeling, Simulation, and Immersive Visualization Advances in medical image segmentation and volumetric reconstruction have enabled the generation of highly accurate, patient-specific three-dimensional (3D) anatomical models from CT, MRI, or ultrasound datasets [67]. These models are pivotal in preoperative planning, as they allow clinicians to explore patient anatomy in detail, simulate procedures, and customize surgical instruments or implants.

Beyond visualization, these models form the computational substrate for physics-based simulations such as finite element analysis (FEA). By assigning tissue-specific material properties and applying realistic boundary conditions, FEA allows for the simulation of stress, strain, and mechanical behavior of anatomical structures under physiological or surgical loading conditions. Such simulations are widely used in orthopedics to assess joint mechanics, fracture risk, or implant stability, and in cardiology to model myocardial deformation or valve dynamics [68]–[70].

Immersive technologies such as virtual reality (VR), augmented reality (AR), and mixed reality (MR) further enhance the utility of 3D models by enabling interactive exploration and surgical rehearsal in a risk-free environment. These platforms improve spatial understanding, support preoperative team briefings, and enhance surgical training, especially in anatomically complex or rare cases [71]. When coupled with real-time simulation engines, these systems might provide feedback on instrument-tissue interaction, tool trajectory, and anatomical deformation, thereby enriching procedural realism and training effectiveness.

Finally, the transformation of digital models into physical objects through 3D printing provides an additional layer of tangible utility. Printed models are used for surgical planning, intraoperative reference, patient communication, and the fabrication of custom prosthetics, guides, and implants. This workflow supports personalized medicine and has been shown to improve surgical accuracy and patient outcomes [72].

Digital Pathology and Radiopathomics The digitization of histopathological slides, through high-resolution whole-slide imaging (WSI), enables the application of computational techniques to analyze tissue architecture, cell morphology, and staining patterns at the microscopic level. This transformation has given rise to the field of computational pathology, in which image-derived features are extracted and quantified using machine learning and deep learning models [73], [74].

A particularly promising area of convergence is radiopathomics, which seeks to integrate quantitative imaging biomarkers from radiology (e.g., MRI, CT, PET) with features from digital pathology to form a multi-scale, multimodal characterization of disease [50]. This approach enhances the ability to correlate radiological phenotypes with histopathological ground truth, uncovering genotype-phenotype associations and improving predictive modeling for patient outcomes.

Radiopathomics is being actively investigated in oncology, where it has shown potential to bridge the gap between non-invasive imaging and invasive biopsy. In glioblastoma, for instance, studies have linked MRI-derived texture features with molecular subtypes and histologic markers of aggressiveness [75]. In prostate and breast cancers, radiopathomic models have improved the accuracy of tumor grading and risk stratification [76].

By integrating data across spatial scales, radiopathomics supports a more holistic understanding of tumor biology, enabling more accurate diagnosis, prognosis, and treatment planning. As computational models evolve, the combined use of radiological and pathological data will likely become central to personalized and precision medicine.

Telemedicine and Remote Collaboration Cloud-based platforms and web-based viewers have become essential components of modern healthcare infrastructure, enabling the remote sharing, visualization, and interpretation of medical imaging data. These technologies support real-time access to diagnostic information by radiologists, specialists, and multidisciplinary teams, irrespective of geographic location. The implementation of secure DICOM-compliant viewers, teleradiology platforms, and vendor-neutral archives (VNAs) facilitates collaborative diagnostics, second opinions, and virtual tumor boards [77], [78].

Telemedicine in imaging has proven particularly valuable in under-resourced regions and during public health emergencies, such as the COVID-19 pandemic, where physical access to healthcare facilities was limited. During this period, the accelerated

adoption of remote diagnostic workflows helped to sustain radiological services while reducing infection risk. Furthermore, the integration of artificial intelligence (AI) tools within telemedicine platforms now allows for automated triage, preliminary reporting, and worklist prioritization, enhancing diagnostic efficiency and consistency across distributed healthcare networks [79].
In this context, telemedicine extends the reach of imaging expertise, supports equitable care delivery, and facilitates interdisciplinary collaboration, making it a key enabler of modern, patient-centric imaging ecosystems.

Digital Twins The concept of a digital twin, a virtual replica of a physical entity that evolves in real time alongside its counterpart, has emerged as a transformative paradigm in healthcare [80], [81].
Medical imaging provides detailed structural, functional, and morphological information that enables the geometric and biophysical reconstruction of patient anatomy. These models serve as the spatial scaffold upon which additional physiological data, such as tissue properties, hemodynamics, or electrophysiological behavior, can be mapped [82].
Physics-based simulations such as finite element analysis (FEA), computational fluid dynamics (CFD), or electromechanical modeling can then be performed to simulate organ behavior under various conditions [83], [84]. This allows clinicians to anticipate disease progression, evaluate the response to therapeutic interventions, or virtually rehearse surgical procedures.
Medical digital twins are being developed and explored in several clinical domains. In cardiology, personalized cardiac models derived from MRI or CT data are used to simulate electrical conduction and mechanical contraction, enabling risk stratification in arrhythmias or planning of ablation therapies [82]. In orthopedics, digital twins of the musculoskeletal system support the assessment of biomechanical stresses on joints and implants [83]. In oncology, tumor models based on multiparametric imaging are used to predict growth patterns or treatment response [85]. In chronic diseases, digital twins may be implemented to foresee the outcome of a treatment or intervention and pick the more promising strategy [86]
In this context, medical imaging is not merely a diagnostic tool, but a core enabler of virtual, data-driven representations of individual health trajectories.

1.5.1 Objective and Contributions of the Thesis

The central objective of this thesis is to advance the use of digital medical imaging for quantitative diagnosis and surgical training through the development, application, and validation of computational methodologies. This work is grounded in the dual recognition that (1) modern imaging technologies produce data-rich representations of anatomy and pathology that can be mined for clinically actionable biomarkers, and (2) these same datasets can be transformed into immersive, interactive, and patient-specific models for simulation-based training and planning.

From a diagnostic standpoint, the thesis contributes novel methods for extracting and analyzing quantitative imaging biomarkers, with applications in cardiology, musculoskeletal imaging, and ophthalmology. These studies leverage standardized imaging modalities as CT and innovative approaches as infrared imaging to characterize tissue composition, structural integrity, and pathological signatures. The extracted features

are rigorously validated and contextualized to support disease classification, stratification, and prognostication. This work contributes to the field of radiomics and quantitative imaging by promoting reproducibility, clinical interpretability, and integration with emerging frameworks such as QIBA.

From a surgical perspective, this thesis investigates how image-derived anatomical models can be leveraged to enhance anatomical education, preoperative visualization, and surgical rehearsal. High-resolution 3D reconstructions generated from CT and MRI data are processed through advanced segmentation and rendering pipelines to produce accurate, patient-specific visualizations of complex anatomy. These models are integrated into immersive environments—including virtual reality (VR) and mixed reality (MR) platforms, that allow clinicians and trainees to interact with anatomical structures in intuitive and spatially meaningful ways.

The emphasis is placed on improving anatomical understanding, enhancing comprehension of morphological variability in real-life cases, and facilitating multidisciplinary communication. Such visual tools support preoperative briefings, enable procedural walkthrough, and aid in patient education by translating radiological data into tangible and explorable content. By developing an interactive clinical database where the user may query cross-sectional questions about anatomy and may read encyclopedic knowledge about what is on displayed, this work contributes to the broader adoption of image-based technologies in surgical training, digital anatomy education, and personalized medicine.

Overall, this thesis advances the digital transformation of medical imaging by:

- Developing and validating quantitative imaging pipelines for radiomic analysis in diagnostic contexts;
- Constructing anatomically accurate 3D models from clinical images for surgical planning and simulation;
- Demonstrating the use of virtual and augmented reality for medical education and training;
- Promoting reproducible, interpretable, and clinically translatable tools that bridge research innovation with real-world clinical workflows.

Together, these contributions align with the broader paradigm shift toward precision medicine and patient-specific care, illustrating how computational image analysis can enhance both diagnostic insight and procedural preparedness across multiple domains of clinical practice.

Chapter 2

Mobility Muscles Aging

Introduction

Aging is accompanied by profound changes in the musculoskeletal system that collectively impair mobility and functional independence in older adults. Among these changes, age-related loss of skeletal muscle mass and strength, a condition known as sarcopenia, is a central factor contributing to mobility decline [87]–[89]. The term sarcopenia (Greek for *poverty of flesh*) was first introduced in 1989 to describe this geriatric syndrome, and has since become a key indicator of biological aging and frailty.

Biologically, sarcopenia involves a combination of muscle fiber atrophy and loss of muscle fibers, often accompanied by increased intramuscular fat infiltration (myosteatosis) that degrades muscle quality. Clinically, it manifests as reduced muscle strength and physical performance, contributing to the frailty phenotype and increasing vulnerability to adverse outcomes. Indeed, sarcopenia is strongly associated with higher risks of falls, fractures, disability, and even all-cause mortality in the elderly. Maintaining mobility therefore emerges as a major challenge in aging populations, as sarcopenia-related weakness and balance impairment threaten the capacity for independent living [89].

Musculoskeletal Aging and Sarcopenia

Sarcopenia is now recognized as one of the most prevalent conditions affecting older adults. It begins insidiously in mid-life and accelerates with advancing age. From the fourth decade of life onward, individuals typically lose around $0.5 - 1\%$ of their muscle mass per year, such that by the eighth or ninth decade up to approximately 50% of muscle mass may be lost in severe cases [88]. This decline is accompanied by a disproportionate loss of muscle strength (sometimes termed dynapenia) which can progress even faster than muscle mass loss. Epidemiological studies indicate that roughly 10% of people over 60 years old meet criteria for sarcopenia, with prevalence rising sharply to one-third or more in those over 80. The rates vary depending on population and diagnostic criteria used; for instance, community-dwelling seniors show lower sarcopenia prevalence (on the order of $5 - 15\%$) compared to more vulnerable groups. In nursing homes, over 40% of residents may be sarcopenic, and in hospitalized elder patients roughly one in four is affected [90].

The progression of muscle degradation with age has far-reaching consequences. Qualitatively, aging muscle exhibits reduced strength, slower contractile velocity, and impaired neuromuscular coordination. Quantitatively, as muscles atrophy and are

replaced by fat and fibrous tissue, the loss of power translates into difficulties in performing daily activities. Common age-related mobility challenges such as slower gait speed, trouble climbing stairs, or rising from a chair are often direct expressions of sarcopenia's impact. In clinical terms, sarcopenia greatly increases the risk of falls and related injuries, which are a leading cause of morbidity in the elderly [90]. Musculoskeletal decline due to aging also correlates with longer hospital stays and greater likelihood of requiring assisted living or nursing care. Notably, older adults with low muscle mass and poor muscle function experience a substantially reduced quality of life and a loss of independence in daily tasks. In short, sarcopenia serves as both a hallmark and a mediator of functional decline in geriatric populations, making it a critical target for assessment and intervention in order to preserve mobility [89].

Assessing Age-Related Musculoskeletal Changes

Accurate assessment of musculoskeletal aging is essential for identifying individuals at risk and for monitoring the effectiveness of interventions. Traditional clinical assessment of sarcopenia has relied on both functional tests and measures of muscle mass. On the functional side, gait speed, grip strength, and chair-rise time provide practical indicators of muscle strength and power in older adults. Low scores on these measures signal elevated sarcopenia risk. To estimate muscle mass, traditional techniques include dual-energy X-ray absorptiometry (DXA) and bioelectrical impedance analysis (BIA). DXA scans can measure lean body mass and have been widely used to define low appendicular muscle mass in sarcopenia research and diagnosis [91], [92]. BIA offers a quick, non-invasive estimation of muscle mass by measuring the body's electrical conductivity [93]. However, both methods provide only indirect or whole-body averages of muscle tissue and can be influenced by hydration or operator technique. Moreover, they do not reveal details about muscle quality (such as fat infiltration) or the distribution of muscle loss across specific body regions.

Other imaging technologies provide more direct and localized assessments of musculoskeletal aging. Ultrasound can visualize muscle thickness and architecture in superficial muscles (e.g. quadriceps), and MRI offers high-resolution images of muscle volume and fat content without radiation. Yet, these modalities are not routinely used for large-scale screening due to practical limitations – ultrasound is operator-dependent, and MRI is expensive and time-intensive. In contrast, computed tomography (CT) has emerged as a powerful and increasingly accessible tool for evaluating muscle aging [94]. CT imaging can quantify both the quantity and quality of muscle in vivo with excellent fidelity.

One practical advantage of CT in geriatric assessment is that many older patients undergo CT scans for unrelated medical reasons (e.g. abdominal or chest scans for diagnostic workups). These existing images can be repurposed in an "opportunistic" manner to evaluate body composition without additional radiation exposure. For example, the cross-sectional area of core musculature at the L3 vertebra on an abdominal CT is highly representative of overall skeletal muscle mass, and cut-offs at L3 have been proposed for diagnosing sarcopenia. Studies have shown that such CT-based muscle measurements are reproducible and predictive of clinical outcomes, solidifying CT as a reference standard for muscle mass assessment [95], [96]. Compared to DXA or BIA, CT provides far greater detail, it can pinpoint muscle atrophy in specific muscle groups and quantify intramuscular adipose tissue that impairs muscle function. By analyzing cross-sectional slices, one can measure muscle cross-sectional area and calculate indices

like the skeletal muscle index (muscle area normalized by height) that correlate with whole-body muscle mass. Importantly, CT attenuation values (in Hounsfield units) of muscle tissue provide a measure of muscle composition – lower density indicates higher fat infiltration and poorer muscle quality, which often accompanies aging and predicts weakness [97]. These innovative imaging approaches are opening new possibilities for tracking the progression of sarcopenia and the effects of interventions (such as exercise or nutrition programs) on muscle health.

In summary, the impact of aging on human mobility is intimately linked to musculoskeletal changes, with sarcopenia standing out as a key contributor to frailty and loss of independence. A solid biological and clinical understanding of sarcopenia's progression and consequences has underscored the urgency of early detection. Traditional assessment techniques, while useful, are being augmented and surpassed by advanced imaging – particularly CT – which offers detailed insights into muscle health.

The first contribution to this thesis is a case-study paper where an interventional program is proposed to overcome aging effect and sarcopenia and CT scan imaging is used together with cross-sectional analysis and 3D reconstruction to longitudinally assess the effect of the program onto the subject.

2.1 The Impact of Persevering Home Full-Body In-Bed Gym Exercise on Body Muscles in Aging

Abstract

Background and Clinical Significance: Sarcopenia, characterized by muscle loss and fat infiltration, poses a significant health burden for aging populations. Quantitative Color 2D and 3D radiodensitometry provides a powerful tool to monitor muscle quality and quantity through CT imaging. This study assessed the impact of a ten-year-long home-bed gym exercise intervention on muscle quality in an elderly subject using CT-derived radiodensitometric analysis. The study involved two comparative analyses: Study A, which compared knee-to-ankle CT scans of the subject between 2013 and 2023; and Study B, which compared the subject's 2023 thigh CT scan with a cohort of 2500 elderly Icelandic individuals from the AGES-Reykjavik study.
Case Presentation: A 70-year-old male began a home-based Full-Body In-Bed Gym exercise program in 2013. Quantitative muscle volume and radiodensity measurements were performed using CT at baseline and after ten years.
Results: Study A shows significant improvements in muscle volume observed in the knee-to-ankle region, while a slower decline in radiodensity was noted, indicating substantial preservation of muscle quality despite the expected decay of ten-year aging. For instance, muscle volume increased by 15% in the left Soleus muscle and by 6% in the right Soleus muscle, while the average radiodensity decreased by 12–17 HU. The subject's thigh muscle quality at 80-years-old is above the AGES- Reykjavik's cohort average, with reduced fat infiltration.
Conclusions: Long-term home Full-Body In-Bed Gym, a low-impact exercise, can mitigate aging sarcopenia, as evidenced by improved tissue radiodensity and muscle mass substantial preservation. This suggests potential applications in personalized healthcare strategies to enhance muscle preservation among aging populations.

2.1.1 Introduction

Sarcopenia, the age-related decline in muscle strength and mass, significantly impacts the elderly population's quality of life, increasing risks of falls, frailty, and mortality [98].

Studies demonstrate that maintaining moderate to high levels of physical activity throughout life is the most effective countermeasure against age-related decline in muscle health and function [98]. However, a significant portion of the global population remains largely sedentary, a trend that only intensifies with age. This widespread lack of physical activity accelerates the natural decline associated with aging, contributing to conditions like sarcopenia, reduced mobility, and overall poorer quality of life in older adults [99].

As a result of the growing interest in diagnosing and monitoring sarcopenia, quantitative radiodensitometry using computed tomography (CT), which measures tissue density based on its attenuation of X-rays during a CT scan, has become a valuable and reliable tool. This technique allows for a detailed assessment of muscle quality, including muscle density and the degree of fat infiltration, providing critical insights into both muscle mass and structural integrity [100].

This study addresses a significant research gap by providing long-term evidence about the effectiveness of accessible home-based exercise programs, specifically the Full-Body In-Bed Gym, in mitigating sarcopenia in elderly populations. The Full-Body In-Bed Gym is a home-based exercise protocol designed to address muscle weakness and atrophy, particularly in aging or impaired populations [101]–[103]. Inspired by established cardiovascular and respiratory rehabilitation protocols for surgical patients, this regimen adapts those principles into a short (10–20 min) sequence of 10–15 simple, tool-free exercises that can be performed entirely in bed. The exercises include movements such as hand gripping, ankle flexion, arm and leg cycling, spinal stretching, and progressive weight-bearing activities, all aimed at enhancing muscle strength, mobility, and overall physical fitness. Starting with as few as 3–5 repetitions, participants gradually increase to 15–20 repetitions as they build endurance. Over time, the speed and intensity of exercises are adjusted to maximize their benefits.

The program has been shown to be effective in improving quality of life and reducing pain in elderly individuals, with participants reporting significant enhancements after two months of consistent practice. Furthermore, this program not only offers a practical method for preserving muscle mass and function in the elderly, but it also provides a significant exercise opportunity for economically disadvantaged populations, who may not be able to afford expensive equipment or gym memberships [101]–[103].

Despite the growing recognition of exercise as a key intervention to combat muscle loss, there is limited data on the sustained impact of such programs. Here, we explore the application of quantitative radiodensitometry paired with 2D and 3D imaging to acquire information about the average X-ray absorption properties of soft tissue and their distributions as Hounsfield Units (HU). Indeed, while quantitative radiodensitometry, including 2D and 3D imaging, has shown promise in assessing muscle health, its application in aging populations has not been well explored.

This case report aimed to fill these gaps by utilizing a 10-year longitudinal study with CT imaging to monitor muscle health outcomes, offering a cost-effective and accessible solution for preserving muscle mass and improving quality of life in older adults.

The aim of this case report was twofold: (1) to support the fact that the Full-Body In-Bed Gym program can combat sarcopenia; and (2) to provide further evidence supporting the effectiveness of 2D and 3D quantitative radiodensitometry as a monitoring tool for muscle health in aging populations.

2.1.2 Case Presentation

2.1.2.1 Study Design

This study focused on a 70-year-old male subject who undertook a home-based exercise regimen for over 10 years. The main objectives were to assess changes in muscle volume and quality over time using radiodensitometry. The study was divided into two parts: (1) Study A compared CT scans of the knee-to-ankle region from 2013 and then 2023; while (2) Study B compared data from a cross-section of a 2023 thigh CT scan with the data from a cohort of 2700 age-matched individuals from the AGES-Reykjavik study.

2.1.2.2 Intervention

The home-based Full-Body In-Bed Gym program employed here consisted of 10 exercises performed six times per week. The Full-Body In-Bed Gym program allows individuals to engage in various exercises from the comfort of their beds, making it particularly appealing for those with mobility limitations or those who prefer to exercise without getting out of bed. This program typically involves a series of low-impact exercises that can be performed while lying down, sitting, or even standing next to the bed. Exercises may include strength training and stretching activities. The subject performed 10 repetitions of each exercise starting in 2013, which he gradually increased in intensity and volume over time. Each session lasted between 5 and 15 min.

Figure 2.1 shows one of the ten home Full-Body In-Bed Gym protocol exercises. The figure was reprinted with permission from the reference Maccarone et al. 2023 [101].

2.1.2.3 Imaging Protocol

Study A: Knee-to-Ankle Comparison (2013 vs. 2023) CT scans were conducted using a Philips iCT 256 scanner. Baseline scans from 2013 were compared to scans from 2023, focusing on the region from the knee to the ankle. Both scans were acquired at 120 kVp, with a voxel size of 0.665 mm and slice thickness of 0.335 mm. Radiodensity and muscle volume were measured using custom segmentation software, analyzing three major muscle groups: *Tibialis anterior*, *Soleus*, and *Gastrocnemius* muscles.

Study B: Thigh Comparison: Longitudinal Case Study (2013–2023) vs. AGES-Reykjavik Population [104], [105] Images were captured from the mid-thigh region using a voltage of 120 kVp. This study compared the 2023 CT scan of the subject's thigh to those of a reference population of 2500 age-matched individuals from the AGES-Reykjavik cohort. Radiodensity was measured for fat (-200 to -10 HU), connective (-10 to 40 HU), and muscle (40 to 200 HU) tissues. The case study values were plotted against the AGES-Reykjavik cohort group to assess relative muscle quality and fat infiltration.

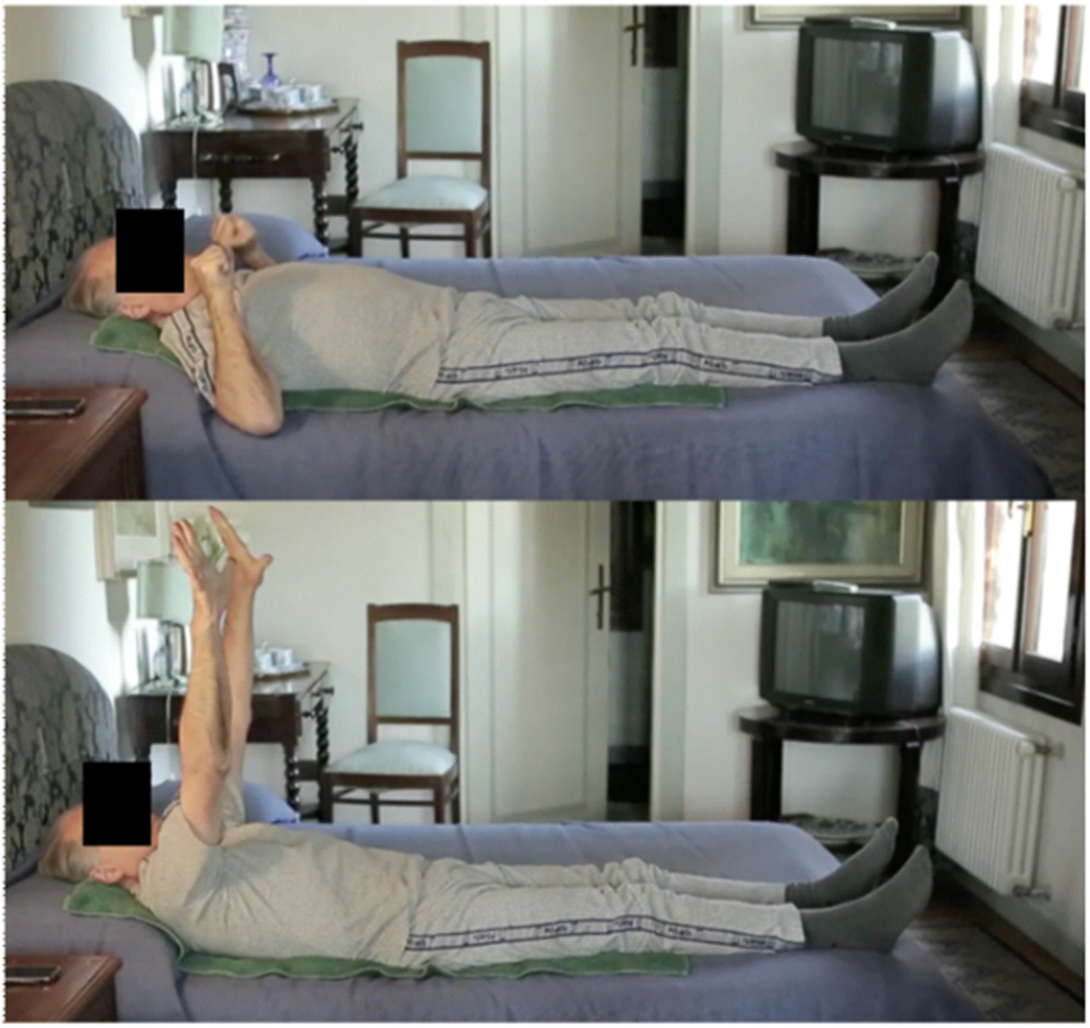

Figure 2.1: An example of the ten exercises which constitute the home-based Full-Body In-Bed Gym protocol.

2.1.2.4 Medical History of the Octogenarian

The case study subject was a male, born in Abano Terme, Padua, Italy, on 23 February 1943. His medical history was collected at the beginning of the study, with the main pathological events including:

In 1969, the subject experienced a vehicular accident that resulted in fractures to both legs and ankles. A significant complication from the incident was the rupture of his spleen, which necessitated surgical removal to address the internal bleeding. He survived as a result of the intravenous infusion of fluids and blood from donors. Unfortunately, during his subsequent convalescence, he developed transfusion-induced hepatitis, which delayed the recovery of the skeletal lesions.

Over the next 40 years, he experienced only two episodes of viral flu and has not developed any COVID-19 infections to date. He has received five doses of anti-COVID vaccines.

Despite having no family history of hypertension and only passive smoking exposure, he was diagnosed with asymptomatic arterial hypertension at the age of 40. He delayed treatment, which ultimately resulted in severe coronary artery disease.

From his medical history recently collected at the Hospital of Rovigo, Italy, we report the following:

An 80-year-old man with a history of hypertension and mixed dyslipidemia, treated pharmacologically since age 45, began experiencing symptomatic effort angina at age 68. Coronary angiography revealed significant disease in the right coronary artery (RCA), left circumflex artery (LCx), and first diagonal branch (D1), leading to percutaneous coronary intervention (PCI) and a drug-eluting stent (DES) placement. Three years later, he developed a symptomatic popliteal artery aneurysm requiring surgical exclusion. At a 10-year follow-up, a transthoracic echocardiogram indicated chronic ischemic/hypertensive cardiomyopathy with preserved left ventricular function. Holter monitoring showed initial conduction system impairment, including first- and second-degree atrioventricular blocks and frequent ectopic beats. Follow-up coronary angiography demonstrated good patency of the previously implanted DES. His optimized outpatient cardiology regimen included aspirin 100 mg, Irbesartan 300 mg once a day, calcium antagonist 10 mg once a day, and rosuvastatin 10 mg.

Despite this strong evidence of a slowly progressive cardiomyopathy, the subject still performs all regular activities of daily living, engages in light voluntary exercise (home-based Full-Body In-Bed Gym), and undertakes heavy gardening work.

2.1.2.5 Quantitative Image Analysis

In Study A we compared volumetric CT data taken from knee-to-ankle joints (Figure 2.2).

CT images were analyzed using Mimics 26.0 segmentation software (Materialize, Belgium).

To assess the effect of the intervention, a 3D model of the calves was reconstructed from the two datasets. An initial thresholding between 0 and 150 HU was performed. To regularize the borders and eliminate floating pixels, a closing gap operation with a gap size of 4 pixels followed by an erosion of 2 pixels was performed. These operations resulted in a 3D model of the muscles in the calves, including the intramuscular fat and other tissues inside muscle bundles. The four principal muscles were separated with a manual splitting tool following their borders over the darker background, and the volume of each bundle was extracted. At this point, the histogram of each muscle was drawn, and the HU spanned from -200 to 200. The contribution of different tissue types was extracted: fat (-200 to -10 HU), connective tissue (-10 to 40 HU), and muscle (40 to 200 HU) [106]. The average HU was calculated and stored for further comparison.

In Study B, we analyzed a mid-thigh CT image cross-section of the Octogenarian (Figure 2.3). We calculated the average radiodensity of connective, muscle, and fat tissues, extracted with the same threshold introduced before (Figure 2.4), and compared it with age-matched controls from the AGES-Reykjavik cohort database. The amount of fat computed in this manner evaluated both intramuscular and subcutaneous fat. In the AGES cohort, we analyzed the same parameters from 2700 individuals aged 65 to 95 [104], [105].

2.1.2.6 Results

Study A: Knee-to-Ankle Muscle Volume and Density Changes (2013 vs. 2023) Data analysis revealed that muscle volume increased across all studied groups of muscles within the distal part of the leg, particularly in the *Soleus* and *Tibialis anterior* muscles. The left *Soleus* muscle showed a 15% increase, while the right *Soleus* muscle increased by 6% (Table 2.1). Despite the increases in muscle volume, the

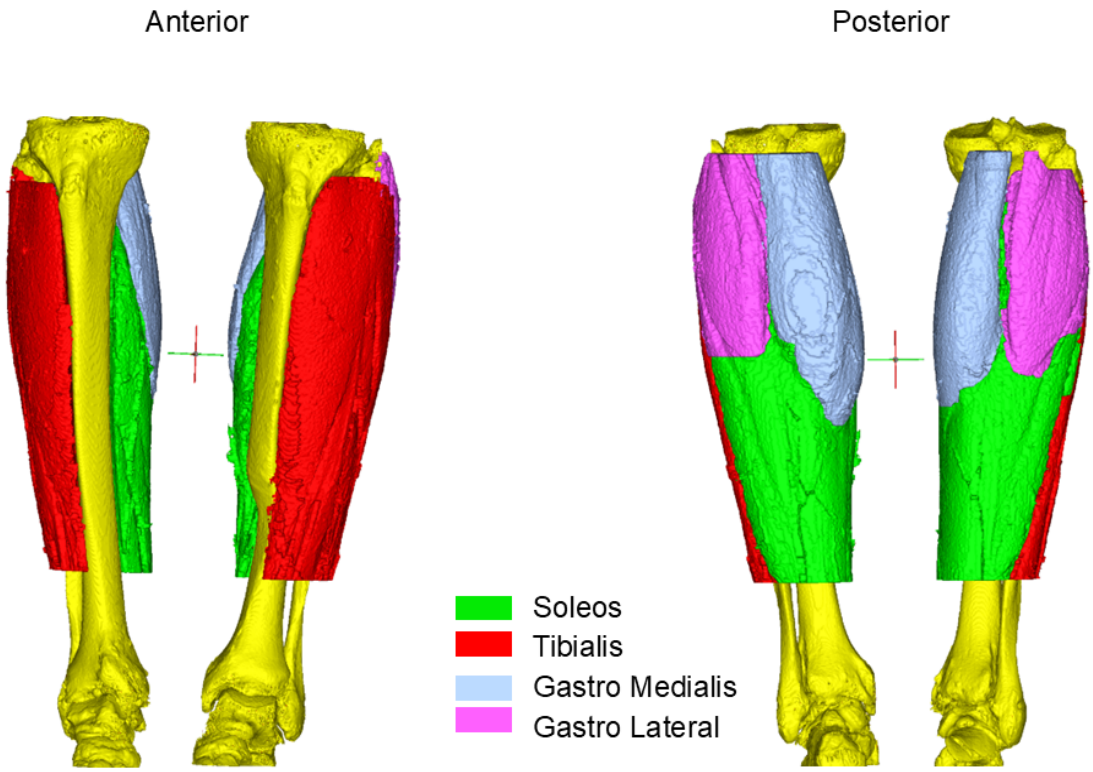

Figure 2.2: Muscle segmentation of the Octogenarian: Different region of interest from the first time point in 2013 when he was 70-years-old.

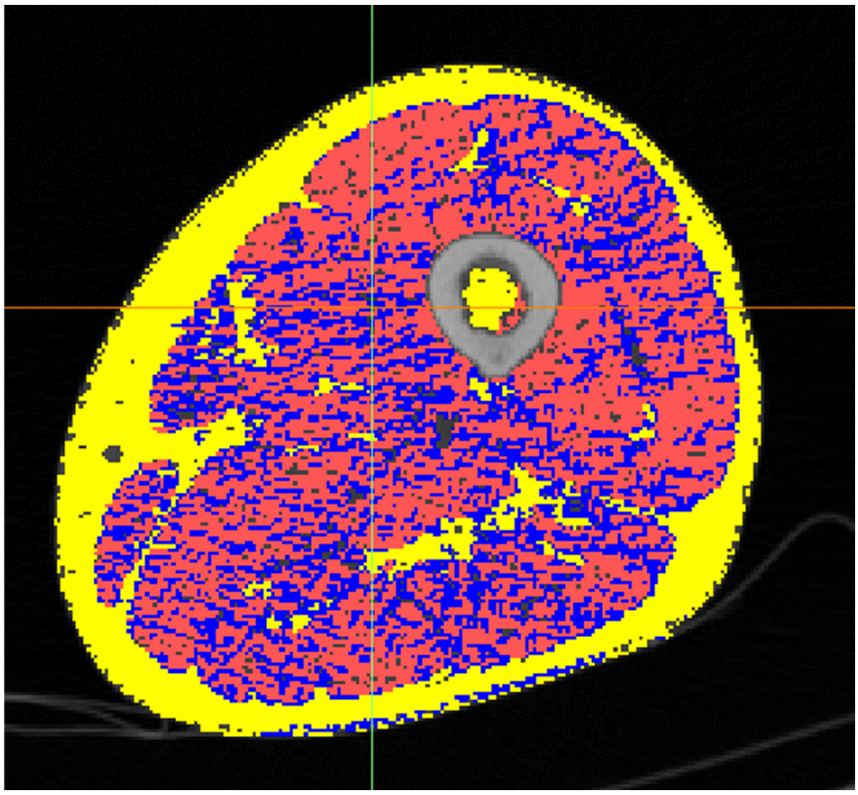

Figure 2.3: Cross-section of the mid-thigh of the Octogenarian. Fat in yellow, connective in blue and muscle in red.

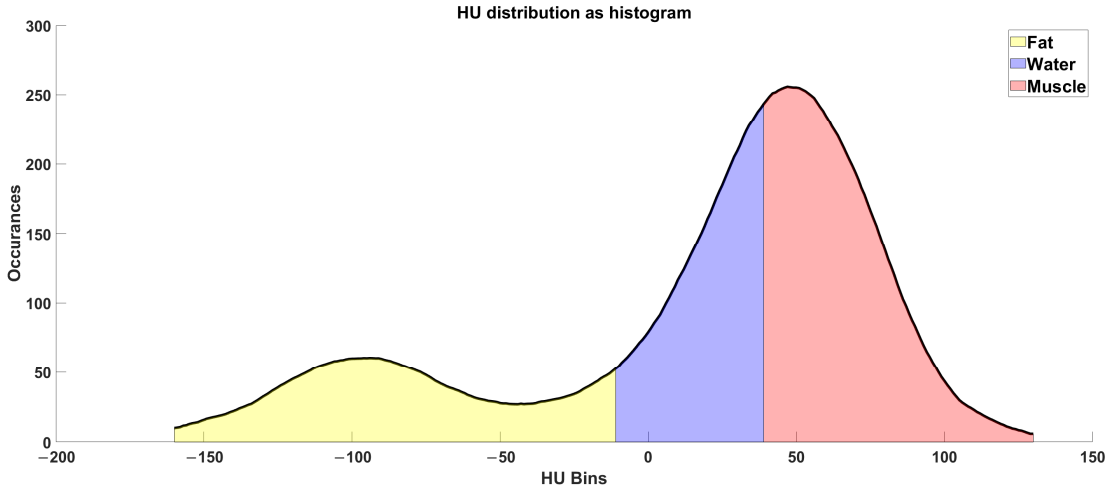

Figure 2.4: Radio densiometric profile of the cross-section of the mid-thigh of the Octogenarian in 2023, where the areas of fat, connective, and muscle tissues are colored, respectively, in yellow, blue and red.

muscle radiodensity decreased (Table 2.2); however, this decline occurred at a slower pace than reported in the literature about the average muscle radiodensity decay that accompanies 10 years of aging (see discussion). Indeed, the radiodensity data revealed a moderate decline in muscle density and increased fat infiltration. Nonetheless, the fat infiltration of the subject remained lower than that reported in the literature [107]–[117].

Table 2.1: Muscle bundle volumes and their percent change in response to the intervention.

Row	**Muscle Group**	**Vol at 70 ys (cm^3)**	**Vol at 80 ys (cm^3)**	**% Change**
1	*Soleus* (Left)	463	618	+33%
2	*Soleus* (Right)	555	542	−3%
3	*Tibialis* (Left)	332	361	+9%
4	*Tibialis* (Right)	351	344	−2%
5	*Gastrocnemius* Medial (Left)	194	194	/
6	*Gastrocnemius* Medial (Right)	143	154	+8%
7	*Gastrocnemius* Lateral (Left)	165	151	−8%
8	*Gastrocnemius* Lateral (Right)	119	195	+64%

The analysis also revealed that total muscle volume increased in both legs over the ten years of intervention (15% left leg and 6% right leg). However, not all muscles underwent the same changes: left leg distal muscles (*Soleus* and *Tibialis* muscles) experienced an increase in volume, whereas on the right leg their volume slightly decreased (Table 2.1, rows 1 to 4). On the other hand, an opposite scenario was revealed for the *Gastrocnemius* muscles. The left volume decreased less than 10% in volume while the right *Gastrocnemius* muscle gained almost 65% in volume laterally (Table 2.1, rows 5 to 8). A graphical representation of these results is pictured in Figure 2.5.

On the other hand, average muscle radiodensity increased from 12 to 17 HU, whereas the average fat and connective tissues radiodensity increased from 5 to 17 HU.

Table 2.2: Tissue radiodensity by muscular bundle before (rows 1–4) and after (rows 5–8) the intervention. Values in Hounsfield Units (HU).

Row	Left Leg (70 yrs)	Muscle	Fat	Connective	Right Leg (70 yrs)	Muscle	Fat	Connective
1	*Tibialis*	68	−35	23	*Tibialis*	71	−33	22
2	*Soleus*	71	−38	21	*Soleus*	69	−37	21
3	*Gastrocnemius medial*	73	−38	21	*Gastrocnemius medial*	70	−37	23
4	*Gastrocnemius lateral*	69	−38	21	*Gastrocnemius lateral*	68	−32	21
Row	**Left Leg (80 yrs)**	**Muscle**	**Fat**	**Connective**	**Right Leg (80 yrs)**	**Muscle**	**Fat**	**Connective**
5	*Tibialis*	56	−24	27	*Tibialis*	57	−21	29
6	*Soleus*	58	−28	23	*Soleus*	57	−26	26
7	*Gastrocnemius medial*	56	−27	25	*Gastrocnemius medial*	55	−28	26
8	*Gastrocnemius lateral*	55	−25	25	*Gastrocnemius lateral*	54	−25	25

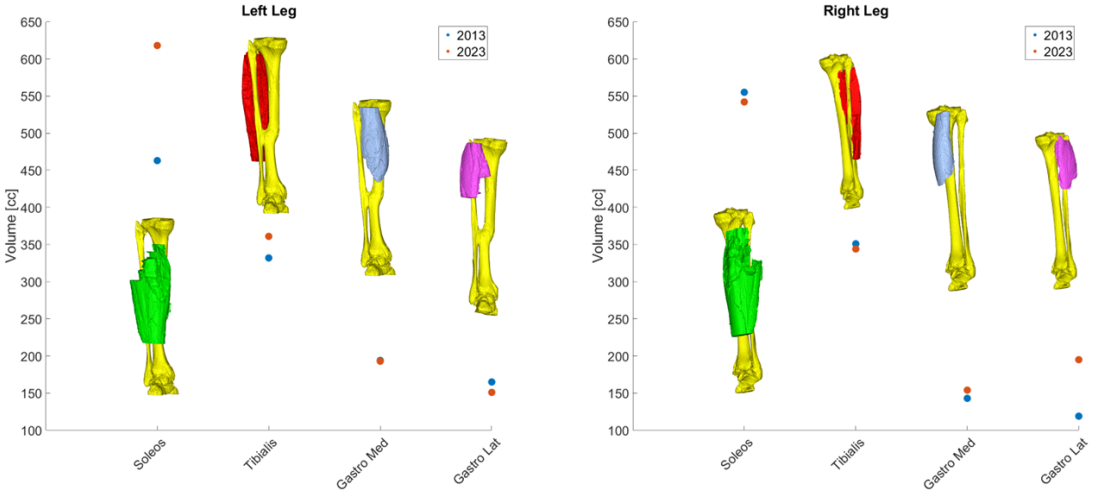

Figure 2.5: Volumetric changes in muscular bundle by leg.

Study B: Thigh Muscle Quality Compared to AGES-Reykjavik Population

The radiodensitometric profile extracted from the cross-section of the midthigh is reported in Figure 2.6. The different tissues are highlighted with different colors. The extracted averages are 61.25 HU for muscle (red), 23.20 HU for connective tissue (blue), and −81.70 HU for fat (yellow).

Compared to the AGES-Reykjavik population, the Octogenarian's 2023 thigh CT scan revealed a higher-than-average muscle density and reduced fat infiltration. Indeed, when the subject's average values are plotted with that of the AGES population, the data place the subject above average in muscular density and at a lower subcutaneous fat density (Figure 2.6).

2.1.3 Discussion

This study demonstrated the effectiveness of a long-term, home-based exercise protocol in mitigating sarcopenia, as evidenced by the preservation of muscle volume and the reduced fat infiltration in the muscle of our exercising elderly subject. Quantitative radiodensitometry using CT imaging has proven to be a valuable tool for assessing long-term muscle quality and quantity.

The home-based Full-Body In-Bed Gym program demonstrated significant benefits in preserving muscle mass and quality. The subject was in his seventies ("Septuagenarian") when the intervention began and is now in his eighties ("Octogenarian"). The

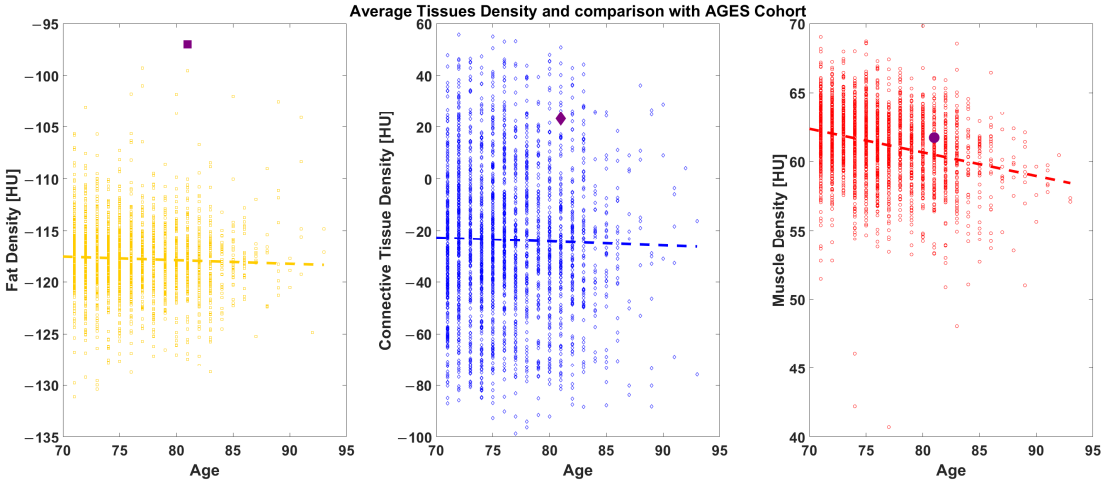

Figure 2.6: AGES comparison: The Octogenarian (reported as a black symbol) is shown against a cohort of 2700 age-matched individuals ranging from 70 to 95-years-old.

unbalanced volume changes (i.e., differences in left and right legs), reported in Figure 2.4, may be a consequence of the right-side dominancy of the subject's posture.

Additionally, the Full-Body In-Bed Gym program contributed to improved quality of life, reduced pain, and a decreased risk of sarcopenia in the elderly sedentary individual [101]. This suggests that similar exercise programs could be effective for a broader aging population. An added benefit of the home-based Full-Body In-Bed Gym is that this safe approach is highly cost-effective.

Compared to data in the literature, the subject maintained higher than average radiodensity values and better muscle quality, highlighting the potential of persevering low-medium intensity exercise to slow muscle decay associated with aging. Our findings are consistent with previous research, showing the efficacy of exercise interventions in combatting sarcopenia, whether due to aging and neuromuscular disorders [107]–[117], or tumors [118]–[120]. Specifically, quantitative radiodensitometry has proven to be a reliable method for assessing both muscle mass and quality, allowing for precise monitoring of age-related and exercise-related changes.

Muscle type also plays an important role in age-related muscle degeneration. Age-related atrophy has proven to affect various muscles fibers differently. For example, type II fibers, which are more prevalent in the locomotor muscles of the lower body (e.g., *Gastrocnemius* muscle), experience greater rates of atrophic change while only moderate changes occur among type I fibers, characteristic of the muscles involved in a postural role (e.g., *Soleus* muscle) [121]–[124]. On the other hand, hypoplasia has also been found to contribute partially to muscle mass reduction [121]. Some reports suggest that hypoplasia and atrophy contribute equally to muscle loss [124]. Indeed, studies have highlighted the critical importance of both processes, although there remains some controversy over which one plays the more significant role [125]–[136].

Similar results were found in a previous study: Ikezoe et al. (2011) found that muscle thickness, measured by ultrasound, decreases with aging based on the type of muscle, and that life-space assessment (LSA) correlates only with the *Soleus* muscle [137]. Reimers et al. (2012) demonstrated the impact of aging and athletic activity on a large, mixed cohort. They found that in athletes, calf thickness remained stable

with age, although fat content increased. However, in non-athletic males, the thickness of the *Gastrocnemius* and *Soleus* muscles decreased significantly—by 16% between the ages of 20 and 70—while the *Tibialis* muscle showed only a 7% reduction [138]. On the other hand, Trappe et al. (1996) reported that elite distance runners and lesser trained/untrained subjects have the same calf cross-sectional area [139]. In addition, Klitgaard et al. (1990) found that elderly swimmers and runners had similar calf cross-sectional areas compared to an age-matched less active control group [140].

Exercise plays a crucial role in the prevention and management of sarcopenia. Numerous studies in the literature demonstrate that regular exercise programs, particularly resistance and strength training, can significantly reduce the risk of sarcopenia by improving muscle mass, strength, and mobility [141]. However, in low-income countries, where access to fitness facilities and equipment is limited, the challenge lies in implementing sustainable and accessible interventions [142]–[147]. Low-cost solutions, such as bodyweight exercises or home-based programs, have proven effective in promoting muscle health even in resource-limited settings [104], [148]–[150]. Simple, safe, and adaptable protocols, such as the Full-Body In-Bed Gym, could serve as valuable strategies to combat sarcopenia and enhance quality of life, particularly in economically vulnerable populations.

Future research should expand on these results by studying more extensive cohorts and incorporating diverse exercise regimens to validate the benefits of such interventions further [99]. Additionally, the role of quantitative imaging in tracking muscle health warrants further exploration to enhance diagnostic and therapeutic strategies for sarcopenia.

2.1.4 Conclusions

CT-based quantitative radiodensitometry is a valuable method for tracking muscle health over time, particularly in aging populations. The Full-Body In-Bed Gym program, designed for home use, showed promising results in maintaining muscle mass and quality, which could contribute to improved quality of life and reduced sarcopenia risk among sedentary older adults. These findings highlight the potential for similar low-cost exercise programs to serve as practical and scalable interventions, benefiting both individual health outcomes and societal healthcare systems. Furthermore, quantitative radiodensitometry paired with 2D and 3D imaging is an excellent way to assess muscle quality and would be useful for diagnoses of muscle pathologies and follow-ups of muscle treatment regimes.

Chapter 3

Quantitative Diagnosis of Acute Myocardial Infarction and Hypertrophic Cardiomyopathy Using Coronary CT Angiography, Radiomics, and Machine Learning

Cardiovascular diseases remain among the leading causes of death and disability worldwide. In particular, coronary artery disease leading to acute myocardial infarction (AMI) is a major contributor to global mortality [151]. Rapid and accurate diagnosis of AMI is critical, as timely reperfusion therapy markedly improves outcomes and reduces complications [152]. Hypertrophic cardiomyopathy (HCM), an inherited cardiac muscle disorder with an estimated prevalence of 1 in 500, is likewise a condition where precise diagnosis and risk stratification are of great clinical importance [153]. HCM is a leading cause of sudden cardiac death in young individuals and athletes, and tragically, sudden death can be the first manifestation in asymptomatic cases [153]. These realities underscore the need for improved diagnostic approaches for both acute infarction and cardiomyopathic disease, enabling earlier intervention and tailored management. Contemporary cardiac imaging modalities have advanced the evaluation of AMI and HCM, yet each has notable limitations. Echocardiography and invasive angiography provide insight into cardiac function and coronary anatomy, but they offer limited direct information on myocardial tissue characterization. Cardiac magnetic resonance (CMR) with late gadolinium enhancement (LGE) has emerged as the noninvasive gold standard for detecting myocardial scars and fibrosis [154]. LGE-CMR can reveal characteristic patterns of ischemic scar in infarction and fibrosis in HCM, and the extent of LGE correlates with adverse remodeling and arrhythmic risk [155].

However, despite its critical clinical value, CMR is not universally accessible or practical for all patients. Many hospitals lack immediate CMR availability, and in acute settings (such as an evolving MI) the lengthy scanning times and need for specialized expertise limit its use. Furthermore, certain patient populations cannot undergo MRI due to contraindications: for example, individuals with incompatible implanted devices, severe claustrophobia, or an inability to tolerate long scans. Even when MRI is possible, image quality can be degraded by artifacts from implanted defibrillatorsn or pacemakers. These limitations often force reliance on less optimal surrogates or delay definitive diagnosis. In the case of HCM, diagnosis is frequently made by echocardio-

graphy, but assessing myocardial fibrosis (a key prognostic marker) typically requires CMR, which not all patients can obtain [156], [157].
There is thus a compelling impetus to develop alternative or complementary imaging strategies that can quantitatively characterize myocardial injury and cardiomyopathic changes with wider accessibility. Coronary computed tomography angiography (CCTA) has rapidly become a cornerstone in noninvasive cardiac imaging, owing to its wide availability and high diagnostic performance for coronary artery disease. Modern CCTA is a first-line test for chest pain evaluation, boasting excellent accuracy in detecting coronary stenoses [158]. Beyond coronary lumen assessment, CCTA also acquires volumetric images of the myocardium, which hold untapped diagnostic information. Unlike MRI, CT scanners are ubiquitous in emergency and hospital settings and can rapidly scan patients, making them attractive for acute care. Traditionally, CT has been regarded as less sensitive than CMR for myocardial tissue characterization. However, recent developments suggest that with specialized techniques, CT can delineate myocardial scar and fibrosis [159]. In particular, delayed iodine-enhanced cardiac CT imaging (analogous to LGE in MRI) can highlight regions of myocardial infarction or fibrosis by performing a scan several minutes after contrast injection [159]. Studies have demonstrated that late iodine enhancement CT (LIE-CT) can successfully identify acute infarcts and even fibrotic lesions from non-ischemic cardiomyopathies, showing patterns that correspond to those seen on LGE-CMR. For example, dual-energy CCTA protocols can differentiate scarred myocardium based on iodine contrast kinetics, and have yielded promising results in detecting MI-related scar tissue [160]. LIE-CT has also proven useful in visualizing fibrosis in conditions like HCM, myocarditis, and sarcoidosis [161], [162]. While CT-based delayed enhancement has limitations (such as difficulty detecting diffuse interstitial fibrosis and concerns about radiation exposure), ongoing improvements in CT technology and protocols continue to enhance its viability [159], [163]. Taken together, these advances suggest that CCTA, beyond its role in coronary assessment, could evolve into a more comprehensive cardiac imaging tool capable of "virtual" tissue characterization when MRI is unavailable.

In order to fully capitalize on CCTA data for diagnosing myocardial infarction and HCM, advanced image analysis methods are required. Radiomics has emerged as a powerful approach to extract quantitative features from medical images, effectively transforming imaging data into high-dimensional mineable information. Rather than relying solely on visual interpretation, radiomic analysis computes a multitude of descriptors that characterize the intensity distribution and textural patterns within the myocardium [44], [164]. This approach can uncover subtle differences between healthy and diseased tissue that may elude the human eye, thereby decreasing observer biases and improving diagnostic accuracy. Radiomics features are typically categorized by their level of complexity or "order." First-order features are basic statistical measures of the voxel intensities (Hounsfield unit values in CT) without regard to spatial arrangement. These include radiodensitometric metrics such as mean attenuation, standard deviation, skewness, kurtosis, and entropy of the intensity histogram [165], [166]. Such first-order features can reflect global tissue characteristics (for instance, the average CT attenuation of myocardium or the heterogeneity of density). Building on this, second-order features (texture features) quantify spatial relationships between voxels [167]. Common second-order radiomic features derive from matrices like the Gray-Level Co-occurrence Matrix (GLCM) or Gray-Level Run-Length Matrix, capturing patterns of texture coarseness, contrast, and repetition within the myocardial tissue [168], [169]. These texture features can detect localized heterogeneity, for example, the

patchy scarring or fibrosis that might be present in an infarct zone or in HCM-affected myocardium. Further extending the analysis, higher-order features are computed after applying mathematical filters or transforms to the images. One prominent example is the use of wavelet transforms, which decompose the image into multiple frequency bands. Wavelet-based features can highlight repetitive patterns or edges at different scales, potentially detecting microstructural abnormalities in the heart muscle [170]. By progressing from first-order to texture to frequency-domain features, radiomics provides a comprehensive quantification of tissue properties. Notably, this quantitative "virtual biopsy" approach has already shown promise in cardiological applications [171]. For instance, radiomic analysis of CCTA in HCM patients has been able to identify regions of myocardial fibrosis that correspond to LGE on MRI [172]. Such findings suggest that radiomics could enable CT scans to serve as a proxy for MRI in detecting fibrosis or infarction, greatly broadening the utility of CT in cardiac diagnosis. Indeed, several studies indicate that integrating radiomics into CCTA interpretation improves diagnostic power and helps overcome the subjectivity and inter-reader variability of conventional imaging assessments[173]–[175]. Realizing the full potential of radiomics for diagnosing AMI and HCM also necessitates robust analytical models. The large number of features extracted in radiomic analysis demands machine learning (ML) techniques to discern which combinations of parameters are most indicative of disease.

In this chapter, we leverage supervised ML classifiers to distinguish pathological myocardial signatures from normal variants based on radiomic feature patterns. Prior radiomics research in both oncology and cardiology has employed various classifiers, from logistic regression and support vector machines to ensemble tree methods, to build predictive models [176]. Here, we focus on two complementary ML approaches to improve diagnostic performance: an ensemble of quadratic discriminant analysis classifiers, and a gradient-boosted decision tree method (LightGBM). Quadratic discriminant analysis (QDA) is a probabilistic classifier that, unlike its linear counterpart, can model non-linear decision boundaries by allowing distinct covariance structures for each class. By using an ensemble of QDA models (for example, through bagging or subspace methods), we aim to capture subtle multidimensional differences in radiomic feature distributions between hypertrophied, and normal myocardium. Meanwhile, Light Gradient Boosting Machine (LightGBM) is a state-of-the-art ensemble learning algorithm based on gradient-boosted tree models. LightGBM is well-suited to high-dimensional data and can automatically handle feature interactions and non-linear relationships. It has demonstrated superior accuracy in various radiomics-based diagnostic tasks, making it a natural choice for my application [177], [178]. By training these classifiers on labeled datasets (e.g. patients with confirmed HCM, or controls), the model learns to recognize complex radiomic signatures associated with each condition. We further employ rigorous validation to ensure the models generalize and to avoid overfitting given the relatively small sample sizes typical in medical imaging studies. In summary, this chapter introduces a novel framework for the quantitative diagnosis of acute myocardial infarction and hypertrophic cardiomyopathy using CCTA-derived data, radiomic feature extraction, and machine learning. We outline how the integration of radiomics and AI-driven analysis can enhance traditional CT imaging, enabling it to detect myocardial infarcts and cardiomyopathic changes with greater accuracy. The ultimate goal is to broaden the clinical utility of CT as a readily accessible imaging modality for cardiac tissue characterization, supplementing or in some cases substituting for MRI-based assessments. By improving diagnostic accuracy for AMI and HCM, this work can contribute to faster diagnosis in acute care, better risk

stratification in chronic disease, and overall more informed clinical decision-making. The following sections detail the development of radiomics signatures from CCTA, the implementation of the QDA ensemble and LightGBM classifiers, and an evaluation of their performance in identifying myocardial infarction and HCM. Through this approach, we aim to demonstrate that quantitative analysis of CT images can uncover "hidden" biomarkers of cardiac pathology, ultimately moving cardiac CT beyond anatomy into the realm of tissue characterization and precision diagnosis. Each component – from the clinical motivation to the computational methods – builds toward a more comprehensive diagnostic tool that leverages widely available CT technology to improve care for patients with these serious cardiac conditions.

3.1 Virtual Histology of the Heart Through CT Imaging: Preliminary Results of a Novel Noninvasive Approach for Cardiac Tissue Characterization

Abstract

The world's population is aging and cardiovascular diseases can become the first cause of frailty in the next future. This study proposes a novel workflow to measure cardiac tissue quality and composition from a CT scan directly through the Hounsfield Units distribution of 3D samples. The cohort includes 15 healthy subjects to study normal heart densitometric composition and 7 hypertrophic patients to measure how the pathology affects myocardial tissue. A significative fat content of 3% of the volume is found in the hypertrophic free wall while the connective tissue in the septum changed from just above 1% to around 5%. Therefore, the proposed noninvasive approach might become a clinical marker to improve diagnosis derived from CT imaging.

3.1.1 Introduction

Strategies to tackle cardiovascular diseases (CVD) become crucial as the population ages. Nowadays, people present multiple comorbidities, and CVDs could lead to a condition of frailty with a compromised quality of life [179]. On the other hand, the number of children and adolescents with hypertension is not decreasing making them prone to develop CVDs, and particularly hypertrophic cardiomyopathy (HCM) [180]. In a scenario of evolution and with disease stratifications, having more markers to track pathology development is necessary.

Imaging techniques (echocardiography, cardiac magnetic resonance imaging and cardiac computed tomography) can investigate both morphological and functional aspects such as wall size and motion, presence of scars, narrowing of coronaries, presence of calcifications and others. Direct information about tissue content and quality are still lacking. In particular, computed tomography is already used to extract measurements about soft tissue from the Hounsfield unit (HU) distributions.

Edmunds et al. compared the HU distributions from a cross-section of the midthigh to investigate tissue composition among young individuals, elders and subjects with sarcopenia [166]. The trimodal profile was then used on a large dataset to compute the

quantity of fat, connective and muscular tissue and relate them with self-reported and instrumentally measured biometric features [97], [181]. In a longitudinal study using the same parameters from the midthigh authors were able to predict CVD, chronic heart failure and coronary heart disease [182].

The objective of the study is to understand if a novel approach of virtual histology based on HU distribution applied to cardiac tissue of the left ventricle can describe cardiac muscle status and detect the presence of pathologies modifying myocardial tissue.

3.1.2 Materials & Methods

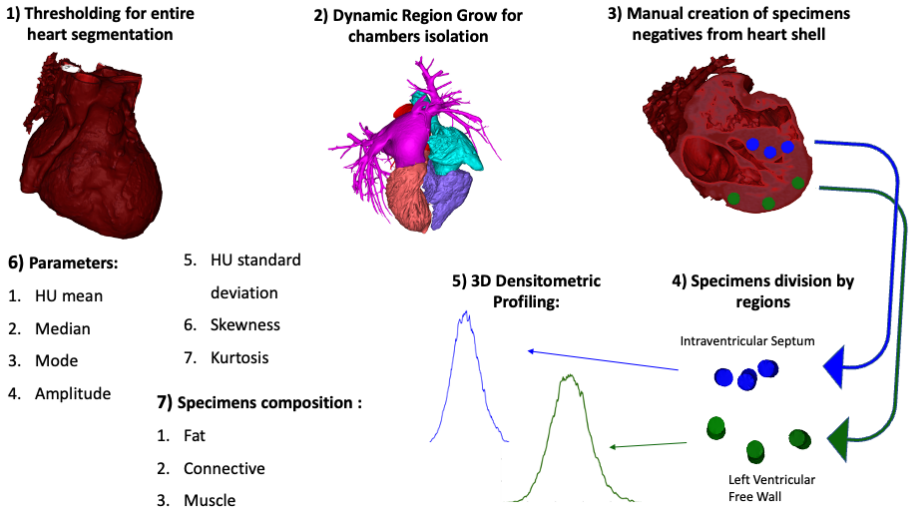

Figure 3.1: Novel workflow for densitometric parameters extraction and tissue composition analysis.

3.1.2.1 Population

The cardiac volume database comprised 22 subjects: 15 healthy and 7 with obstructive HCM. 15 static CT data were acquired with a Revolution Evo GE Healthcare machine with a $100kV$ radiogenic tube. 7 static CT data were acquired with a Canon Medical System Aquilion ONE machine with a $120kV$ radiogenic tube. Pixel size (PS) was in $0.4 - 0.5mm$ range and slice thickness (ST) between 0.25 and $0.6mm$ with a field of view (FOV) of $200 - 250mm$.

3.1.2.2 Cardiac CTs segmentation and parameters extraction

We propose a novel workflow (Figure 3.15) to extract 3D samples from the external wall of the left ventricle (LVFW) and the interventricular septum (IVS) and to analyze tissue composition based on the HU distributions.
Image analysis was performed in Mimics 23.0 software (Materialise, Leuven, Belgium). A mask for the entire myocardium in $[-200; 1600]$ HU range was created (Fig 3.15, panel 1).

Simultaneously, a mask for each heart chamber was obtained based on different pixel intensities and dynamic region-grown algorithms. (Fig 3.15, panel 2) A boolean subtraction of heart chamber masks from the first one was performed to isolate the myocardium shell from the blood pool. The selection of the 3D cylindrical samples (volumes of interest, VOIs) was designed. Six 3D holes were manually drawn from a copy of the heart shell mask; then by applying a boolean subtraction from the original mask the specimens were generated (Fig 3.15, panel 3). The VOIs were drawn above and below the four-chamber view in the axial plane: three were selected on the IVS, and the other 3 on the LVFW. In each region, one specimen was taken close to the valvular plane, one at the apex and one at the midpoint between them (Fig 3.15, panel 4).

The volume of each specimen was computed as:

$$SampleVolume = \frac{\pi}{4} * D^2 * PS^2 * ST * NSlices \tag{3.1}$$

where D is the diameter of the cylinder section and $NSlices$ is the number of slices and the six VOIs were selected for further analysis if their volume was $1[cc]$ with a tolerance of 15%. If this constraint was not fulfilled, the specimen selection was repeated. The HU values were then exported.

For each subject, a densitometric profile, a histogram of the HU distribution normalized to the total number of pixels, was drawn for both regions (Fig 3.15, panel 5). From the Gaussian-shaped profile, seven parameters were computed and used to create a densiometric profile: HU mean, median and mode measure the average CT absorption value of cardiac specimens; peak amplitude and HU standard deviation (HU std) assess the arrangement of muscle, fat and connective tissue components, as well as skewness and kurtosis (Fig 3.15, panel 6). In a second study concerning tissue composition, the percentages of fat ($[-200; -20]$ HU), connective tissue ($[-20; +20]$ HU) and muscle ($> +20$ HU) were extracted from the densitometric profile (Fig 3.15, panel 7). Thresholds are based on previous studies and experimental data [183], [184].

3.1.2.3 Statistical analysis

Data were analyzed using a linear mixed model, a generalization of the linear regression model, relaxing the assumption that the errors are independent and therefore, uncorrelated. Since our experimental design had multiple measurements from different regions within each subject, correlation within-subject data had to be accounted for [185].
R [186] and lme4 [187] were used to perform a linear mixed model with the seven densitometric parameters as dependent variables and pathology and region as fixed effects. Interaction effects between independent variables were also considered. We specified a model with a random intercept and unstructured covariance structure using Restricted Maximum Likelihood (REML). $P - values < 0.05$ were considered statistically significant and Satterthwaite's approximation was implemented to calculate degrees of freedom [188].
The assumption of normality was checked using the Shapiro-Wilk test of normality. Additionally, to further explore any significant effects identified in the previous analyses, we conducted simple contrast analyses with Bonferroni correction using the emmeans package.

3.1.3 Results

Intraventricular septum resulted a denser structure than the left ventricular free wall in the control group ($+15HU$, $p < 0.01$ with HU mean, mode and median), but not in the pathological subjects ($p > 0.05$), as shown in Figure 3.2. Shape parameters did not show any statistical difference among groups.

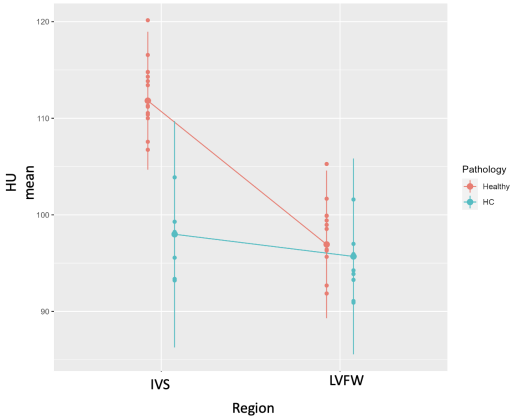

Figure 3.2: Densitometric parameter: HU mean as the output of the linear mixed model showing the higher density measured on IVS for the control (healthy) group. HCM showed a different densitometric behavior, having similar values on both IVS and LVFW.

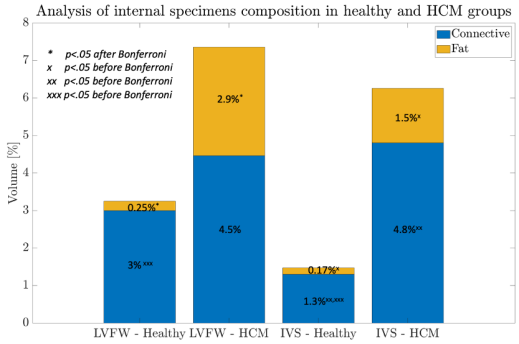

Figure 3.3: Tissue composition comparison: fat content is significantly higher in LVFW of HCM group whereas is absent in control group. Similar situation on IVS with lower percentages. Also the connective tissue increments with the pathology.

Fat and connective tissue percentages are reported in Figure 3.3. The control group reported less than 0.3% of fat in both regions. Connective tissue is around $3\% \pm 0.6\%$ in LVFW and drops to $1.3\% \pm 0.7\%$ on IVS. HCM group, instead, had less muscle with $2.90\% \pm 0.5\%$ fat and $4.5\% \pm 0.5\%$ connective in LVFW and $1.5\% \pm 0.7\%$ fat and $4.8\% \pm 0.5\%$ connective in IVS. The increase of fat in the LVFW in HCM group was statistically significant ($p < 0.001$), whereas the other comparisons lost the significance after Bonferroni correction (Figure 3.3, * and ^{x} symbols).

Tissue composition changes could be seen from the 3D densitometric profile as shown in Figure 3.4.

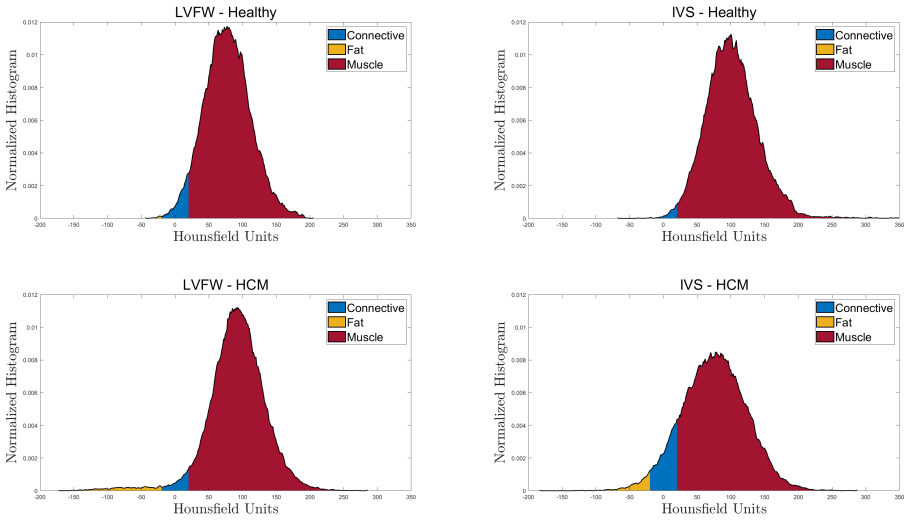

Figure 3.4: Patient-specific 3D profiles of a healthy subject (first row) and an HCM subject (second row). The three tissue types are drawn with different colors. A tail in the LVFW - HCM profile represents the presence of the pathology, the onset of non-muscular tissue. Also in IVS (right column), the pathological profile reports more fat tissue than the healthy one.

3.1.4 Discussion

Our results obtained analyzing densitometric profiles showed IVS as a denser (HU mean, mode and median) tissue compared to LVFW, as confirmed by the anatomical references [189]. The different transmural fiber alignments did not seem to impact the measured parameters.

In HCM subjects differences between IVS and LVFW were not reported suggesting a characteristic densitometric value for both regions different from what was found in the control group. Indeed, due to different CT scanners, the lower density of IVS in the HCM group may not be due to the pathology.

Looking at the sample composition, there are no universally accepted threshold intervals. Among what is reported in the literature, authors agreed on: (1) a more conservative threshold for muscle (+20 HU); (2) a symmetrical range for connective tissue composed mainly of water around 0 HU and decided (3) to label everything below −20 HU as fat to have a realistic representation of what a normal septum is and what HCM hearts report. A statistical significance in the volume of fat is found among healthy and HCM, meaning that the signs (fibrosis with fat deposition [190]) may be assessed and quantified with the technique.

3.1.5 Conclusion

As far as we know, this is the first study proposing the use of virtual histology from CT imaging to evaluate densitometric parameters and assess cardiac tissue composition in healthy and diseased hearts. The comparison of fat and connective compounds between healthy and HCM subjects showed significant differences and might be considered be a marker to detect the presence of CVD. Following a more comprehensive validation on

a larger population, also considering other cardiac diseases, the proposed non invasive approach might improve clinical diagnosis derived from CT imaging.

3.2 Virtual Cardiac Histology: Towards a Radiodensitometric Characterization of Left Ventricular Cardiac Muscle in Healthy and Pathological Conditions

Abstract

Background and Objective: Cardiovascular imaging plays a crucial role in disease understanding and case severity. Despite good results in morphological assessment due to an elevated spatial resolution, functional evaluation about cardiac tissue status is still lacking. The aim of the work was to perform a virtual cardiac histology, meaning to characterize cardiac tissue of the left ventricle with Computed Tomography images and use densitometric distribution to detect the presence of cardiac diseases such as acute myocardial infarction and hypertrophic cardiomyopathy.
Methods: The study retrospectively analyzed volumetric data from sixty subjects, equally distributed among classes, developing a pipeline of image processing for the semi-automatic extraction of 3D virtual samples from different levels and segments. From each sample's densitometric profile, a set of statistical descriptor were extracted.
Results: The densitometric characterization detected heterogeneity in the left ventricular tissue, differentiating the more conductive myocytes of the septum with the more contractive myocytes of the other segments. In addition, a gradient of radiodensity was found as moving from the valvular plane (basal) to the apex of the heart. The intraventricular septum was also found as an eloquent structure in pathological changes due to myocardial infarction since a geometrical modification and shift of the profile was observed (Amplitude = 0.02, Muscle HU = 57). The hypertrophic cardiomyopathy caused significative changes in the contractile segments intensity (Muscle 5-7 HU increase) and shape of the profile (Amplitude = 0.21 inferior wall) reporting the absence of physiological fat and connective tissue in those segments (fat volume = 0.2 %).
Conclusion: This study introduces a novel methodology leveraging CT densitometric properties to characterize left ventricular myocardium and distinguish healthy from pathological tissue. Significant patterns associated with hypertrophic cardiomyopathy and acute myocardial infarction highlight the potential of this approach for cardiac risk stratification.

3.2.1 Introduction

Cardiovascular imaging still remains one of the largest field where radiological evaluations are essential in the understanding and tracking of different pathological conditions ([191]). Despite a common symptomatology, the hidden causes may vary widely and having the right tool to "see inside" is crucial for patient treatment policy. Among the several imaging acquisition modalities, the high resolution of computed tomography (CT) has allowed investigation of blood vessels morphology, particularly in coronary

artery diseases (CAD) where a fatty plaque (atherosclerosis) might partially or completely obstruct the flow of the vessels. Angiography is widely requested since CAD, similarly to cancers, is one of the leading cause of death and morbidity in occidental population ([192]). Following the occlusion of the lumen, a damage in the myocardial muscle can be observed due to shortage of blood supply and a consequent reduced perfusion leading to abnormalities in motion and thickening of the injured myocardium ([193]). Dynamic, or 4-D CT scans are routinely performed to have a functional study over a beat and assess segments geometry and motion. In the last decade, quantitative cardiac imaging researchers have developed several tools from CT images to provide reliable assessment regarding myocardial ischemia, cardiac mass and left ventricle function ([194]–[196]). Moreover, heart's chambers geometry and volume may be quantified with CT imaging ([197]). It is particularly useful in the case of hypertrophic cardiomyopathy (HCM) where the excessive thickening of the left ventricle can be associated with remodeling of the hearts shape and normal geometrical relationship to ensure a good blood outflow ([198]).

Despite the physics behind x-ray absorption, it remains difficult to provide quantitative measurement about cardiac tissue properties from CT images. The research on pixel intensity and their spatial relationship in the image, known as radiodensity and radiomics, has faced a widespread growth in the last five to ten years ([44]). Focus has shifted from the entire image to key region of interest crucial for understanding pathophysiology. These tools excel in predicting and describing pathological tissues by looking beyond the image, advancing quantitative assessment not evaluated conventionally and unconventionally ([199]). In 2020 a review paper reported that almost the 61% (n=71) of the included studies using radiodensity were focusing on cancer patients and only a small portion on non-communicable and neuromuscular diseases, but in the 81% of the cases the radiodensity assessment was on the skeletal muscle quality ([200]). Edmunds et al. proved that a rigorous quantification of midthigh muscle with Hounsfield Units (HU) distributions assesses sarcopenic degeneration and correlates with lower extremity function and biochemical variables in aging population ([97]). The same technique was then capable of predicting five years in advance the onset of a coronary artery disease, heart failure and cardiovascular diseases with an accuracy of almost 80% starting from the same region of interest ([182]). In particular, the fat content was the most important feature when analysing the machine learning performances, being used almost half of the time (41%) in the final prediction ([182]). Similar approaches based on radiodensity were applied to assess skeletal muscle quality in oncological patients, offering a quantitative prognostic information about the survival chances ([201], [202]). Furthermore, the quantity of epicardial fat was correlated with vascular calcification in woman and a lower radiodensity can be a marker for a less favorable cardiac profile ([203]). The radiodensity and volume of epicardial fat was also related to the mortality of patients with end-stage renal disease ([204]). In summary, the prognostic value of epicardial fat is clear and out of doubt, but a similar assessment for the intramuscular fat and connective tissue remains elusive.

The main objective of the presented work is to prove the applicability of pixels intensity technique on cardiac CT to characterize healthy and diseased tissues, to replicate a histological examination from medical imaging, thus virtual. For this purpose, two different pathologies such as HCM and acute myocardial infarction (AMI) were chosen due to the modification caused in the myocardial tissue and their different localization where HCM is a more generalized disease whereas AMI is localized to a specific infarct vessels site. This approach is unique and could open to insight about tissue qual-

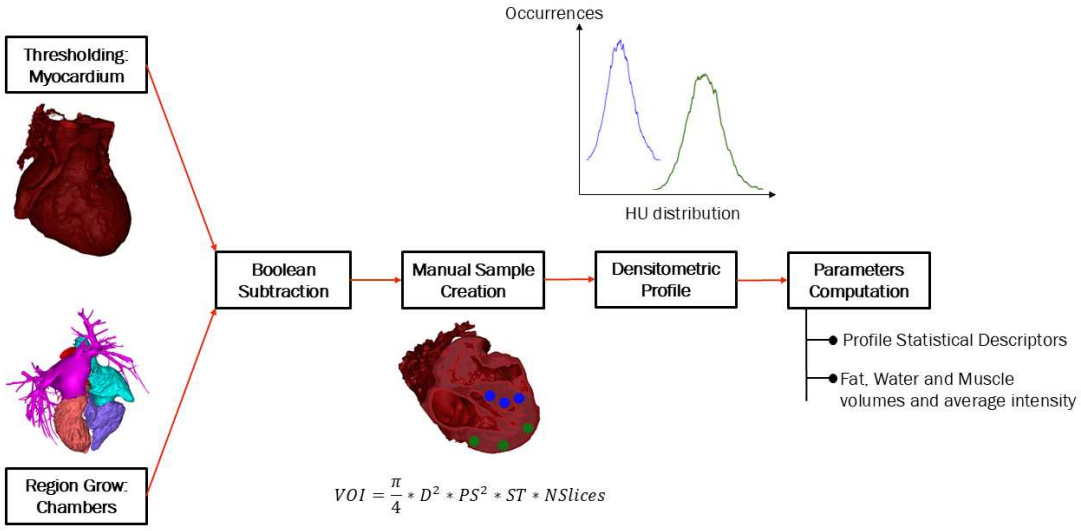

Figure 3.5: Operative workflow: from image analysis to parameters computation. From the original image, two different masks were created: one for the myocardium (thresholding and atlas based) and one for the blood pool inside heart chambers. After a boolean subtraction of the latter from the former, a manual editing step to create the cylinder was taken. Then HU values were exported and densitometric profile recreated in Python environment, where the features were finally computed. A more detailed description was provided before [205].

ity even without magnetic resonance examination, the only assessment of this kind. Tissue characterization could then be linked to other morphological and clinical risk factors to track the development of conditions and anticipate their diagnosis becoming a quantitative supportive clinical tool. This methodology would also apply in studying the aging of a healthy cardiac muscle, quantifying the effects of different life styles including for instance the impact of smoke and cholesterol.

3.2.2 Methods

3.2.2.1 Population

Sixty subjects that underwent CT scan by request of their medical advisor were retrospectively enrolled in this study. The study population was stratified according to the outcome of CT diagnostic test: twenty individuals were negative on CT imaging , used as control group (C), twenty were diagnosed with HCM and the last third with AMI. The demographic and anthropometric characteristics of the three groups are reported in Table 3.1.

3.2.2.2 Image Acquisition

Cardiac CT volumetric data of sixty different subjects were retrieved from SynLab PACS system (Gianturco, Naples, Italy). Data were acquired with a Siemens Somatom Force scanner, with a Cardiac CT Retro (ECG triggered) Functional Cinematic acquisition protocol. For each subject, two volumes were extracted: 1) diastole

Group	Males	Age	BMI	BSA	Obesity	Familiarity	Smoke	Diabetes	Statins
C	11 (55%)	56.4 ± 11.85	29.24 ± 5.11	1.95 ± 0.22	6 (30%)	14 (70%)	6 (30%)	1 (5%)	8 (42.11%)
AMI	17 (85%)	64.9 ± 10.64	27.45 ± 4.10	1.96 ± 0.18	5 (25%)	10 (50%)	5 (25%)	3 (15%)	18 (90%)
HCM	15 (75%)	68.15 ± 11.63	29.41 ± 5.18	1.98 ± 0.25	9 (45%)	8 (40%)	2 (10%)	3 (15%)	12 (60%)

Table 3.1: Study population characteristics divided by group - Risk factors as value (percentage) in that population, numerical parameter as average ± standard deviation.

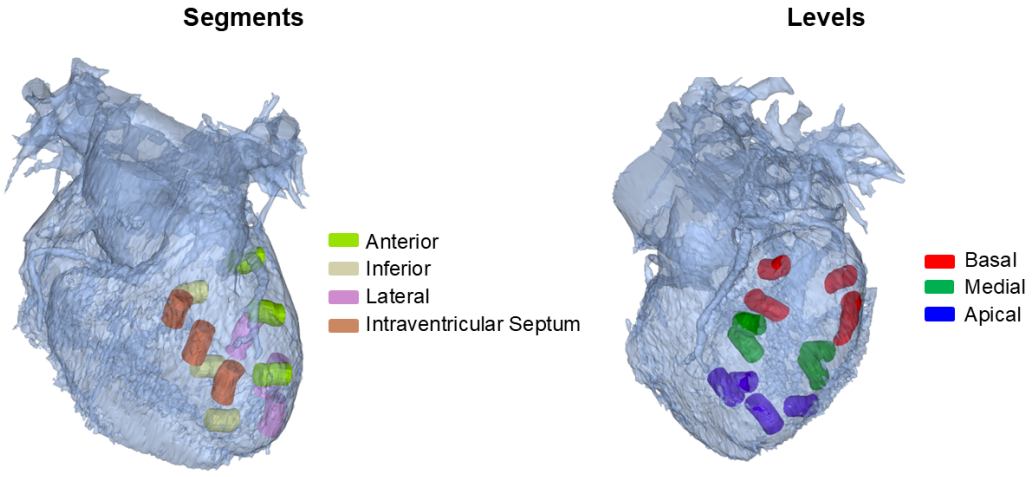

Figure 3.6: Sampling Areas: twelve positions were identified and localized to make the procedure repeatable. The four segments of the left ventricle (Anterior, Inferior, Lateral and the Intraventricular Septum) were sampled in the basal, medial and apical levels for a total of twelve sample from each heart. Segments and levels were used for further analysis in characterizing the myocardial tissue.

with contrast medium in at least the left ventricular chamber and 2) diastole without contrast media to extract samples. The need for the second volume is because of the effect of contrast media on cardiac muscle pixels brightness ([206]). Images parameters such as pixel size and slice thickness varied in $[0.25 - 0.40]$ mm and $[0.20 - 0.33]$ mm ranges, respectively. The radiological team pre-selected the images and exclude data with ghosting artifacts mainly due to cardiac motion.

3.2.2.3 Image Processing

The image processing pipeline got the cardio CT with contrast media as an input and it returned HU values describing the cardiac tissue. The workflow was developed in Mimics 26.0 (Materialize, Belgium). The pipeline for left ventricle segmentation and samples extraction was previously described ([205]). Briefly, each sample was isolated by manually designing a cylinder of 1 cc from a mask of the entire myocardium that was previously edited with boolean subtraction of the blood pool to ensure myocardium isolation. In this work, sampling was extended to achieve a mapping more similar to the AHA 17-segment model (American Heart Association 17-segment model) ([207]). Four different segments of the left ventricle: lateral and inferior from a coronal two-

chamber view, septum and lateral from a four-chambers axial view. The samples from each segment were extracted at three different levels: the basal plane, at the apex of the ventricle and at the middle point, as shown in Figure 3.6, resulting in twelve cubic centimeters of non-overlapping volume sampled for further analysis. This combination allowed to cover the entire left ventricle ensuring a trade-off between representativeness and size of the samples, especially avoiding partial volume effect, in accordance with areas from the radiological reports. To avoid brightness influences from contrast media inside the chambers, a rigid registration step of the second non-contrasted diastole volume on the contrasted one was performed to align the anatomies. The two dataset, from the same acquisition, were first manually aligned and then the registration was performed, with an accuracy of the pixel size. The roto-translation matrix obtained from this step was inverted and then used to extract samples from the non-contrasted dataset. The HU values contained in the voxels of the twelve samples are exported into a text file with their spatial coordinates (X, Y, Z).
To avoid biases at the extraction phase, the image processing step was taken blindly, without knowing the condition of the heart.

3.2.2.4 Feature Extraction

The HU from each sample were used to create a histogram where the number of occurrences were normalized by the total amount of pixels from that sample. The resulting normalized histogram was called densitometric profile. The profile is generally a Gaussian-shaped bell that can be described by different statistical parameters:

- Position: Mean, Median and Mode.
- Shape: Skewness, Kurtosis, Amplitude and Width (Standard Deviation)
- Complexity: Entropy ([208])

The position parameters quantify the average radiodensity of the underlying tissue. The shape and complexity parameters gave a quantitative assessment about how the distribution vary around the peak ([209]). A mathematical formulation is reported in the appendix A.

In addition, six other descriptors were calculated to isolate different tissue types. Similarly to previous works, the HU values were divided by thresholds to identify fat, muscle and connective/water equivalent tissue ([97], [183], [184]). This work used the following intervals: -200 to -20 HU for fat, -20 to +20 HU for connective/water equivalent and +20 to +200 HU for muscular tissue, as proposed before ([205]). The number of pixels of the given tissue over the total amount from that volume was quantified for each tissue (FatVol, Water eq Vol, Muscle Vol). In addition, the average radiodensity of each tissue was calculated (Fat Density [HU], Water eq Density [HU], Muscle Density [HU]). A graphical representation of the densitometric profile with some extracted parameters was reported in Figure 3.7.

A database of 720 volumes of interest matched with the fourteen measured parameters was created and each sample was labeled both based on the class of the subject (C, HCM or AMI) and based on the status of the area (healthy or pathological) according to the clinical assessment.

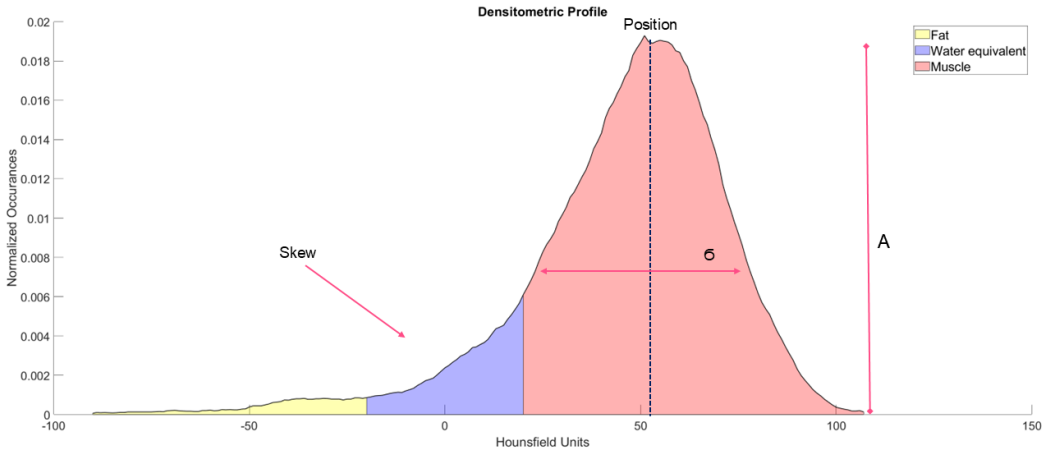

Figure 3.7: Densitometric Profile and extracted parameters: the profile represents the HU distribution and the three groups of statistical descriptors are extracted from it. The position group is drawn in dark blue whereas the position group is in violet. The profile was then divided in three regions according to the tissue type (fat, water equivalent and muscle). The amount of each tissue is computed, with respect to the total and their average HU is extracted.

3.2.2.5 Statistical Analysis

A normality test (Shapiro-Wilk test) was performed on each extracted sample to check the shape of the densitometric profile. Firstly, a study on the healthy population was carried out to create a reference model on how a healthy heart may be characterized with a densitometric approach. A correlation analysis was performed among the extracted parameters and the age to study the inter-parameter effects. Then a mixed linear model was fit onto the experimental data using age, sex, segment and region as fixed effects and the addition of a random effect to take into account multiple samples from the same subjects.
Secondly, a correlation analysis was used to study the impact of aging in pathological hearts and to highlight potential changes from the healthy correlation among parameters. Moreover, a comparison analysis was performed to assess the impact of the pathologies onto the densitometric parameters. A Kruskal-segmentis test was used due to non-normal distribution of the parameters (Shapiro-Wilk's test p-value > 0.05) and the three groups nature problem. When this test returned statistical relevance (p-value $< .05$), a post-hoc Dunn's Test with Bonferroni correction was performed. The chain of tests reveals for each parameter if and among what groups they were statistically different. This analysis included only the pathological samples from pathological hearts and comparing them with the corresponding segment and region from healthy hearts.
Lastly, a validation analysis including the healthy samples from the pathological heart against the healthy hearts was performed to assess the effect of localized (AMI) and global (HCM) pathologies. In addition, a correlation analysis between BMI, BSA and volume of fat and water tissues.
A statistical significance equal to 0.05 was set.

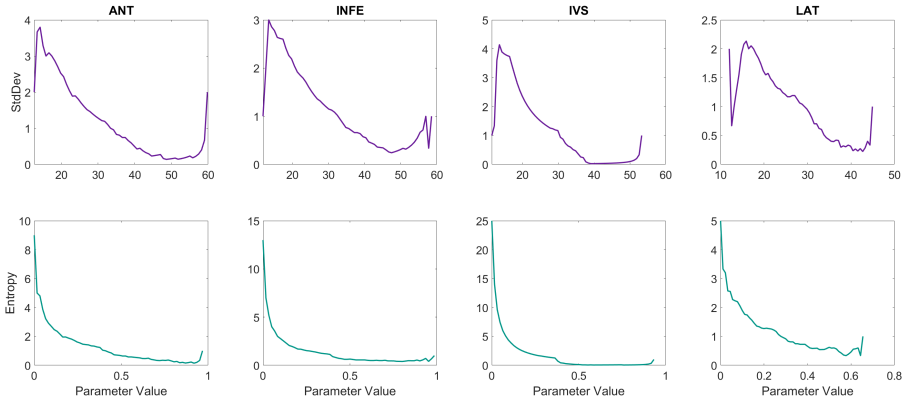

Figure 3.8: Distribution of Standard Deviation (top) and Entropy (bottom) parameters in different segments over the healthy control group. Notably, the intraventricular septum has the higher entropy with less variance and the lateral segment is the more homogeneous due to lower entropy.

3.2.3 Results

The analysis was feasible for all the sixty subjects, so we did not exclude any of those and overall the average computational time was between two and ten minutes for the image processing and about five minutes for the computation of the twelve features from all the cohort. Segmentation and data extraction was performed on a commercial tower computer with a dedicated graphic card (NVIDIA GeForce RTX 3070).

3.2.3.1 Healthy Densitometric Heart

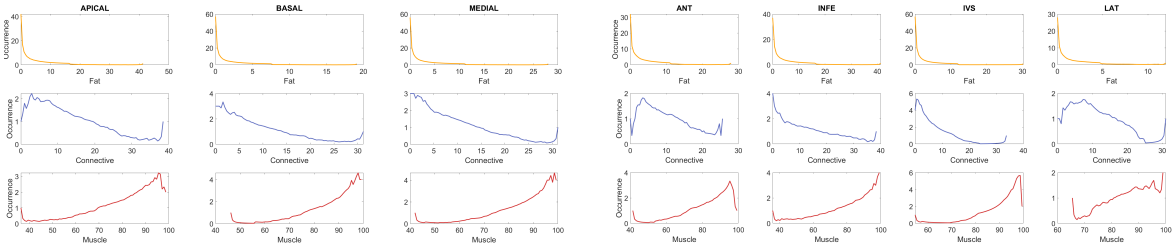

(a) (b)

Figure 3.9: Volume partition as percentage of 1 cubic centimeter, in Fat (yellow), Water (blue) and Muscle (red) over different areas of the left ventricle by level (a) and by segment (b). The apical level has the higher content of fat, whereas the septum has almost no fat but a higher content of water.

The correlation analysis reported no influence of aging onto the measured densitometric parameters. The position of the peak was negatively correlated with its own variability and complexity (standard deviation and Entropy) and the amount of non-muscular tissues in the sample (fat volume, water volume) but positively correlated with muscle percentage and muscle density. On the other hand, the width of the peak and the entropy reported positive correlation with the volume of fat and connective tissues. Skewness was negatively correlated with kurtosis. A minor correlation was also reported among the amplitude of the peak and the content of connective tissue (negative) and muscle (positive). All the results and p-value are reported in Table 3.2.

Variable	Age	Mean	Mode	Median	StdDev	Entropy	Skewness	Kurtosis	Amplitude	FatV	Water V	MuscleV	Avg Fat HU	Avg Water eq HU	Avg Muscle HU
1. Age	Pearson's r	–													
	p-value	–													
2. Mean	Pearson's r	0.060	–												
	p-value	0.355	–												
3. Mode	Pearson's r	−0.003	0.720	–											
	p-value	0.958	< .001	–											
4. Median	Pearson's r	0.045	0.959	0.818	–										
	p-value	0.490	< .001	< .001	–										
5. StdDev	Pearson's r	−0.126	−0.790	−0.321	−0.622	–									
	p-value	0.051	< .001	< .001	< .001	–									
6. Entropy	Pearson's r	−0.102	−0.882	−0.483	−0.764	0.908	–								
	p-value	0.115	< .001	< .001	< .001	< .001	–								
7. Skewness	Pearson's r	0.074	0.441	0.178	0.302	−0.578	−0.558	–							
	p-value	0.256	< .001	0.006	< .001	< .001	< .001	–							
8. Kurtosis	Pearson's r	−0.033	−0.225	−0.104	−0.148	0.327	0.278	−0.911	–						
	p-value	0.607	< .001	0.106	0.022	< .001	< .001	< .001	–						
9. ModeRatio	Pearson's r	0.130	0.439	0.225	0.404	−0.632	−0.575	0.010	0.128	–					
	p-value	0.044	< .001	< .001	< .001	< .001	< .001	0.873	0.048	–					
10. FatV	Pearson's r	−0.088	−0.820	−0.335	−0.690	0.875	0.859	−0.386	0.147	−0.493	–				
	p-value	0.175	< .001	< .001	< .001	< .001	< .001	< .001	0.022	< .001	–				
11. Water_eqV	Pearson's r	−0.092	−0.814	−0.679	−0.830	0.644	0.812	−0.298	0.121	−0.624	0.538	–			
	p-value	0.154	< .001	< .001	< .001	< .001	< .001	< .001	0.062	< .001	< .001	–			
12. MuscleV	Pearson's r	0.104	0.929	0.622	0.881	−0.836	−0.940	0.382	−0.154	0.646	−0.814	−0.927	–		
	p-value	0.107	< .001	< .001	< .001	< .001	< .001	< .001	0.017	< .001	< .001	< .001	–		
13. Avg Fat HU	Pearson's r	0.173	0.576	0.172	0.379	−0.774	−0.634	0.851	−0.685	0.156	−0.590	−0.239	0.471	–	
	p-value	0.049	< .001	0.050	< .001	< .001	< .001	< .001	< .001	0.076	< .001	0.006	< .001	–	
14. Avg Water eq HU	Pearson's r	0.038	0.683	0.335	0.588	−0.751	−0.847	0.594	−0.356	0.512	−0.632	−0.697	0.757	0.513	–
	p-value	0.557	< .001	< .001	< .001	< .001	< .001	< .001	< .001	< .001	< .001	< .001	< .001	< .001	–
15. Avg Muscle HU	Pearson's r	−0.057	0.747	0.831	0.820	−0.258	−0.446	0.305	−0.221	−0.006	−0.281	−0.597	0.543	0.227	0.336
	p-value	0.381	< .001	< .001	< .001	< .001	< .001	< .001	< .001	0.932	< .001	< .001	< .001	0.009	< .001

Table 3.2: Pearson's Correlations r and associated p-values in the analysis on healthy hearts

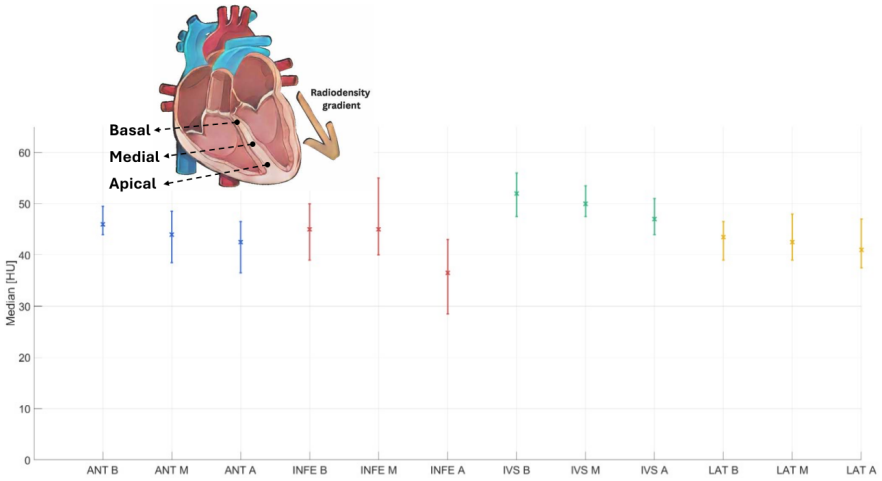

Figure 3.10: Median radiodensity from the extracted areas as combination of segments (Anterior - Inferior - Intraventricular Septum - Lateral) and levels (Basal - Medial - Apical). A gradient in HU median was reported in every segment from Basal to Apical level.

The linear mixed models reported that the intraventricular septum segment had a higher radiodensity (50 HU on average) compared to the other segments (Mean, Mode, Median with p-value $< .05$) and its complexity and standard deviation resulted significantly lower (p-values $< .05$) (Figure 3.8).

The apical region reported as less radiodense compared to other levels (Basal and Medial) with a typical 40 HU as average. A graphical representation of the gradient in median radiodensity over different levels is reported in Figure 3.10. The intraventricular septum reported an asymmetry in its profile as well as no volume of fat in the basal and medial levels, where the other segments had a statistically higher contribution (Fat Vol p-value $<.05$ on both segment and region). Similarly, the content of connective tissue was principally found in the inferior segment, especially in the apical region while the septum was characterized by the less content of connective tissue (Connective Volume p-values $<.05$ on both segment and region). A summary of tissues volume distributions is reported in Figure 3.9, split by Region (Figure 3.9a) and segment (Figure 3.9b).
The validation analysis on the healthy samples from pathological subjects reported the average muscle density in the apical level was the only parameters found statistically different (p-value $<.05$ apical against medial and basal levels) from HCM group. No differences were observed in other locations for HCM nor in AMI subjects.
The correlation analysis on the volume of fat and water with BMI and BSA on healthy subjects reported no linear correlation or inconclusive results due to p-value above the significant value. (BMI: r = -0.04, p-value = 0.39; r = 0.13, p-value < 0.005; BSA: r = -0.05, p-value = 0.24; r = 0.06, p-value = 0.13 fat and water, respectively)

3.2.3.2 Pathological Hearts

Correlation analysis on the subcohort of pathological subjects reported no correlation among age and radiodensitometric parameters. The one with the volume of fat and water with BMI and BSA reported no clear correlation between the parameters (Fat Volume - BMI: r = 0.20, p-value = 0.07; r = 0.06, p-value = 0.58; Fat Volume - BSA:

Statistical Test	Shapiro-Wilk's	Linear Mixed Model	Kruskal-Wallis Dunn post-hoc
HU mean	*	IVS - Apical	C-HCM
HU median	*	IVS - Apical	C-HCM
HU mode	*	IVS - Apical	C-HCM
StdDev	*	IVS	C-AMI
Entrompy	*	IVS	C-AMI
Skewness	*	IVS	C-HCM C-AMI
Kurtosis	*	No Significance	C-HCM
Amplitude	*	No Significance	C-HCM C-AMI
Muscle Volume	*	No Significance	No Significance
Water Volume	*	INF	No Significance
Fat Volume	*	IVS - Medial, Basal LAT, INF, ANT	C-AMI
Muscle Density[HU]	*	No Significance	C-HCM
Water Density[HU]	*	No Significance	C-AMI
Fat Density[HU]	*	No Significance	No Significance

Table 3.3: Extracted parameters and statistical tests. Shapiro for normality: * not normal distributed. Linear mixed model: segment and level where the parameter was found significant. Kruskal-Wallis and Dunn post-hoc: couple of conditions were the parameter was found significant. No significance otherwise.

r = 0.20, p-value = 0.06; r = -0.32, p-value < 005, HCM and AMI, respectively). No major changes in other correlation Pearson's coefficients and p-values. Major changes caused by pathologies over radiodensitometric parameters are reported in Figure 3.11.

Hypertrophic Cardiomyopathy HCM samples revealed that the muscle had increased radiodensity (mean, mode, median p-values <.05) in the anterior and lateral segments (Figure 3.12a). The amplitude of the peak decreased, with a consequent but not signification increment in variability (Amplitude p-value <0.05, StdDev p-value >.05, kurtosis p-value <.05) especially in the inferior and lateral segments (Figure 3.12b). The latter it was also characterized by a less negative skewness (p-value <.05), thus profile seemed more symmetric. The region analysis revealed that the muscle radiodensity was higher in basal and apical areas (p-values <.05, Figure 3.13a), and the former was also characterized by a lower amplitude of the profile (p-value < .05). No statistical changes were registered in the intraventricular septum (IVS).

Comparison analysis among healthy samples from HCM hearts and healthy hearts revealed no statistical changes in segments, while the apical region was characterized by a higher radiodensity and a more symmetrical profile' shape (p-values < .05) (Figure 3.13a).

Acute Myocardial Infarction Despite having pathological samples from the four segments, statistical changes were recorded in IVS only. The AMI samples belong-

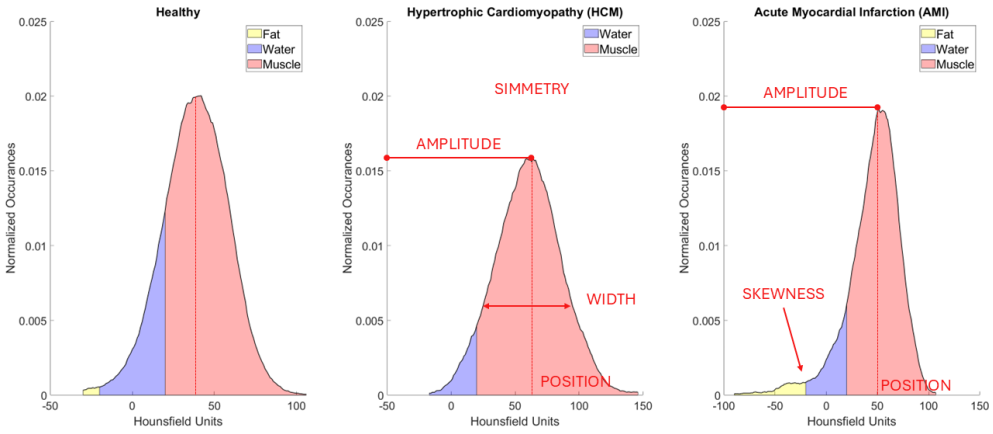

Figure 3.11: Effect of pathologies on the densitometric profile: statistically relevant parameters and their geometric meaning on the densitometric profile by pathology and a healthy profile as a reference.

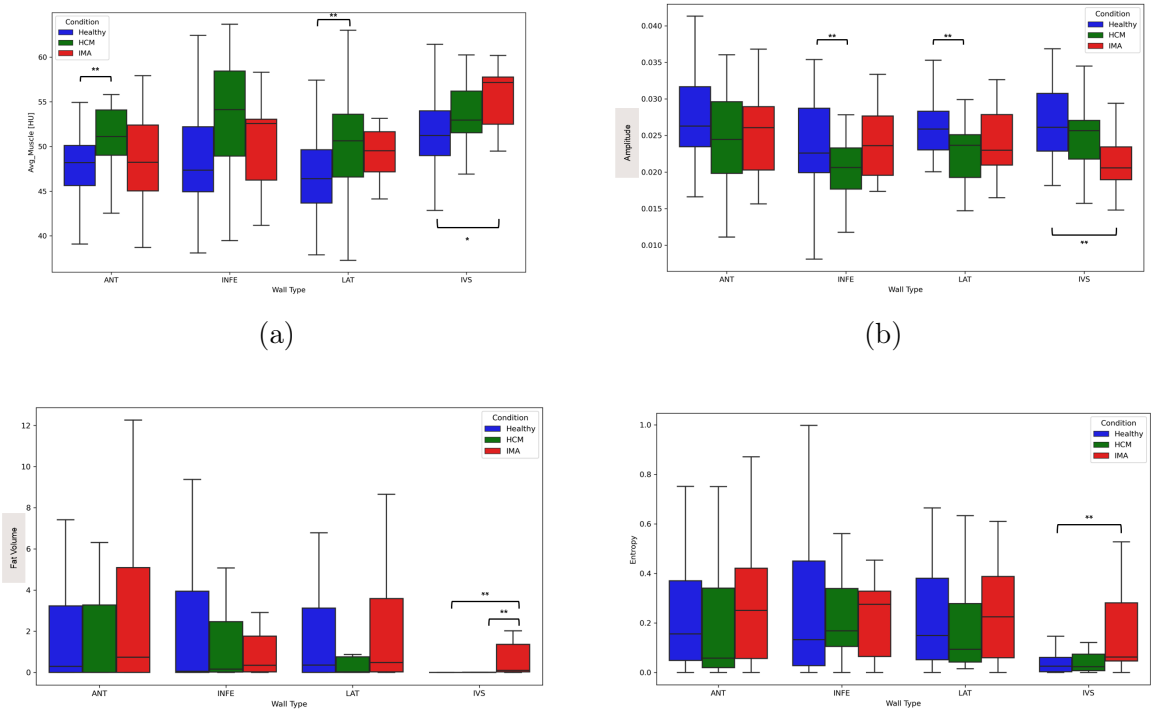

Figure 3.12: Radiodensitometric Analysis of HCM (green) and AMI (red) samples matched with Healthy (blue) control reference by segment. $*$ p-values equal 0.06; $**$ p-values below 0.05. (a) Muscle Density analysis: increased muscle density in all the segments (HCM) (b) Amplitude analysis: profile amplitude reduction in HCM patients; (c) Fat Volume analysis: fat detection in the septum of AMI patient and (d) Entropy analysis: increased entropy in the septum of AMI patient as a result of fat infiltration due to infarction event.

ing to this segment reported an incremented variability (StdDev p-value<.05) and higher entropy (p-value<.05), the profiles had decreased amplitude and skewness (p-value<.05)(increased asymmetry to the negative side of the HU spectrum) (Figure 3.12b). The radiodensity of connective tissue decreased (Connective HU p-value <.05). A trend in incremental muscle radiodensity was found (p-value = 0.07, Figure 3.12a) whereas an a significant increment of fat deposition happened (p-value <.05), mainly in the medial region (p-value <.05) (Figure 3.13b). In the same area, the entropy increased significantly (p<-value <.05).

The control analysis between healthy samples from the two groups (AMI vs. Healthy) reported no statistical changes in the parameters.

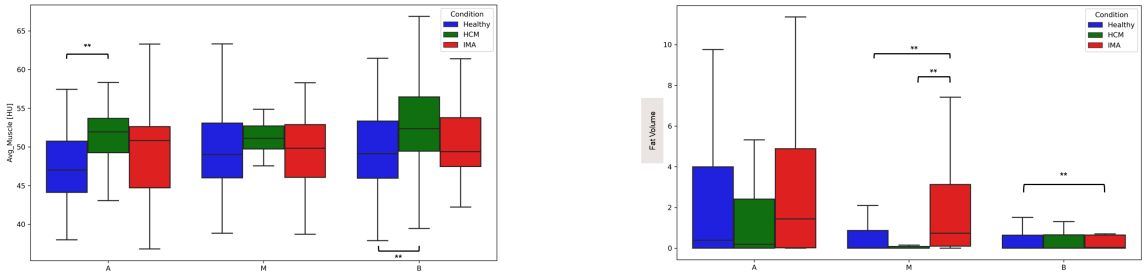

(a) (b)

Figure 3.13: Radiodensitometric Analysis of HCM (green) and AMI (red) samples matched with Healthy (blue) control reference by Level. ∗ p-values below 0.10; ∗∗ p-values below 0.05. (a) Muscle Density analysis; (b) Fat Volume analysis. The effect of pathological condition may be observed at different levels with an increase in muscle radiodensity both basally and apically (HCM) and the presence of fat medially for AMI patients.

3.2.4 Discussion

The intricate structure and functional heterogeneity of myocardium pose significant challenges for diagnostic imaging. Traditional approaches often begin with clinical assessments like symptom evaluation and electrocardiograms (ECGs), followed by echocardiography as the primary imaging modality. For more comprehensive evaluations of cardiac conditions, advanced imaging techniques such as cardiac computed tomography (CT) and cardiac magnetic resonance imaging (CMRI) are often employed. CT, particularly, is recommended as a first-line test in chest pain management due to its ability to detect coronary artery disease (CAD) with high diagnostic confidence ([210]). The latter is mainly requested to assess myocardial structural and functional changes as well as quantifying fibrosis and fat infiltration with a lower spatial resolution but no ionizing radiations ([154]). The purpose of this study was to demonstrate that the tissue characterization approach is feasible with CT data that provide additional information on the diagnostic path. This could prove important in clinical practice because CT is more readily available than cardiac MRI (CMRI).
This study aimed to demonstrate that tissue characterization using CT data is not only feasible but also provides additional diagnostic information. The key findings of this research emphasize the importance of the densitometric profile, which not only serves to characterize healthy cardiac muscle and study its physiological radiodensity

variability, but also reveals distinctive patterns in various pathologies. For example, in diseased states, we observed a shift toward higher radiodensity values, a reduction in amplitude, and an increase in profile width, all of which altered the typical Gaussian geometry seen in healthy profiles. These findings align with the idea that CT-based densitometric profiling can effectively differentiate between normal and pathological myocardial tissues, offering a non-invasive approach for diagnosing and monitoring heart diseases. For example, virtual cardiac histology may detect subtle changes in myocardial tissue composition and organization reflected in parameters such as amplitude, skewness and average radiodensity and identify pathological alterations before clinical symptoms appear or other imaging modalities can detect them. To further investigate the predictive power of these features, an ad hoc cohort need to be enrolled. This methodology can provide additional information during angio-CT and assessing coronary artery status that remains one of the most frequent examination worldwide.

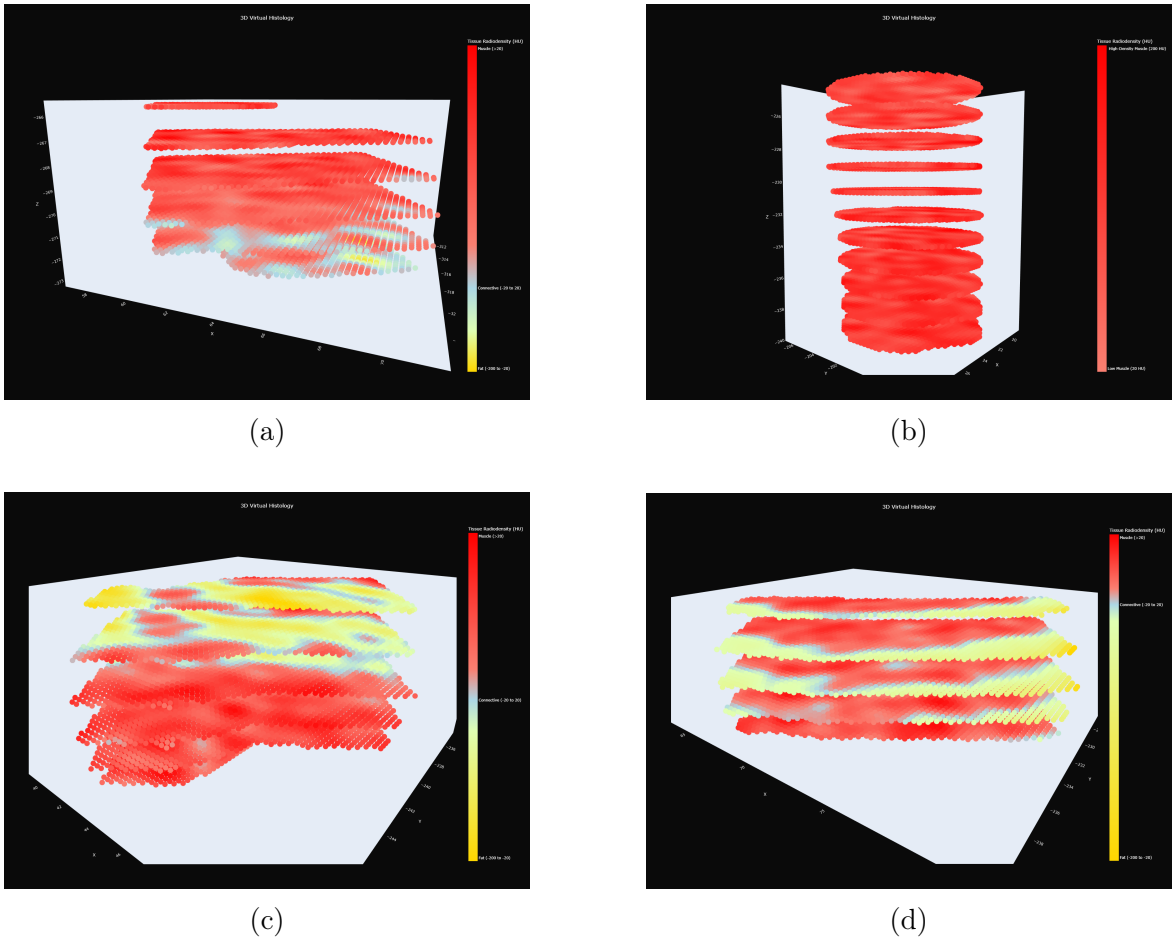

(a) (b)

(c) (d)

Figure 3.14: 3D Virtual Histology renders: HU to tissue-colored mapping enables visual comparison of healthy and diseased samples. (a) Render of a healthy specimen from the inferior apical segment of an healthy subject. (b) Render of a healthy specimen from the intraventricular septum of an healthy subject. (c) Rendering of a diseased specimen from a subject with hypertrophic cardiomyopathy. The subject is a 40 years old male with 20% fat tissue in the sample's volume. (d) Render from an AMI subject of the anterior apical segment specimen. The subject is a 60-year-old male with 13% fat tissue in the sample's volume.

The initial analysis highlighted the heterogeneity of cardiac muscle in the left ventricle, with particular emphasis on the intraventricular septum, which contains specialized cardiomyocytes for conducting electrical signals (Purkinje fibers). In contrast, the other segments primarily contribute to contraction activity. Figure 3.14 shows a render of the tissue types and their radiodensity by slices of specimens coming from healthy and pathological subjects. Panel 3.14a and 3.14b display the different composition and radiodensity of contractile and conductive cardiac tissue. Although the segments generally appear similar in radiodensity, they vary in thickness ([211]). Thus, extracted samples have generally different diameters to fit in the cross-section of the left ventricle, and the position may slightly change due to natural inter-subject variability.
The apical region resulted in less radiodense, as proven by ex-vivo heart histology that found sparser fibers in the mid-apex of the left ventricle ([211]). Particularly, IVS reported a gradient of radiodensity from the base to the apex, according to its own morphology and fiber arrangement (Figure 3.10) ([212]). To this purpose, having images in diastole reduces the complexity because the cardiomyocytes are not contracted so there are no modifications of the structures due to motion.

Aging is the largest risk factor for cardiovascular diseases ([213]). The major structural changes in cardiac aging are a thickening of the LV segment due to an increase in cardiomyocytes size ([214]) and a LV volume decrease with a preserved cardiac mass ([215]). As a result the mass/volume ratio (density) increases. Functionally this is most often reflected as impaired relaxation and disturbance of LV diastolic function. This hypertrophy although concentric, often asymmetrically affects the LV, mostly affecting the interventricular septum leading to a redistribution of cardiac muscle, explaining the lack of effect on total cardiac mass ([213]). The aging analysis proposed in this work showed no correlation between radiodensity parameters and age (Mean Pearson's $r = 0.06$ and p-value $= 0.36$). Nonetheless, the trend is positive, thus there is a slight increment in the overall average radiodensity in aged hearts, but not significant in this cohort. These results might be explained by the resolution of CT images that is not enough to detect single cardiomyocyte size. Further analysis on a larger population is needed to further investigate this finding.

The second part of the work was focused on the analysis of diseased samples. Despite the knowledge about the modification of the IVS in HCM ([190], [216]), our results indicated an increase in radiodensity in the inferolateral segments, as well as at the base and apex of the heart. This may suggest a compensatory remodeling mechanism in which structural changes occur to offset morphological alterations in the intraventricular septum and ensure preserved cardiac function ([217]). Figure 3.14c display the virtual histology render of a sample from the anterior segment that suffered fat and connective tissue infiltration.

HCM group reported a more symmetric profile, compared to the control group. In addition, the higher kurtosis highlighted the importance of the tails in these distributions. Since there were no statistical changes in the amount of fat and water in the right tail, the loss of asymmetry may be explained as an increased amount of pixels in the right tail, at higher Hounsfield values. Fibrosis, a typical condition of HCM patients, under the radiodensitometric point of view should be presented as more radiodense than muscle, falling to its right-side in a densitometric profile [218]. Thus, the combination of parameters may point out the presence of fibrosis in the extracted samples. Further studies will be needed to investigate this quantification.

A decade ago the idea of quantifing fibrosis from CT images was already present: Nacif et al. demonstrated a strong correlation between extracellular volume fraction (ECV) values measured by CT with geometrical and emodynamic parameters, supporting the potential of CT as a fibrosis assessment tool from a histological perspective in subjects with heart failure ([219]). This foundational work was further supported by Yamada et al., who showed that cardiac CT can reliably quantify ECV to assess myocardial fibrosis in hemodialysis patients, revealing a strong alignment between CT-derived ECV values and those obtained from CMR ([220]). More recently, Carbucicchio et al. (2021) broadened the utility of cardiac CT by demonstrating its effectiveness in characterizing left ventricular scarring through delayed enhancement techniques, which are useful for visualizing fibrosis-related scar tissue, as seen in conditions like ventricular tachycardia ([221]). Together, these studies outline a robust workflow for fibrosis characterization: beginning with histology to ensure accuracy, using CMR to validate findings, and ultimately applying CT as a practical, non-invasive method for fibrosis assessment across a range of clinical scenarios.

On the other hand, AMI is a localized disease that leads to focal tissue necrosis and modification primarily in the area of the infarction, and lately in the entire LV ([222]). The proposed analysis proved that for AMI, the IVS has a higher degree of fragility since it is the only one that reported statistical changes even though other segments were contributing with pathological samples. On average the pathological septum was characterized by a slightly denser tissue (p-value = 0.07, after Bonferroni correction) with an increased amount of fat, especially in the medial region that reflected in a modification in profile shape (decreased skewness, which means more asymmetry and lower amplitude). To support the finding, the amount of fat in the body (BMI) was not correlated with the fat volume inside the specimens, proving that its presence is due to the pathology. Figure 3.14d display the virtual histology render of a sample from the anterior segment that may detect part of a scar filled of fat tissue. The infarction led to different tissue organization locally, detected by an increased variability and complexity, which were otherwise very low in IVS. Since the population involved had an acute myocardial infarction we did not expect any major change or remodeling in the other areas, as it resulted from the analysis of healthy samples from pathological hearts against healthy hearts.

Virtual cardiac histology technique based on first order radiomics was able to design a signature behavior for both pathologies, that are unique and different. For instance, fat volume in IVS is typical of AMI while is almost absent in HCM, asymmetry decreased in AMI due to fat infiltration while a platykurtotic (lower kurtosis) profile characterized HCM, where fibrotic tissue may correspond to the higher density value in the right tail of the profile. Tissue characterization, coupled with geometrical evaluation, may enforce diagnostic power of image-based tools ([223]).

Although the study demonstrated promising results, several limitations were noted, including CT's resolution constraints in detecting subtle changes like cardiomyocyte hypertrophy, the need for larger, age-diverse cohorts to explore aging-related radiodensity changes, and the necessity to refine fibrosis quantification techniques with advanced radiomic features. Importantly, one of the key limitations of our study is the relatively small therefore our results would need confirmation on a bigger cohort.

3.2.5 Conclusion

Virtual cardiac histology leverages CT's accessibility and spatial resolution to provide actionable insights into cardiac tissue pathology. This project proposed a novel methodology for characterizing left ventricular myocardium, utilizing densitometric properties extracted from CT images. The proposed approach demonstrated the potential of densitometric properties derived from CT images in distinguishing healthy myocardium from pathological cases by identifying specific densitometric patterns in the conductive and contractile myocardium. Notably, significant alterations in these patterns were observed in hypertrophic cardiomyopathy (HCM) and acute myocardial infarction (AMI), underscoring the potential of this method in detecting and assessing cardiac diseases. These findings suggest that densitometric properties could serve as additional functional markers for cardiac risk stratification, enhancing the diagnostic utility of medical imaging. Future work should focus on validating this method with larger and different populations. Additionally, the integration of advanced radiomic features, could also be investigated to enhance the classification of cardiac tissue and to support the development of a comprehensive numerical index to quantify healthy tissue and assess disease risk with greater precision.

3.3 Multi-Domain Radiomics Analysis of Virtual Cardiac Histology Samples: A Predictive Model for Hypertrophic Cardiomyopathy

Abstract

This study demonstrates the application of radiomic-based machine learning models for hypertrophic cardiomyopathy (HCM) classification using CT imaging. By integrating multidomain radiomic features and anthropometric data, we trained Light Gradient Boosting (LGB) and Quadratic Discriminant Analysis (QDA) ensembles while addressing class imbalance with focal loss. Subject-based classification improved with combined features, with LGB achieving an AUC-ROC of 0.93, whereas sample-based classification relied more on imaging alone. SHAP analysis enhanced interpretability, highlighting key radiomic features. These results show the potential of radiomics and AI for HCM diagnosis, encouraging further research with larger cohort for more generalizable findings.

3.3.1 Introduction

Hypertrophic cardiomyopathy (HCM) is a primary myocardial disorder characterized by abnormal thickening of the left ventricular myocardium, which can lead to functional impairments and an increased risk of adverse cardiovascular events [224]. HCM is a diagnosis of exclusion; secondary causes of left ventricular hypertrophy (LVH) such as systemic hypertension, valvular and subvalvular aortic stenosis, and infiltrative cardiomyopathies must be ruled out [225]. While conventional imaging techniques, such as echocardiography and cardiac magnetic resonance, remain standard for diagnosis, recent advancements in radiomic analysis have demonstrated potential in extracting quantitative imaging biomarkers from computed tomography (CT) scans [172]. These

biomarkers may enhance disease characterization and improve diagnostic accuracy with the support of artificial intelligence [182].

This work contributes to the growing field of computational imaging in cardiology by exploring radiomic-based predictive modeling for HCM detection and classification. By optimizing machine learning and explainability techniques, we aim to establish a framework for integrating radiomics into clinical workflows, potentially aiding in early diagnosis and personalized risk assessment.

3.3.2 ML Approaches in Cardiac Imaging Diagnostic: state of the art

Advances in computing and data availability have enabled two broad ML approaches in HCM imaging: (1) Radiomics with Classical ML, where handcrafted features (shape, intensity, texture statistics from images) are extracted and input to ML classifiers or regression models (like support vector machines, random forests, or logistic/cox models); and (2) Deep Learning, where convolutional neural networks (CNNs) or related architectures learn directly from imaging pixel data (often requiring large datasets). Both approaches have been applied to morphological images, functional metrics, and tissue-characterization images (LGE, T1 maps), as detailed below.

3.3.2.1 Radiomics for Morphological Differentiation

Radiomics has shown particular promise in differentiating HCM from other causes of hypertrophy by quantifying subtle image textures and patterns. For example, Hu et al. (2022) extracted 275 texture features from CMR cine images and used a least absolute shrinkage and selection operator (LASSO) to select important features for classification of HCM vs. cardiac amyloidosis [226]. In the study of 167 patients (85 amyloidosis, 82 HCM, plus normals), a support vector machine classifier based on 19 selected radiomic features achieved an accuracy of 85% (AUC = 0.89) in the validation set, outperforming models using conventional MRI metrics alone. Notably, a gray-level non-uniformity texture feature was higher in HCM than amyloidosis, reflecting more heterogeneous myocardium in HCM; combining radiomic textures with standard metrics improved diagnostic AUC from 0.79 to 0.89. This suggests radiomics can detect microstructural differences (e.g. myocyte disarray or patchy fibrosis) on non-contrast cine that aid in distinguishing HCM from infiltrative cardiomyopathy, even without LGE.

Another important application is differentiating HCM from hypertensive heart disease (HHD), which both cause left ventricular hypertrophy (LVH). Zhang et al. (2024) built discrimination models using both conventional CMR indices and radiomics from cine and LGE images in a cohort of 421 HCM vs 200 HHD patients [227]. After feature selection, the strongest differentiators were maximal wall thickness, left ventricular ejection fraction, presence/extent of LGE, and composite radiomic scores from cine and LGE images. A combined multivariable model achieved excellent diagnostic performance (AUC = 0.98 in both training and held-out validation sets), significantly better than using only standard CMR measures (which gave 0.79 AUC). The authors concluded that radiomic features from cine and LGE effectively discriminate HHD from HCM, and integrating these with traditional measures could greatly enhance diagnostic accuracy. Such high accuracy (over 98%) indicates that ML can recognize subtle

distinctions (e.g. hypertrophy distribution, scar patterns, texture heterogeneity) that reliably separate primary (HCM) from secondary (hypertensive) hypertrophy.

Similarly, radiomic analysis of native T1 maps has been used to differentiate HCM from phenocopies. A study by Neisius et al. in 2019 showed that texture features of native T1 maps could distinguish HCM from hypertensive heart disease (and healthy controls) with high accuracy, highlighting the value of tissue characteristics even before scar is overt [228]. Radiomics has also been applied to identifying HCM genotypes: e.g. radiomic patterns on T1 mapping were found to differ between HCM due to MYH7 vs MYBPC3 mutations, suggesting ML might even predict genetic subtypes non-invasively.

Beyond radiomics, deep learning has been explored for morphological classification tasks. Chen et al. (2024) developed a deep learning pipeline using 3D convolutional neural networks (3D ResNet) on short-axis cine MRI to distinguish HCM from Fabry cardiomyopathy (another HCM mimic with LVH) [229]. Their model, trained on multi-center data in Taiwan, achieved 91% accuracy (AUC 0.91) on an internal test set and 81% accuracy (AUC 0.92) on an external cohort. Notably, this approach did not require LGE or T1 maps; it relied solely on cine images, recognizing subtle motion and morphological differences between Fabry disease (which often has basal inferolateral hypertrophy with low native T1) and sarcomeric HCM. The deep network effectively became a "virtual expert," matching the accuracy of specialized imaging techniques. Likewise, earlier studies combined deep learning with segmentation: one approach applied a CNN to pre-segmented cine images to classify HCM vs amyloidosis vs Fabry vs hypertensive LVH, demonstrating the feasibility of multi-class differentiation by image appearance. These deep learning models, once validated, could assist general clinicians by flagging likely phenocopies or guiding the need for genetic testing (e.g. identifying features suggestive of Fabry that warrant enzyme assay). However, deep models are often less interpretable; radiomics, in contrast, can sometimes point to human-understandable features (like "Gray-Level Non-uniformity") that drive predictions. A synergy of both approaches is emerging in the field.

3.3.2.2 ML in Tissue Characterization: Fibrosis Detection and Quantification

Identifying myocardial fibrosis is crucial in HCM diagnosis and risk assessment. LGE on MRI is the gold standard for fibrosis, but requires contrast. Machine learning has been leveraged to predict or detect scar using non-contrast data, both in MRI and CT domains. A prime example is the use of balanced steady-state free precession (bSSFP) cine MRI (which all patients get) to screen for scar, potentially reducing unnecessary contrast administration. Fahmy et al. (2022) developed an "AI scar screening" model that combined radiomic features and deep CNN features from cine CMR to predict absence of LGE in HCM [230]. Using 759 HCM patients' cine images, they trained separate models (radiomics alone, CNN alone, and a combined model) to identify patients with no LGE scar. The hybrid DL–radiomics model performed best, with an internal AUC 0.83 and external-test AUC 0.74, significantly outperforming the individual models. In practice, at 95% specificity the combined model correctly identified almost 43% of scar-negative patients (internal test), suggesting nearly half of HCM patients without fibrosis could be recognized without contrast. This could enable a "screening" CMR (cine only) for low-risk patients, reserving gadolinium for those likely to have scar. The authors noted, however, that the model's generalizability and accu-

racy (especially external) were modest, and further refinement is needed before clinical adoption.

In parallel, radiomics applied to LGE images themselves has provided more nuanced quantification of scar beyond simple extent. Textural analysis of LGE can capture heterogeneity of scar (e.g. distribution of gray levels in scar regions), which may relate to arrhythmogenic risk. Fahmy et al. (2024) analyzed LGE-CMR from 1,229 HCM patients across 3 centers, extracting numerous radiomic features of scar, and reduced them via principal component analysis to a few "radiomic indices" [231]. They found that these radiomic features had strong prognostic power: one principal radiomic factor (reflecting scar texture heterogeneity) was a significant predictor of sudden cardiac death (SCD) risk (HR 0.07 per unit change, $P = 0.03$). Moreover, adding the radiomics-based risk score to current guideline risk models improved SCD risk discrimination: for example, combining radiomics with the ESC risk calculator raised the C-statistic from 0.57 to 0.73 (a substantial reclassification improvement). In short, "myocardial LGE radiomics are strongly associated with SCD risk in HCM and provide incremental risk stratification beyond current ESC or AHA/ACC models."[231]. This finding is clinically significant: it suggests that not just the amount of scar, but the texture and spatial complexity of scar tissue, influence arrhythmic risk, patterns that ML can quantify. Such radiomic risk markers are being investigated as additions to decision-making for implantable cardioverter-defibrillators (ICDs) in HCM, although prospective validation is warranted. Machine learning has also extended tissue characterization to cardiac CT, offering an alternative when MRI is unavailable. Contrast-enhanced CT (particularly with delayed imaging, so-called late iodine enhancement, LIE) can depict myocardial scar, though with lower contrast than MRI. Radiomics can potentially amplify CT's diagnostic value. Qin et al. (2021) performed a radiomics study on 161 HCM patients who underwent both coronary CT angiography (CCTA) and CMR LGE [172]. They extracted radiomic features from the myocardium on CT images and built models to predict the presence of significant fibrosis (defined as LGE 15 % of LV mass on MRI). The radiomic signature alone achieved good accuracy for per-segment fibrosis detection (AUC 0.78–0.81 in test). Importantly, a combined model integrating radiomic features with clinical and echocardiographic data reached AUC 0.92 in the test set for identifying patients with substantial fibrosis (15 % LGE). The authors concluded that CT radiomic models are useful, complementary biomarkers for myocardial fibrosis evaluation in HCM, potentially aiding risk stratification when CMR is contraindicated. This is a notable development since CT is far more widely available than CMR; an AI-enhanced CT could one day screen for HCM-related fibrosis (and thus risk) in centers lacking MRI, although issues like radiation and lack of standardized LIE protocols remain. Ongoing research is also exploring dual-energy CT to improve scar visualization, and ML may further optimize scar detection on CT images.

3.3.3 Materials & Methods

3.3.3.1 Population

Forty subjects who underwent CT scans by request of their medical advisor were retrospectively enrolled in this study. The study population was stratified according to the outcome of CT diagnostic test: twenty individuals were negative on CT imaging, used as the control (C), and twenty were diagnosed with HCM, previously described [232].

3.3.3.2 Data collection and Pre-Processing

This examination was based on the extraction of 12 myocardial samples in specific locations of the left ventricle [232]. From each sample, multidomain radiomic feature extraction was performed. A graphical chart of the workflow was reported in Figure 3.15.

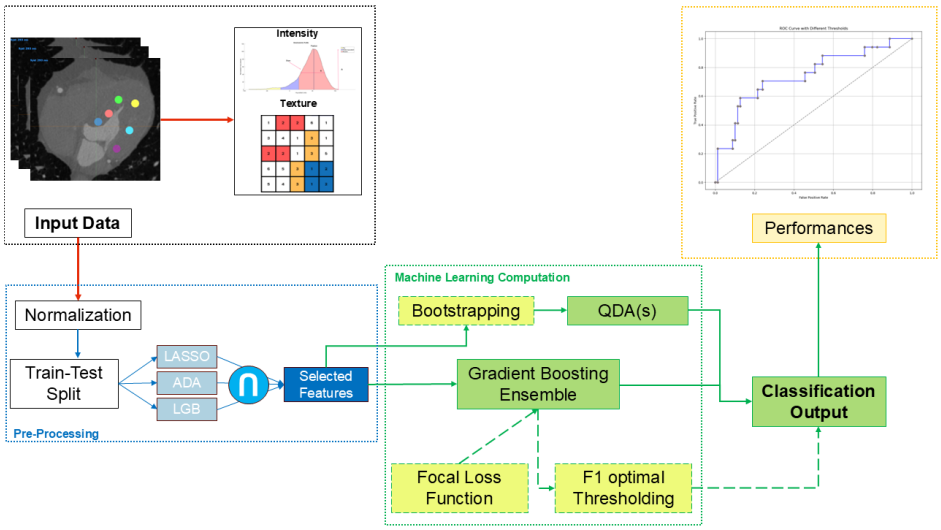

Figure 3.15: Machine Learning pipeline: subject-based prediction has a continuous line (arrows and boxes) and a dashed line contour reported the modification to the pipeline to deal with the unbalance of the sample-based classification task. Blue lines and boxes refer to the feature selection steps.

Original CT image radiomics features were extracted from different families: first-order (pixel brightness) and second-order (texture) were computed with PyRadiomics package (v3.1.0). The texture features quantified the spatial relationship among different combinations of HU such as gray-level co-occurrence matrix (GLCM), gray-level run length matrix (GLRLM), gray-level size zone matrix (GLSZM), neighboring gray-tone difference matrix (NGTDM) and gray-level dependency matrix (GLDM). A total of 75 features were collected so far.
Wavelet transformation with the Haar method was performed on the original images to enable the frequency analysis. A total of eight different configurations of low- and high-pass filtered images were computed. For each configuration radiomics features were re-extracted for a total of almost 100 features per 3D wavelet configuration. A final database of N = 480 samples with M = 795 features was created. Each sample was uniquely identified by the combination of the patient code and its position in the left ventricle. Isotropic resampling at 1 mm was applied to avoid biases in the measured features. The Yao-Johnson transformation was used to compensate for issues related to heteroscedasticity (non-constant variance) for the following ML steps and because it works both for positive and negative feature values. The optimal parameter for stabilizing variance and minimizing skewness was estimated through maximum likelihood. The dataset was split into train and test sets with 80% - 20% distribution of C and HCM subjects in each set to avoid data leakage in the test set. Due to the limited size of the dataset and its retrospective nature, there were biases in subjects' age and sex and in some risk factors. For this reason, only the anthropometric features

(body mass index (BMI) and body surface area (BSA)) that were uncorrelated and not statistically significant among the two populations were included in the set of features. Three different models LASSO, AdaBoost and Gradient Boosting were used to compute feature importance on the training set, and only the features recognized as important by all three models were kept for the actual classification task.

3.3.3.3 Machine Learning models

Two classification tasks were analyzed:

- subject based: the label to the samples was given following the subject condition. 0: Control (240 entries) and 1: HCM (240 entries).

- sample based: the label is assigned to every sample following the sectorial radiological report. 0: Control (370 entries) and 1: HCM (110 entries).

The proposed workflow consisted of two different non-linear methods: Quadratic Discriminator Analysis (QDA) and a tree-based model such as Light Gradient Boosting (LGB) as these were among the most promising models for machine learning purposes and since all the most common linear models were not able to learn from the data. The performances were computed from the test set and estimated by accuracy, sensitivity, specificity, f1-score, and AUC-ROC. To assess the impact of imaging features, a first round of classifiers was trained only on those and later they were retrained on both imaging and anthropometric features.
LGB was created with "gbdt" boosting, 300 estimators, a low learning rate and a high minimum samples per child to control overfitting (0.05 and 20 respectively), and used the 80% of samples and features per single tree. The cost function used was the cross-entropy loss. For the unbalanced classification task, a focal-loss function and an adaptive thresholding method based on the f1-metric were used to convert the raw odds into probabilities.
In addition to performance evaluation, one of the objectives of the proposed work was to guarantee the explainability of the results and of the mechanisms behind the learning strategy of the models. A promising technique, proposed in 2017 and based on Shapley (or shap) values from cooperative game theory was used in this work to explain the predictions of machine learning models [233]. Overall, the technique relied on the assumption that important features have an impact on the classification performances and when these features are missing, the result becomes uncertain. Despite other techniques, embedded into the ML models, shap values are computed on the test set and not at the training phase. Another major benefit is that it provided a direct and optimized computation (explainer) of Shapley values for tree-based algorithms and also an estimation strategy for black-box classifiers such as QDA. We used a TreeExplainer to compute the shap values of LGB models and a KernelExplainer to estimate shap values for QDA and QDAs ensemble. The importance of the latter, particularly, was given as an average of the estimation of each QDA, despite the vote of that single model. A final ranking of features was reported in the beeswarm plot, where the value of a single test set sample and its impact on the model are related.

	Accuracy	Sensitivity	Specificity	F1 score	AUC ROC
Subject-based QDA	**0.66**	**0.71**	**0.63**	**0.68**	**0.67**
Subject-based LGB	**0.61**	**0.60**	**0.63**	**0.61**	**0.61**
Sample-based QDA	**0.77**	**0.71**	**0.78**	**0.52**	**0.77**
Sample-based LGB	**0.75**	**0.65**	**0.77**	**0.49**	**0.74**

Table 3.4: Imaging Features models performances. Subject-based classification performance are reported in the first two rows, whereas sample-based in the last two rows.

	Accuracy	Sensitivity	Specificity	F1 score	AUC ROC
Subject-based QDA	**0.67**	**0.77**	**0.56**	**0.70**	**0.67**
Subject-based LGB	**0.93**	**1.0**	**0.85**	**0.93**	**0.96**
Sample-based QDA	**0.70**	**0.76**	**0.68**	**0.47**	**0.72**
Sample-based LGB	**0.67**	**0.71**	**0.66**	**0.43**	**0.68**

Table 3.5: Imaging Features and anthropometry models performances. Subject-based classification performances are reported in the first two rows, whereas sample-based in the last two rows.

3.3.4 Results

Subject-based classification from a single sample achieved moderate performances with imaging features only (Table 3.4, first two rows). By adding anthropometric features, LGB model showed a boost in performance, reaching 0.93 in accuracy and 0.93 AUC ROC on the balanced dataset (Figure 3.16). QDA, instead, did not increase the performances (Table 3.5, first two rows). To validate the result, a statistical test on the anthropometric parameters was performed and no statistical differences were observed among control and HCM subjects. Features importance with shap values reported anthropometric features as the most relevant followed by wavelet HHL Long Run Emphasis (glrlm) and wavelet LLH HU non-uniformity (glszm). In this classification task, no features from the original image were kept. Sample-based classification reached, on average, better performances particularly with imaging features only: accuracy 0.75 and 0.77 with AUC ROC 0.74 and 0.77 for LGB and QDAs ensemble, respectively (Table 3.4). Anthropometric features, in this case, acted as confounding effects, slightly lowering the performances (Table 3.5). Class imbalance effect was mitigated, and the two ensembles were able to learn from the data, without polarizing towards the majority class. Features importance with shap values reported a combination of original image and wavelet radiomics features as most important. In sample-based classification, the most important feature was the level (basal, medial or apical) of origin of the sample as reported in Figure 3.17.

3.3.5 Discussion

The present study demonstrates the potential of radiomic-based machine learning models in the classification of hypertrophic cardiomyopathy (HCM) using computed tomog-

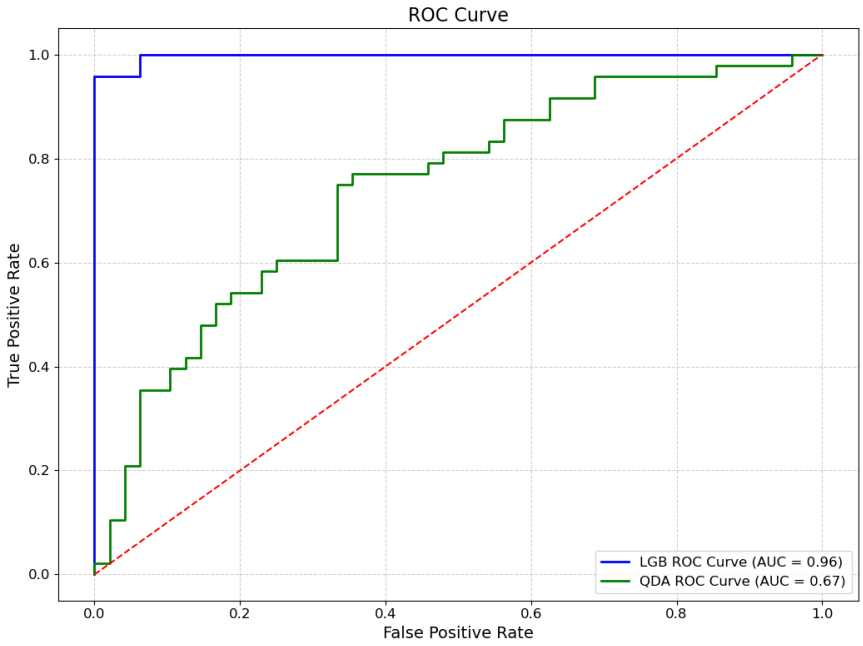

Figure 3.16: Subject-based classification ROCs with imaging and anthropometric features. The red dotted line represents a casual classifier.

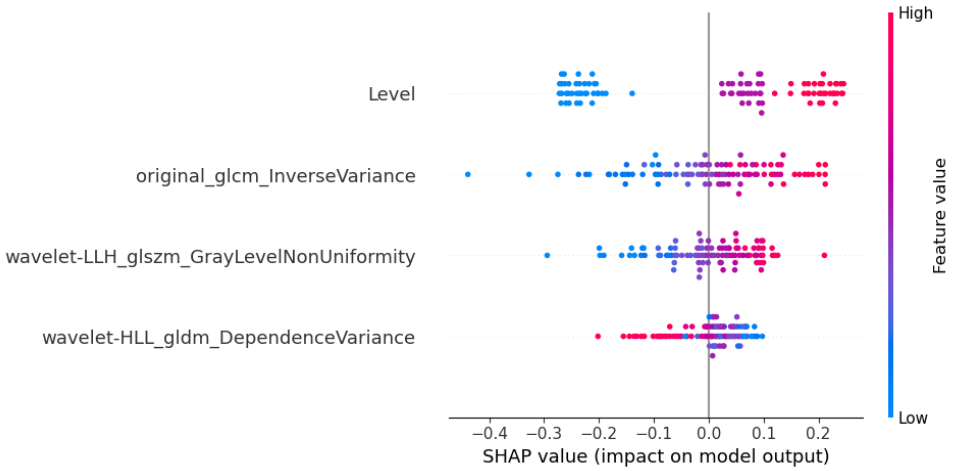

Figure 3.17: Feature importance analysis with imaging-based QDAs ensemble models.

raphy (CT) imaging. Our findings highlight the feasibility of integrating multidomain radiomic features with advanced machine-learning techniques to improve diagnostic accuracy and model interpretability.

Feature selection may be performed with different methods such as filter models, wrapper models, or embedded models. Even though wrapper models maximize the performances by optimizing the objective function, they are generally computationally more expensive due to many reiterations to remove unwanted features. This work proposed a maximum agreement rule over different embedded methods for feature selection.

One key observation is the improvement in classification performance when anthropometric features were included alongside imaging-based radiomic features. Specifically, in subject-based classification, LGB model demonstrated a significant increase in performance, achieving an accuracy of 0.93 and an AUC-ROC of 0.96. The importance of BMI and BSA is confirmed by SHAP, which ranked them first and second, respectively, highlighting how complementary information enhances the discriminatory power of the model. On the other hand, QDA model did not exhibit a similar boost, indicating that its assumptions and decision boundaries may not fully capture the pattern in the data.

Conversely, in the sample-based classification, anthropometric features acted as a confounding factor, slightly reducing classification performance. This may be attributed to the fact that the sample-based labeling was based on local radiological findings rather than global patient characteristics. Consequently, imaging features alone were more effective in capturing localized patterns associated with HCM, as demonstrated by the superior performance of both LGB and the QDAs ensemble in this task.

The impact of class imbalance was effectively mitigated using ensemble strategies and focal loss-based training. The QDAs ensemble and LGB focal loss models outperformed their single-model counterparts, underscoring their applicability in real-world clinical settings, where disease prevalence is often skewed.

Another important contribution of this study is the use of Shapley values for model explainability. SHAP analysis provided insights into the role of specific radiomic features in classification decisions, reinforcing the interpretability of our models. The ability to attribute decision-making to distinct imaging biomarkers enhances clinical trust in AI-driven diagnostic tools and facilitates their integration into routine clinical practice.

Despite these promising results, our study has several limitations. First, the relatively small sample size may impact the generalization of our findings. Larger, multicenter datasets are needed to validate the robustness of our approach.

3.3.6 Conclusion

In conclusion, this study underscores the potential of radiomic-based machine learning models for HCM classification. By leveraging advanced feature selection, ensemble learning, and explainability techniques, our approach provides a robust framework for integrating computational imaging into cardiology. These findings lay the groundwork for future research aimed at enhancing early diagnosis and personalized risk assessment in HCM patients. Future work should explore the integration of deep learning architectures with radiomic-based models to further improve classification performance.

Additionally, prospective validation studies are necessary to assess the clinical utility of our approach in real-world diagnostic workflows.

Chapter 4

Quantitative Morphological Assessment of Meibomian Glands Deficiency

Meibomian Glands Deficiency, Dry Eye Disease and Clinical Assessment

Dry Eye Disease (DED) is a common multifactorial condition of the ocular surface, often associated with unstable tear film and chronic irritation. A large body of evidence indicates that Meibomian Gland Dysfunction (MGD) is a leading cause of DED worldwide [234], [235]. The Meibomian glands, located in the eyelids, secrete the lipid (oil) layer of the tear film which slows evaporation and maintains tear film stability. When these glands are deficient or dysfunctional, the protective lipid layer is compromised, leading to excessive tear evaporation and an unstable tear film [236]. Consequently, MGD-induced lipid insufficiency can precipitate evaporative DED, causing symptoms of dryness, burning, and visual disturbance. Effective evaluation of Meibomian gland health is therefore critical in diagnosing and treating DED, as gland function directly influences ocular surface lubrication and comfort [237].

MGD itself is defined as a chronic, diffuse abnormality of the Meibomian glands, typically characterized by glandular obstruction or qualitative changes in meibum secretion. These changes result in altered tear film composition, increased evaporation, and ocular surface inflammation. In fact, the international MGD Workshop has underscored MGD's impact, noting that it "may well be the leading cause of dry eye disease throughout the world," affecting millions of patients [238]. This underscores the clinical significance of MGD within the spectrum of dry eye etiologies. Identifying and grading the extent of Meibomian gland deficiency (dropout or dysfunction) is pivotal because targeted therapies (such as warm compresses, lid hygiene, gland expression, or lipid-replenishing eye drops) can be instituted to restore tear film stability. However, reliable identification of MGD requires robust clinical assessment methods, which historically have faced challenges in consistency and objectivity.

Clinical Assessment of MGD: Current Methods and Limitations

Clinicians employ a variety of methods to assess Meibomian gland function and diagnose MGD. These include both symptom-based evaluations and objective signs, as outlined below:

- **Symptom and History Evaluation**: Patients often report dryness, irritation, burning, or fluctuating vision. Standardized questionnaires like the Ocular Surface Disease Index (OSDI) capture symptom severity, but these are subjective patient-reported outcomes and may not always correlate with gland findings. Symptom assessment is important for guiding the clinical suspicion of MGD, yet it provides only indirect evidence of gland dysfunction and can be influenced by patient perception and external factors.

- **Tear Film and Ocular Surface Tests**: Clinicians examine tear film stability using tests such as tear break-up time (TBUT) and measure tear production (e.g. Schirmer's test). In MGD, TBUT is often shortened due to inadequate lipid coverage on the tear film. Additionally, signs of ocular surface stress, like corneal staining with fluorescein, may be present. While these tests indicate the functional impact of MGD on the tear film, they are not specific – tear instability can result from other dry eye causes as well. Results can also vary between visits or examiners, and conducting these tests requires time and careful technique.

- **Lid Margin and Gland Orifice Examination**: Under slit-lamp biomicroscopy, the clinician inspects the eyelid margins for signs of MGD such as plugged gland orifices, lid margin telangiectasia, or anterior blepharitis. Gentle pressure on the lid (Meibomian gland expression) is applied to observe the quality and quantity of meibum expressed. Gland secretions may be graded (e.g. clear vs. turbid or toothpaste-like secretions) and the number of functional glands can be estimated. This examination provides direct information about gland functionality. However, it is largely qualitative, the interpretation of meibum quality or the force used to express glands can vary between examiners [239]. As a result, manual gland expression and grading are subjective and can differ widely between practitioners, contributing to interobserver variability in MGD diagnosis. Moreover, the process can be time-consuming and uncomfortable for the patient, since it involves physical manipulation of the lids.

- **Meibography (Meibomian Gland Imaging)**: Meibography has emerged as an indispensable tool for directly visualizing the structure of the Meibomian glands in vivo. Infrared meibography, in particular, uses infrared light to illuminate and capture high-contrast images of the glands through the tarsal eyelid tissue. This technique reveals morphologic details such as gland dropout (areas where glands are atrophied or missing), shortening or truncation of glands, gland blockage, and tortuosity (twisted or irregularly shaped glands). By providing an anatomical map of gland health, meibography allows clinicians to classify MGD severity based on the extent of gland loss or distortion (e.g., using meiboscore grading scales). It also aids in differentiating MGD from other ocular surface diseases that might cause similar symptoms. Crucially, meibography is objective and highly reproducible in the sense that it produces a visual record of the

glands that can be reviewed and compared over time [239]. In modern dry eye clinics, it has become one of the most widely used imaging techniques for MGD assessment.

Despite the value of these methods, each comes with significant limitations. Symptom questionnaires are inherently subjective and can fluctuate, tear film tests have variability and lack specificity, and slit-lamp gland evaluations depend on clinician experience and technique. Even meibography, while instrumental, has traditionally required manual interpretation of the gland images. Clinicians or graders must often outline glands or estimate the area of gland loss by eye, or assign an empirical grade based on appearance. This manual image analysis is time-consuming and subjective, and it suffers from high interobserver variability. Studies have shown that different observers (or the same observer at different times) may disagree on the degree of gland dropout visible in an image, due to subtle distinctions and lack of standardized quantification. In essence, most conventional approaches for evaluating Meibomian glands have been qualitative – relying on human judgment to interpret gland appearance or expressibility. As a result, there is considerable potential for inconsistent diagnoses or tracking of MGD, especially in mild or borderline cases. Furthermore, manual grading of images adds to clinical workload, making it impractical to perform detailed gland analysis for every dry eye patient in a busy practice. These shortcomings in current clinical assessment underscore the need for more objective and efficient diagnostic modalities in MGD.

Meibography in Modern Diagnostics and the Need for Automation

In contemporary DED management, instrumental diagnostics have become increasingly important to complement clinical examination. Meibography, in particular, provides an objective visualization of gland morphology that is invaluable for both diagnosis and ongoing monitoring of MGD. Because it directly images the glands, meibography can document the progression of gland loss or the improvements following treatment, which can be tracked by comparing images over time [240]. This longitudinal tracking is critical in a chronic condition like MGD, where therapeutic interventions (e.g. warm compresses, gland expression, thermal pulsation treatments) aim to halt or reverse gland dropout. By staging the disease (mild, moderate, severe gland loss) and observing changes, clinicians can adjust treatment plans in a timely manner. Indeed, the benefits of Meibography include monitoring and staging of disease progression, as well as evaluating treatment effects in a quantifiable way [240]. Modern ocular surface disease clinics often incorporate Meibography alongside other tests, making it a cornerstone of DED workups. However, the full potential of Meibography is realized only when its interpretation is objective and quantitative. Recognizing the limitations of purely human evaluation, recent efforts have turned toward computer-assisted analysis of Meibography images. Semi-automated and automated image analysis techniques have been developed to improve consistency. More advanced approaches employ machine learning, particularly deep learning convolutional neural networks (CNNs), to automatically identify gland structures and even detect MGD with high accuracy [241]. These data-driven models, trained on annotated Meibography datasets, have demonstrated impressive ability to match expert evaluations of gland loss. Automated segmentation and analysis reduce reliance on subjective grad-

ing, offering the promise of more standardized assessments across clinics. Despite their promise, current high-end solutions like deep learning come with practical challenges. Training robust CNN models requires large labeled image datasets, and the computational demand for running such models can be high. In a busy clinic setting, the delays from processing time or the need for powerful hardware can limit the feasibility of deploying these techniques for real-time patient feedback. Studies have noted that while deep learning methods can accurately segment glands and quantify dropout, they often involve lengthy processing pipelines (including image pre-processing and post-processing) and may not integrate easily into commercial ophthalmic devices or provide instantaneous results during a patient visit. These factors have spurred interest in simpler, faster analytical methods that still provide objective results. Objective, live, and quantitative assessment of Meibomian glands is now recognized as an essential goal for improving DED diagnostics and management. An ideal solution would deliver immediate, reproducible measurements of gland morphology during the exam, without the need for extensive manual input or waiting time. To this end, the research presented in "Advancing Meibography Assessment and Automated Meibomian Gland Detection Using Gray Value Profiles" introduces a novel automated approach leveraging gray-value distribution profiles in meibography images [242].

The core idea is to use the pixel intensity patterns (gray values) within infrared Meibography images to distinguish glandular tissue from the background and to quantitatively characterize each gland's structure. Since Meibomian glands and surrounding tissues reflect or absorb infrared light differently, their gray-scale intensity profiles can serve as digital signatures. By analyzing these intensity profiles along the eyelid, the algorithm can automatically detect glands as continuous peaks or regions of distinctive pixel brightness. This yields measurements such as gland length, width, and an "atrophy index" that quantifies gland loss or degeneration across the entire lid image. Importantly, this gray-value profile method is computationally lightweight compared to deep learning approaches, enabling real-time analysis during the clinical exam. The automated output is a set of objective metrics describing the gland morphology, which can be tracked over time or used to stratify disease severity in a quantitative manner.

4.1 Advancing Meibography Assessment and Automated Meibomian Glands Detection Using Grey Values Profiles

Abstract

Objective: This study introduces a novel method for the automated detection and quantification of Meibomian gland morphology using gray value distribution profiles. The approach addresses limitations in traditional manual and deep learning-based meibography analysis, which are often time-consuming and prone to variability.

Methods: This study enrolled 100 volunteers (mean age 40 ± 16 years, range 18–85) who suffered from dry eye and responded to the Ocular Surface Disease Index questionnaire for scoring ocular discomfort symptoms and infrared meibography for capturing imaging of Meibomian glands. By leveraging pixel brightness variations, the algorithm provides real-time detection and classification of long, medium, and short Meibomian glands, offering a quantitative assessment of gland

atrophy.
Results: A novel parameter, namely "atrophy index", a quantitative measure of gland degeneration, is introduced. Atrophy index is the first instrumental measurement to assess single- and multiple-gland morphology.
Conclusions: This tool provides a robust, scalable metric for integrating quantitative meibography into clinical practice, making it suitable for real-time screening and advancing the management of dry eyes owing to Meibomian gland dysfunction.

4.1.1 Introduction

Dry eye disease (DED) is a complex and multifactorial condition that is frequently driven by Meibomian gland dysfunction (MGD), which causes instability of the tear film. The Meibomian glands play a critical role by secreting the lipid layer of the tear film, preventing excessive evaporation, and maintaining a healthy and lubricated ocular surface [243], [244]. Accurate assessments of these glands are pivotal for the effective diagnosis and treatment of MGD, and infrared meibography has emerged as one of the most widely used imaging techniques for this examination.

Meibography is a non-invasive imaging technique that visualizes the structure of the Meibomian glands using infrared light. This allows clinicians to detect abnormalities such as: gland shortening, dropout, blockage, and tortuosity by capturing detailed images of the glands inside both eyelids [245]. However, traditional meibography analysis is often performed manually, leading to time-consuming, subjective interpretations that suffer from high interobserver variability [246]. Addressing these limitations through automation is essential for improving diagnostic accuracy and consistency.

To overcome the challenges of manual meibography evaluation, semi-automated and automated techniques have been developed. These methods often employ image segmentation and feature extraction algorithms to differentiate Meibomian glands from surrounding tissues [247]. More advanced solutions involve machine learning, particularly deep learning models like convolutional neural networks (CNNs), which have demonstrated high accuracy in detecting gland abnormalities [248]. While deep learning techniques have achieved impressive accuracy in detecting Meibomian glands, significant practical limitations remain, such as the extended computational time required for both training and inference, which hinders real-time application. For instance, CNNs, though effective for segmenting glands and detecting gland dropout, require substantial computational resources, making them unsuitable for use in fast-paced clinical settings where immediate feedback is critical [249]. These delays are exacerbated by the need for pre- and post-processing steps, further complicating their integration into clinical workflows.

To address these limitations, this study proposes a novel method for the quantitative evaluation of meibography images that reduces computational time while maintaining high accuracy. Our approach leverages gray value distribution profiles to detect and characterize Meibomian glands automatically, providing a feasible solution for real-time analysis and integration into clinical workflows.

Pixel brightness, or gray value, reflects a tissue's response to light and varies based on the imaging technology used, such as X-ray absorption in computed tomography scans or magnetic properties in magnetic resonance imaging [250], [251]. Recent advances in radiomics, which examine pixel intensity and spatial relationships, have shifted focus from broad imaging to key regions of inter-

est, enabling more precise, evidence-based analyses of pathological tissues [252], [253]. For instance, radiodensity measures in skeletal muscle have been linked to predicting sarcopenic degeneration and cardiovascular diseases [254]–[256]. In meibography, infrared imaging captures the thermal responses of Meibomian glands, requiring precise differentiation between glands and the surrounding tarsus. However, due to tissue overlap and light exposure, this distinction can be challenging. To overcome this limitation, a local approach is proposed. To recognize glands, the alternation between brighter spots (actual glands) and darker one (tarsus, background) is exploited: following a curved line from the left to the right side of the eyelid, a gray value swing may be observed, where the peaks match with glands and the valleys match with the background.

The purpose of this study is to develop an automated instrumental measurement for detecting and quantifying single- and multiple-Meibomian-gland morphology in the lower eyelid.

4.1.2 Materials and Methods

4.1.2.1 Study Setup and Data Acquisition

The study enrolled 100 volunteers (mean age 40 ± 16 years, range 18–85, 53% female) without a definitive diagnosis of DED but reporting a variable degree of ocular discomfort symptoms. Exclusion criteria were related to a history of epilepsy, and metal implants in the facial area. Subjects were visited at 3 time points (day 0, day 14, and day 28) for the evaluation of (i) the Ocular Surface Disease Index (OSDI) questionnaire for the assessment of ocular discomfort symptoms [257] and (ii) infrared images of the Meibomian glands (Me-check®, Espansione Group, Bologna, Italy).

The cohort was split into 10-year age groups, and a description is reported in Table 4.1.

Table 4.1: Demographic and clinical characteristics of the study population by age group. The table reports average age (years old), gender distribution (female/male), and baseline Ocular Surface Disease Index (OSDI 1) scores for each age group.

	20–30 (Years)	**30–40 (Years)**	**40–50 (Years)**	**50–60 (Years)**	**>60 (Years)**
Age (mean)	27.0	35.8	43.6	53.3	67.7
Gender (F/M)	24/16	6/5	2/5	9/6	5/7
OSDI 1 (score)	18.5	26.6	20.4	22.4	27.0

After the baseline evaluation, patients were treated once with Low-Level Light Therapy (LLLT) technology using the My-mask® device (Espansione Group, Bologna, Italy) for 15 min with their eyes closed [258]. An infrared picture of Meibomian glands was taken again after the LLLT session.

The OSDI score was categorized in 4 classes, as follows: normal (0–12), mild (13–22), moderate (23–32), and severe (33–100) dry eye [259]. The meibography of the lower eyelid was taken in a dark environment to minimize the effect of external light and reflection on image quality. The Supplementary Materials

(S1) report the analysis of the LLLT effect on ocular discomfort symptoms and Meibomian glands.

4.1.2.2 Meibomian Gland Profiling

The proposed approach relies on the brightness gradient obtained while crossing the Meibomian glands from one side to the other at different heights, knowing that a pathological eyelid may show shortening in some glands. Figure 4.1a reports an example of how the signal shape is when extracted from a healthy and pathological region of an everted eyelid. After a moving average filter with a window size equal to 200 steps, a chart of gray values over the x position was drawn, and it represented the alternation of glands and tarsus below the segments as the gradient of the gray value (Figure 4.1b). The number of glands detected by the segments was estimated by the number of peaks found on the signals. Since the number of peaks varied over the lines, to calculate the actual number of glands and their length, Dijkstra's algorithm was introduced. Dijkstra's algorithm is a weighted-graph algorithm that finds the shortest path from a given node source to every other node [260]. In a weighted graph, the shortest path is the collection of edges with the minimum total weighted sum; in our case, the graph is built in a way that every path represents a gland. The eyelid was isolated with a pre-constructed binary mask that replicated the Me-check® built-in alignment, and 4 lines were used to extract gray values at different heights (Figure 4.1c). Each line was mapped into a layer of the graph, and each peak was mapped into a node. Nodes from the adjacent layer were fully connected with arcs weighted by the distances between the two nodes. To reconstruct the elongated shape of a gland, the minimum path was found (Figure 4.1d). First, all the layers were used to find the full-length glands. In the subsequent iteration, the upper layer was removed as well as nodes already associated with a gland, and the logic was reapplied to detect shortened glands. Each gland was then labeled as long (L), medium (M), or short (S) based on the number of layers involved, and therefore, the length became discretized. A counting step was introduced for each group as the sum of the number of glands belonging to that discretized length (N_L, N_M, and N_S).

The width of the peak provided an estimation of the width of the glands at 50% of the peak height. In addition, the average width of glands per class x (L, M, or S) was computed as follows:

$$AveWidth_x = \frac{\sum_1^n Width_{x,i}}{N_x}$$

where i from 1 to n means that the sum was performed on all the glands of that group.

4.1.2.3 Profiling Automation

An algorithm was designed to automate the profile extraction. It is based on the profile extraction previously described, and it receives input from the meibography and a mask that represents the eyelid shape; both images have a resolution of 1280 × 720 pixels. The first step is to obtain the "profile lines", the lines underneath which the gray value is extracted. To achieve this, the mask is divided into 5 different vertical zones, and the size of the foreground is divided into percentages (0.10, 0.45, 0.55, and 0.75) downwards. Each point is connected to

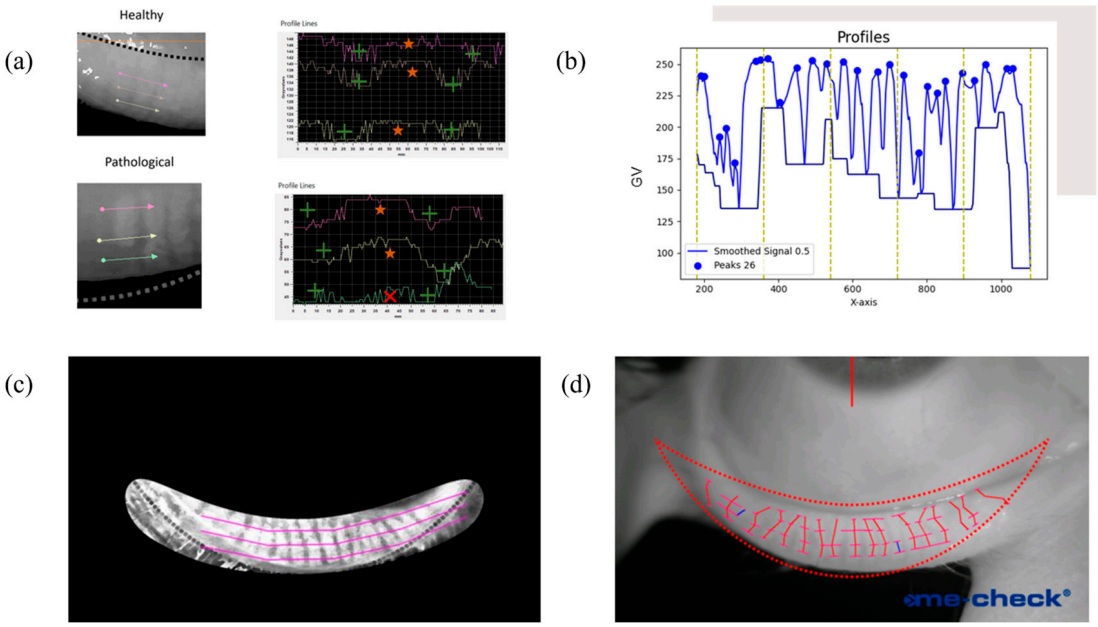

Figure 4.1: Major steps for gland detection: (**a**) local image of how gray value gradient can be associated with the presence of a gland (star) or a missing gland in a pathological condition (X) and the background (+); (**b**) the gray value profile extracted from a single line, filtered and with the peaks recognized; (**c**) how the sampling was carried out to determine the presence and size of Meibomian glands; (**d**) the result, highlighting the skeleton of the glands and the width in corresponding nodes.

one of the subsequent zones and at the same height. In this way, we obtained piecewise continuous lines that accommodated the eyelid shape (Figure 4.2).

The input image undergoes a filtering process to enhance the contrast. First, the dark images are corrected by moving the histogram in a way that it is centered around the value 100 (considering the gray value in a range from 0 to 255). Then, several filters are applied to enhance the contrast between the glands and the foreground. The first filter is a Canny with an aperture size of 3, a lower threshold of 0, and a higher threshold of 255, the two extremes. It was found that this enhances the light reflex on the eyelid, so the effect can be mitigated by extracting the burned pixels (white) of the obtained images and substituting those pixels with a value in the original image. The value is evaluated since the reflection is related to a localized and more humid zone of the eyelid. Therefore, these areas can be considered as connected components, filling the inside with a mean value evaluated from the contour pixels. Next, the dark pixels are transformed to pure black with a threshold of 50, as the intensity is enhanced in terms of the contrast between light pixels and darker ones. The image histogram is then equalized through the contrast-limited adaptive histogram equalization (CLAHE) technique with a clip limit of 12 and a 20×20 grid, and the goal is to remove the illumination gradient that can affect the algorithm's performance. Then, a gray value closing morphological transformation is applied to remove small dark holes in the bright foreground of glands. The structuring element is a circle with a diameter of 5 pixels. Finally, the histogram is equalized to stretch the values among the full range of representation and separate the background from the foreground.

From the filtered image, the gray values are extracted from the profiles, the curves are smoothed with a linear Savitzky - Golay filter with a window length

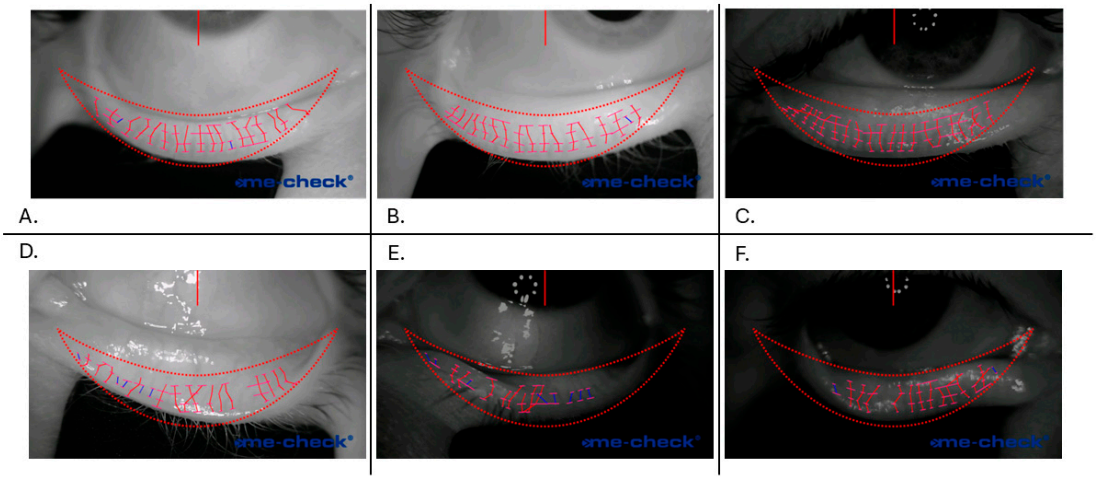

Figure 4.2: The algorithm's output for different types of images. The first row (**A**–**C**) reported well-segmented glands, in two opposite illumination conditions. The second row (**D**–**F**) reported the more common mistakes where glands were misrecognized due to reflection artifacts (**E**,**F**) or incorrect eyelid eversion (**D**,**F**).

of 11, and the peaks with prominence of 0.1 and a minimum width of 2 are considered valid.

To reduce the number of double detections in the same gland, peaks closer than 10 pixels cannot be a gland, so they are fused into a new peak localized in the middle with a width that is the sum of the two older ones. Sometimes, peaks that do not represent a gland can be recognized because of their high width, so we removed them with a threshold of 90 pixels.

The algorithm's core is a graph that allows the peaks from different profiles to be connected to trace the glands. Each peak can be represented as a node, and a group of them is a layer; the nodes contained in a layer come from the same profile and are not connected at all. Since the profiles are ordered, the layers are also "ordered" in the sense that each node of the first profile (the upper or the lower, depending on how you build the graph) is connected to every node of the second profile and only to those nodes with direct edges. The nodes in the second layer are connected to the nodes in the third one, and so on. It is worth noticing that each node in the second layer has inward edges from every first layer's node. The edges are weighted with the Euclidean distance between the two nodes that they connect. Two special nodes are added to this graph, and they are the "supersource" and the "supersink"; the first one is connected to every node of the first layer with an edge weight of 0, and the second one is connected to every node of the third layer with an edge weight of 0.

The two special nodes serve as the Dijkstra algorithm's starting and ending points, searching for the shortest path from the source to the sink. Considering the meaning of the edges' weights, the shortest path is the connection between nodes of different layers that are generally "closer": the gland and its length is the sum of the edges' weights, which is the path length itself. The selected nodes are removed from the graph, and the algorithm is repeated until the length of the gland is higher than a threshold fixed at 100. At this point, because the glands can shorten, the layer containing the peaks from the upper profile is removed, and either the supersink or the supersource is left without a connection. They are connected again to the new upper layer available, and the algorithm is repeated until there are at least 3 layers in the graph. In this situation, the third layer is

removed, and the edges shorter than a threshold fixed to 60 pixels are considered a gland. The glands composed of only two nodes are the shortest detectable by the algorithm, but this distance can be fixed by tuning the number of profiles.

In this way, we automatically obtain the number of glands, their length, and a variable number of widths linked to every gland.

4.1.2.4 Atrophy Index

To encapsulate the extracted information in one quantitative value, we proposed an index defined as follows:

$$Atrophy\ Index = \frac{N_L - (N_M + N_S)}{N_T}$$

where N_L is the total number of long glands from that image, N_M is the number of medium length, and NS is the number of short glands. N_T is the sum of N_L, N_M, and N_S. The atrophy index spans from -1 to 1, where the minimum is associated with a subject having all the glands shortened, and the maximum is a subject where all the glands are healthy and cover the entire eyelid in length.

4.1.2.5 Statistical Analysis

The atrophy index and AveWidth parameters were computed for each eye for each subject. A Pearson correlation analysis was performed with OSDI scores to search for possible relations between self-reported statuses and objective measurements. In addition, a Kruskal–Wallis test, due to the non-normality of the data, was performed on the counted number of glands (NL, NM, and NS) over the OSDI score to verify if the number of glands was significant for the pathology.

Due to a lack of gold standards and instrumental assessment for meibography, the glands extracted by our algorithm underwent a validation process through visual inspection performed by a team of experts, including optometrists, doctors, and engineers.

4.1.3 Results

4.1.3.1 Algorithm Performance and Robustness

The number of glands is a patient-specific parameter. An example of algorithm output can be found in Figure 4.2, as well as in the Supplementary Materials (S2). Figure 4.2A–C show the algorithm's ability to recognize glands in different bright environments, and the algorithm was able to identify most of the glands and their width. However, despite the algorithm having a built-in correction strategy to compensate for reflection spots, when this artifact was too heavy, the computation failed by missing glands and/or their length (Figure 4.2D,F). In addition, the output strongly depends on the quality of the eyelid eversion, such as prolapsed conjunctiva (Figure 4.2D) and incomplete eversion (Figure 4.2E,F), leading to missing glands and/or due to practitioner eversion expertise.

The same number of glands among the appointments should be counted to validate the algorithm; indeed, in Figure 4.3, the number of mean glands recognized in each visit shows almost no variation within the same gland group.

This number is extracted by keeping the same algorithm parameters in the analysis of each image because this number is highly dependent on them. Indeed, the number of profiles and their location, with respect to the eyelid and gland positioning, is a crucial factor in correctly recognizing the glands.

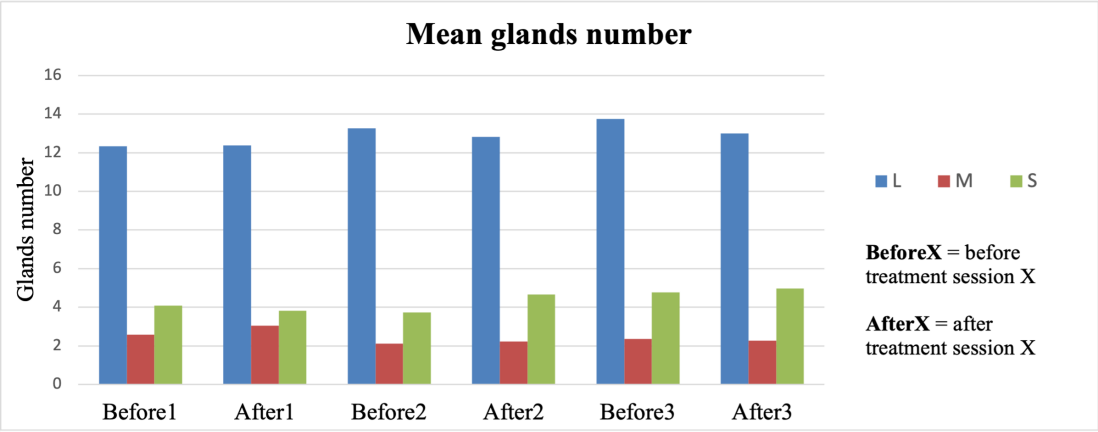

Figure 4.3: Mean number of Meibomian glands in the lower eyelid during the different time points over the entire population.

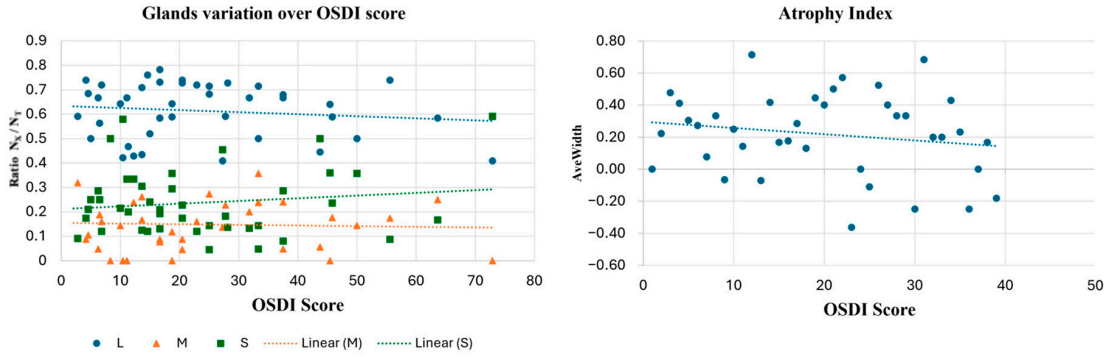

(A) (B)

Figure 4.4: (**A**) The ratio of the number of long/medium/short glands over the total number per subject and their trends; (**B**) the atrophy index correlation with OSDI score.

4.1.3.2 Atrophy Index and OSDI Score

The outliers were handled by using only good-quality images and manually inspecting the algorithm's output. However, extreme values outside the 5th and 95th percentiles were excluded from the subsequent analysis.

The number of glands from each grade of severity of the disease was reported as not statistically different (Kruskal–Wallis p-value > 0.05 for N_L, N_M, and N_S over the grades normal, mild, moderate, and severe).

A correlation analysis of the normalized number of glands in each class on the OSDI score reported Pearson coefficients of -0.13, -0.04, and 0.14, respectively, for long, medium, and short glands (Figure 4.4A). When combined into the atrophy index, the correlation analysis on the OSDI obtained from the measured cohort reported a Pearson coefficient of -0.28 (p-value $= 0.07$), and the correlation can be seen in Figure 4.4B.

AveWidth showed no correlation with OSDI score when extracted from long glands (Figure 4.5A) but showed a progressive decrease for the medium gland (Figure 4.5B) and an increase for short glands (Figure 4.5C).

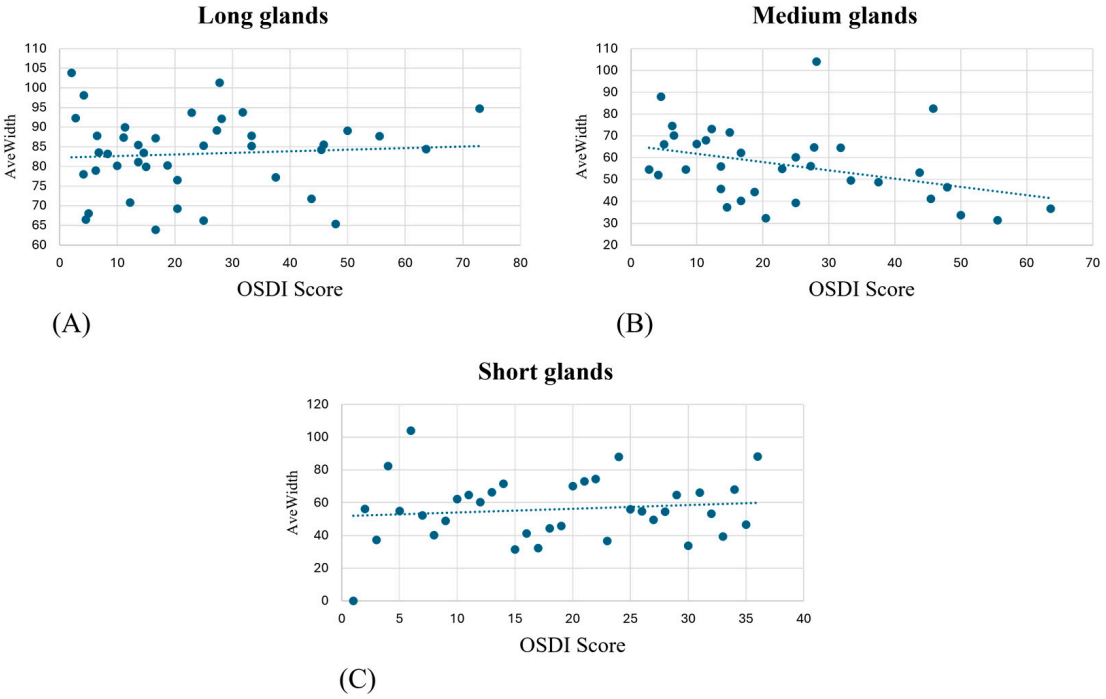

Figure 4.5: AveWidth variation in OSDI score at first visit for detected long (**A**), medium (**B**), and short (**C**) Meibomian glands.

4.1.4 Discussion

This study describes a novel method for the analysis of meibography based on quantitative descriptors from the gray value distribution and develops the atrophy index that, to the best of our knowledge, represents the first instrument for the evaluation of Meibomian gland morphology. The proposed methodology, based on gray value profiles, successfully identified and quantified glands, offering an objective and automated approach compared to traditional methods that rely on visual evaluation. This innovation addresses a crucial need in the field, where quantitative assessment tools are limited, and most of the current analysis remains qualitative and subjective.

Our algorithm successfully differentiated between gland morphology by detecting distinct gray value peaks corresponding to Meibomian glands. This segmentation approach enabled a more detailed evaluation that is particularly valuable in assessing the severity of gland shortening/loss or atrophy, which could be associated with several clinical conditions.

The analysis conducted between the gland's widths/atrophy index and OSDI score failed to find a correlation. This result may be explained by the subjective nature of the OSDI questionnaire and its short-term variability, even after a single LLLT session. Conversely, as reported in Figure 4.2, the atrophy index does not change over 2 months of follow-up, independently of the efficacy of the LLLT, requiring longer time intervals for frank longitudinal changes.

Recent studies in deep learning-based segmentation, such as the Mask R-CNN and U-Net architectures, have shown excellent performance in gland segmentation and dropout detection. These models utilize large, annotated datasets to train their algorithms and can rapidly segment Meibomian glands [261], [262]. However, one of the key limitations of these approaches is the substantial computational power and time required for both training and inference, which delays

results and reduces their applicability in fast-paced clinical environments [249]. Additionally, these models often require significant pre- and post-processing steps to refine gland segmentation, further complicating their integration into commercial devices for everyday clinical practice [263], [264].

In contrast, our proposed gray value distribution-based method reduces the computational complexity, providing a robust evaluation of single- and multiple-gland morphology. This allows for real-time analysis, providing immediate feedback to clinicians, which is critical for timely decision making at diagnosis and throughout therapy during patient evaluations. Moreover, our approach does not require large training datasets, making it more accessible for clinical settings where data collection and annotation are challenging.

The key innovation of our algorithm is its ability to quantify morphological metrics such as gland length, width, and atrophy index, which are crucial for objectively tracking the progression of MGD. Our method allows a direct calculation of gland morphology from the gray value profiles.

In terms of clinical impact, the real-time capabilities of our method provide significant advantages. Unlike deep learning models, which require dedicated hardware and extensive computational resources [260], our algorithm can be implemented on standard clinical equipment without sacrificing performance. This facilitates its integration into existing clinical workflows and commercial meibography devices, ultimately improving patient care by delivering rapid and reliable results. Additionally, the automated nature of our method eliminates the subjectivity and potential for human error inherent in manual meibography analysis, increasing diagnostic accuracy and reproducibility across different clinical environments. This approach has the potential to substantially improve the diagnosis and management of MGD, making advanced meibography analysis more accessible and practical for a broad spectrum of eye care professionals.

The limitations of the proposed study concern the high variability and complexity of meibography since it might be difficult to assess the exact point where the eyelid ends. Thus, an expert operator is still essential. For these reasons, future work may include more subjects and an ad hoc binary mask to better isolate the everted eyelid.

The present work advances state-of-the-art techniques for the imaging of Meibomian glands, and the main benefits and novelties are (i) a pixel-based automatic algorithm for the identification and localization of Meibomian glands and (ii) a multiscale morphological parameter extraction methodology where information can be retrieved from a single gland up to the entire eye lid gland population.

4.1.5 Conclusions

In conclusion, this study introduces a novel, automated approach for the detection and quantification of Meibomian glands using gray value distribution profiles. The algorithm developed demonstrates high performance in terms of computational efficiency and gland recognition ability, making it suitable for real-time clinical use in diagnosing and managing MGD. By providing a quantitative, objective method to assess gland morphology, this approach offers significant advantages over traditional manual and deep learning techniques, particularly in fast-paced clinical environments. This innovation represents a step forward in the integration of meibography into everyday ophthalmic practice.

The algorithm described in this study is currently patent pending, further underscoring its unique contribution to the field. As we continue to refine this

technology, future research should explore its broader applications and potential to enhance patient care.

Chapter 5

Medical Education & Surgical Training

Digital imaging data, particularly when acquired in three dimensions, serve as the foundation for building anatomically accurate virtual models, which can be employed in surgical education, rehearsal, and planning. The ability to segment and reconstruct patient-specific anatomies from CT or MRI scans has paved the way for the development of simulation environments that mimic real surgical scenarios. These platforms may include virtual reality (VR), augmented reality (AR), or mixed reality (MR) interfaces, and sometimes incorporate haptic feedback to simulate tactile sensations.

Surgical simulation based on medical imaging provides a risk-free environment where trainees can practice procedures, improve their anatomical knowledge, and gain familiarity with rare or complex cases. In neurosurgery, for instance, MRI-based models of the brain and spinal cord allow for precise visualization of tumor boundaries and eloquent areas, supporting safe resection planning. In orthopedics, 3D models of fractured bones assist in planning fixation strategies and implant placement. Similarly, in cardiovascular surgery, reconstructed models of the aortic arch, coronary arteries, or congenital heart defects are used to prepare for complex interventions.

An emerging trend is the use of 3D printed models derived from imaging data. These tangible representations are used not only for surgical planning but also for patient education and interdisciplinary communication. In complex craniofacial surgeries, for example, customized implants can be designed preoperatively based on 3D reconstructions. In minimally invasive procedures, preoperative rehearsal on virtual or printed models has been shown to reduce operative time and improve outcomes [265], [266].

Advanced image-guided navigation systems now allow for the real-time use of preoperative imaging during surgery. In these contexts, accurate segmentation and registration of anatomical structures are crucial. When integrated with tracking systems, imaging data can support intraoperative guidance, enhancing precision and safety [64].

From a pedagogical perspective, digital imaging has become a cornerstone in medical education. Anatomical atlases and dissection labs are increasingly supplemented or replaced by digital platforms offering interactive, high-resolution 3D models. These tools foster a more intuitive understanding of spatial relationships and allow for repeated, self-paced exploration. In this regard, digital imaging is not just a diagnostic tool but a medium for learning and collaboration.

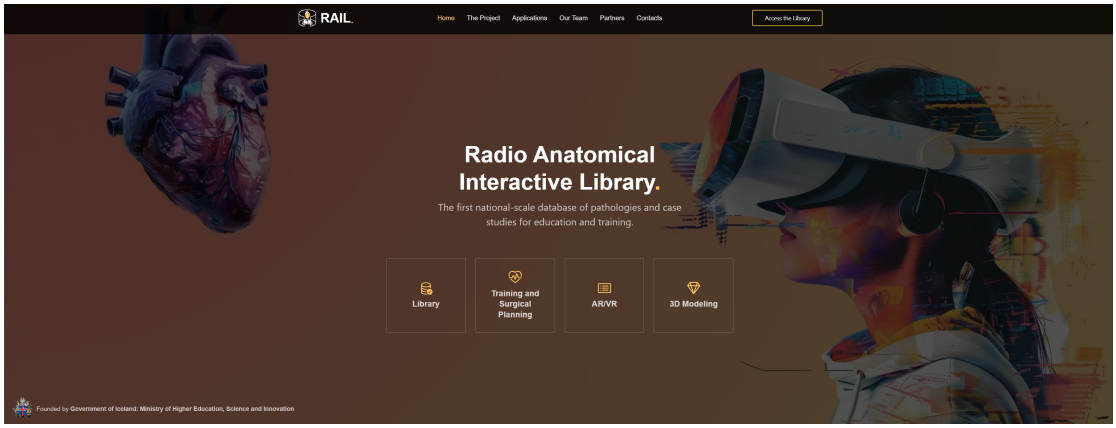

Figure 5.1: RAIL web-site landing page.

5.1 RAIL

The Radio Anatomical Interactive Library (RAIL) is a national-scale platform developed in Iceland as part of a collaborating initiative to combine together advanced planning and technological visualization building a always available repository where professionals may study previous cases and students can learn about a desired procedures. Rather than inventing new hardware or techniques, RAIL innovates by integrating existing technologies, including medical imaging, 3D modeling, 3D printing, and augmented reality (AR)/virtual reality (VR), into a cohesive system (Figure 5.1). The platform's purpose is to make surgical anatomy and pathology more accessible and interactive for learners and clinicians, addressing several longstanding challenges in surgical training. Traditional surgical education relies heavily on cadavers, plastic models, or observing live surgeries, which can be expensive, ethically complex, and limited in availability. By contrast, digital simulations and models offer a safer, repeatable, and more widely accessible alternative [267]. RAIL's relevance is underscored by the growing evidence that extended reality (XR, an umbrella term for VR/AR) can significantly improve surgical skills acquisition and anatomical understanding [268]. XR-based training environments have been shown to increase procedural accuracy and reduce errors, while also enabling practice without risk to real patients [267]. In this context, RAIL serves as a comprehensive educational platform that leverages real patient imaging data to create interactive 3D anatomical models, which can be explored in AR/VR or as physical 3D prints. Crucially, this integration reduces the cost and barriers to simulation-based learning: RAIL emphasizes in-house production of real cases 3D models to make advanced training "more accessible and affordable" on a national scale. As the first national-scale database of pathological cases and 3D anatomical models for education and training, RAIL represents a novel infrastructure for surgical education, linking hospitals and universities in a shared digital library of anatomy.
This chapter provides a detailed overview of the RAIL project as an innovation in surgical training, describing its integrated approach, system architecture, example use-cases, and its impact and future directions.

5.2 System Architecture

The RAIL platform's architecture can be understood as a workflow pipeline coupled with a distribution network connecting the hospital and universities. The major components of this system are outlined below and are represented in Figure 5.2, following the journey of a case from data acquisition to end-user experience:

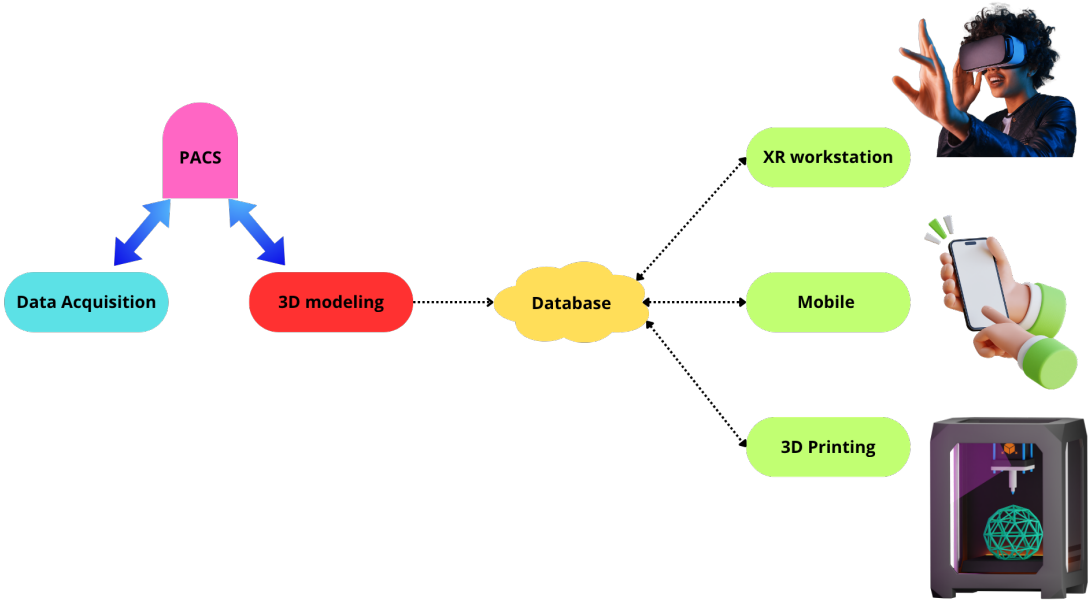

Figure 5.2: RAIL infrastructural design: from acquisition and integration into Landspitali PACS, to 3D modeling creation, upload into the online database through a proprietary server and final model navitaion options.

Data Acquisition (PACS Integration): RAIL begins with real patient imaging data sourced from the national PACS (Picture Archiving and Communication System) at Landspítali University Hospital. PACS is the standard digital repository for radiological scans (CT, MRI, etc.) in the healthcare system. When a new case is identified for inclusion (for instance, a unique pathology or an anatomy of educational interest), the relevant DICOM imaging data is retrieved from the PACS. This integration means RAIL has access to a wealth of authentic clinical data, ensuring that its library reflects realistic and diverse medical scenarios (not just idealized textbook images).

Data Processing and 3D Model Creation: Once the imaging data is obtained, it is processed by engineers and anatomists at IBNE (Institute of Biomedical and Neural Engineering, Reykjavik University). Using medical image processing and segmentation software, the team converts the 2D scan slices into a 3D digital model of the anatomy. This involves segmenting different tissues or structures from the images, for example, isolating a tumor mass, bone, blood vessels, and so on, each as separate 3D structures. The outcome is a high-fidelity 3D model that can be viewed on a computer. The RAIL workflow often uses standard tools like Materialise Mimics for segmentation and 3-Matic for post-processing, ensuring the models are accurate and optimized, since they are considered as medical devices. According to the platform's documented workflow, a specific region of interest is extracted from the scans and transformed

into “a detailed 3D digital model, producing an accurate replica of the patient’s anatomy”. At this stage, the model can be saved in formats suitable for both visualization and 3D printing (such as STL files).

Central Digital Library (Database): The digital models are then uploaded to the RAIL online platform, essentially a database and web interface that constitutes the library. Each model entry in the library is accompanied by metadata: the case description (e.g. diagnosis or key learning points), the anatomical region, modality of origin (CT or MRI), and any segmentation notes. The library is organized by categories (for example, Head, Heart, Pelvis, Knee) so that users can easily find cases of interest. Every anatomy is coupled with a state-of-the-art description from medical manuals and encyclopedias. Users access the library through a secure website (rail.ru.is) where they can browse available models or search for specific conditions. The platform being online means that all participating institutions (the hospital and the universities) are always accessing the latest content from a single source. There is also a version control aspect – if a model is improved or updated (say, refined segmentation), the library ensures everyone sees the updated version. Importantly, the RAIL library is not static; it is designed to expand. The “Request a model” feature on the site allows educators or clinicians to propose new cases, which the team then processes, as described earlier. This creates a feedback loop in the architecture: educational demand can directly drive the addition of new content.

Mixed Reality Workstations: Each of the four partners has a dedicated AR/VR workstation set up for RAIL. These workstations typically consist of a high-performance computer pre-loaded with the RAIL visualization software and one or more XR headsets (such as the Oculus/Meta VR headset). The visualization software is a commercial application developed to streamline 3D anatomies in XR and RAIL provide a downloadable file compatible with this app. When a user wants to use a model in AR, the software fetches the model from its local library and renders it in the headset. The AR software often allows basic and advanced interactions: scaling the model, cutting sections, or annotating parts, recording voice memos, taking measurements and collaborates with other users on the same project. Because each university has this setup, students across different campuses can get a comparable AR learning experience. The use of AR or XR devices is significant because these allow the user to see the real environment and the virtual anatomy simultaneously, which is excellent for group discussion when the models are streamed on a screen. The architecture also supports collaborative XR sessions: two remote sites can join the same session so that, for instance, an instructor at the hospital and a class at the university can co-observe the model. This capability is in line with the platform’s emphasis that XR “eliminates geographical barriers” in shared training experiences.

Mobile and Web Access : Not everyone needs an AR headset to benefit from RAIL. A crucial part of the system architecture is the web-based viewer for the 3D models. By partnering with existing solutions like the Materialise Mimics Viewer (a secure online 3D viewing platform), RAIL enables any authorized user to open a model in their web browser and interact with it (rotate, zoom, pan, measure dimensions, etc.). This means a medical student revising anatomy at home can pull up, say, the pelvic fracture case on their laptop, tablet or mobile phone, and study the model in 3D without specialized hardware. The viewer

works on standard PCs and mobile devices, bringing portability to the RAIL system. The only requirement is an internet connection and login credentials. This aspect of the architecture is particularly powerful for inclusive education, it ensures that even if a user cannot attend the AR lab physically, they can still access the models virtually. Moreover, it supports clinicians who may want to quickly review a model on a tablet during a patient consultation or a team meeting.

3D Printing Service: While digital viewing is the primary mode for most educational interactions, RAIL's architecture also includes a pipeline for producing physical replicas. If a physical 3D model is needed (for example, for surgical simulation with instruments or to hand out in a classroom), the digital model from the library can be sent to a 3D printer. RAIL's base at Reykjavik University hosts an advanced 3D printing facility (the ICAAM – Icelandic Center for Advanced Additive Manufacturing) featuring a multi-material anatomical 3D printer. The process involves preparing the model file (hollowing, adding support structures, etc.) and selecting appropriate materials (rigid resins for bone, flexible materials for soft tissue, etc., depending on the user's requests). These printed models are extremely useful: they are used in surgical rehearsals (surgeons can practice cuts or drill into a printed bone) and in educational displays or exams. In addition, with the advent of Digital Anatomy Printing (J850 DAP, Stratays, Israel) models "look" real even from the tactile point of view. The machine can bland the resins in way that the haptic response of the printed part is similar to the biological counterpart. The turnaround time for printing a model can be hours to a couple of days, so this is usually planned for specific needs (e.g., a scheduled training session). Each institution can request a 3D print through the platform, and the print is then produced and delivered to them, creating a hybrid analog-digital training ecosystem.

Overall, the RAIL system architecture is designed to be robust, flexible, and user-centric. It connects the dots from hospital imaging data to end-user educational content, providing multiple modalities of access. This architecture exemplifies how integrating health IT (PACS), engineering (3D modeling/printing), and XR interfaces can create a powerful new infrastructure for surgical education. Every component – data, processing, library, AR stations, web viewer, printers – works in concert to deliver a comprehensive learning experience that can be accessed in classrooms, clinics, or even at home.

5.3 Innovation Aspects

RAIL embodies multiple dimensions of innovation – pedagogical, clinical, technological, and infrastructural – all rooted in clever integration of existing tools and methods. Instead of creating one new device or procedure, the project's novelty lies in how it blends technologies and workflows to transform surgical education. Below, we analyze these aspects in turn, emphasizing the meaningful convergence of pedagogy, clinical practice, and tech infrastructure.

5.3.1 Pedagogical Innovation

From an educational standpoint, RAIL introduces a more immersive and interactive learning experience for medical students and trainees. By providing digital

3D models of human anatomy (including both normal anatomies and complex pathologies), the platform allows learners to visualize and manipulate anatomical structures in ways traditional textbooks or even cadavers cannot. Studies have shown that AR/VR tools enhance spatial understanding of anatomy and improve knowledge retention by enabling "hands-on" exploration of structures and conditions in a risk-free environment. RAIL leverages this by offering an AR/VR interface where students can virtually dissect or enlarge anatomical models and observe pathological variations. This kind of active learning experience, where students engage with lifelike 3D content, can "revolutionize the way teaching is delivered" by moving from passive observation to active participation. For example, a medical student studying neuroanatomy can examine a 3D brain model with a tumor or hemorrhage in AR, walking around it or slicing through layers virtually, thereby gaining a 3D understanding that is hard to achieve with 2D images alone. Such pedagogical integration aligns with best practices in modern medical education that favor simulation and visualization to overcome limitations of cadaver-based training. Nonetheless, RAIL offers the user a dedicated cross link to medical manuals and encyclopedia to read about anatomy and pathology in the more classic way, believing that the innovation is in the integration and not on substitution but in the integration. In addition, RAIL's library of cases includes not just normal anatomy but real clinical cases (e.g. a complex cardiac malformation or a pelvic fracture), exposing students to variability and pathology early in training. This case-based learning approach enriches education by bridging theory to real-world examples. Learners can attempt to plan a procedure on a virtual model of an actual patient case, fostering clinical reasoning in a safe setting. Overall, the pedagogical innovation of RAIL is in creating an extended classroom where anatomy and surgery come alive through integrated XR and 3D content, promoting deeper understanding, interactivity, and learner confidence.

5.3.2 Clinical and Training Innovation

Clinically, RAIL extends benefits to surgical training and preoperative planning for professionals. It provides surgeons and residents with patient-specific 3D models that can be used to rehearse surgeries and improve planning. By converting a patient's CT or MRI scans into a tangible 3D model, surgeons can better visualize complex anatomies (such as the spatial relationship of a tumor to surrounding organs or the intricate anatomy of a congenital heart defect) before entering the operating room. This approach has been shown to enhance surgical outcomes: using 3D models for pre-surgical planning can significantly improve precision, reduce operative times, and decrease intraoperative surprises [269]. In RAIL's workflow, a high-resolution scan is first segmented and converted into a detailed 3D digital model, which can then be examined in AR/VR or printed as a physical replica. Surgeons can thus simulate a procedure step-by-step on the model, for instance, practicing the optimal angle for a cranial approach or testing the fit of a prosthetic implant in a 3D-printed bone model, all before the actual surgery. This kind of patient-specific rehearsal is a key innovation that integrates existing technologies (imaging, segmentation software, AR visualization, 3D printing) into a practical training aid. It is not a new concept that simulation improves surgical skills, but RAIL makes it systematically available across institutions. Additionally, RAIL fosters remote and collaborative clinical training: the AR aspect allows an expert surgeon in one location to virtually share a model and guide a trainee elsewhere in real time. Extended Reality in a

shared environment enables "two or more individuals to collaborate on the same virtual project, regardless of their physical locations". This means a specialist at the university hospital can mentor a rural surgeon through a complex case by jointly examining the AR model, effectively facilitating tele-mentoring. Such remote collaboration through AR has already been demonstrated to be feasible in surgical education (for example, prior studies used AR headsets for remote guidance during procedures), and RAIL builds on these successes by incorporating the capability as part of its platform [270]. Clinically, this integration of AR/VR and 3D models shortens the learning curve for new surgeons by providing realistic practice: indeed, recent reviews report that 3D-printed simulators "effectively reduce learning curves and enhance trainees' surgical skills", and AR interventions using devices like the HoloLens have led to measurable improvements in trainee performance. RAIL's innovation is making these benefits routinely accessible, every new case added to the library is a potential training scenario for both students and practicing surgeons to refine their technique and clinical decision-making without risk to patients.

5.3.3 Technological Innovation

Technologically, the RAIL project is innovative in how it synthesizes multiple advanced technologies into one platform. Each component technology, PACS medical imaging archives, segmentation software, 3D printing, AR/VR visualization, was already established on its own. RAIL's leap was to integrate them in a pipeline that seamlessly goes from medical scan to interactive model and distributes that model across various media (virtual, augmented, and physical). The platform capitalizes on high-resolution imaging (CT, MRI) and robust image processing: radiological data is taken from the hospital's Picture Archiving and Communication System (PACS) and processed by biomedical engineers at the university to create accurate 3D reconstructions of anatomical regions of interest. This involves segmentation of tissues (e.g. isolating a tumor, bone, vessel, or organ) using specialized software (such as Materialise Mimics or similar medical devices). The resulting digital model can be rendered in an AR/VR environment using custom software developed by the RAIL team. In practice, a user wearing an AR headset can project the virtual anatomy into their real surroundings, walk around it, and interact with it – for instance, enlarging it or slicing through it to reveal internal structures. At the same time, the platform supports VR viewing for fully immersive interaction, as well as web-based 3D viewing on standard devices. RAIL did not invent AR or 3D printing, but it innovatively combined them: every model in the library is not only viewable in AR but can also be exported for 3D printing. The project benefits of an in-house 3D printing facility (through the Icelandic Center for Advanced Additive Manufacturing, Reykjavik University, Iceland) to produce physical models on demand. By using in-house printers, RAIL avoids the high costs of purchasing models from external companies, thus dramatically cutting expenses. Notably, 3D printed models produced by RAIL typically cost only on the order of 100˘1000 in materials, and can be reused, representing a cost-effective solution for simulation training. The customization afforded by this technology integration is also key: educators or clinicians can request a specific model (say, a rare cardiac anomaly), and the team can generate it from imaging data, tailoring the output to the educational needs.

The platform's technical design also emphasizes multi-platform access. Each of the three participating universities has been equipped with an AR/VR worksta-

tion, including headsets and visualization software, so that students on campus can use RAIL's content in dedicated labs. Meanwhile, the digital library is cloud-based, meaning authorized users (e.g. professors, students, surgeons) can log in remotely to view the models on their personal devices. For mobile and on-the-go access, RAIL leverages an online 3D viewer (the Materialise Mimics Viewer) to share cases; this allows a user to inspect the 3D models in a web browser without any specialized software or licenses. Taken together, the technological innovation of RAIL is the creation of a unified infrastructure that links hospital image data to a rich, interactive educational experience. This kind of end-to-end integration, from PACS to AR headset, demonstrates how existing technologies can be orchestrated to produce a powerful new educational tool.

5.3.4 Infrastructural Innovation

In addition to pedagogy and technology, RAIL is innovative in its infrastructure and collaborative model. It is a coordinated effort between the national university hospital (Landspítali) and multiple universities, forming a network that breaks traditional silos between clinical and academic institutions. The platform is accessible to clinicians at the hospital and to instructors and students at three universities, fostering an interdisciplinary and multi-institutional approach to medical education and surgical training. By creating a centralized online library of anatomical models, RAIL ensures that educational resources are shared across institutions rather than duplicated in isolation. A medical student at one university can learn from the same digital case that a surgical resident at the hospital is using for rehearsal, promoting a continuity of education from classroom to clinic. This national repository is the first of its kind, reflecting a governmental push for innovative education solutions. In practical terms, the infrastructure comprises a secure cloud platform where anonymized patient imaging data and derived 3D models are stored. Data governance is an important aspect: the hospital enables access to its imaging data (with appropriate ethical clearance and patient consent for educational use), and the Institute of Biomedical and Neural Engineering (IBNE) at the university processes the data into usable models. IBNE has been a pioneer in medical 3D modeling for years – since 2005 it has operated one of the world's first hospital-integrated 3D printing services for surgical planning, and RAIL builds on this foundation by scaling it up and making it broadly available. The project's infrastructure also includes a model request system: if an instructor or clinician identifies a need (for example, a specific pathology not yet in the library), they can request a model through the RAIL web portal. The team can then retrieve the relevant scans from the PACS database, create the 3D model, and upload it to the library for all to use. This on-demand expansion capability ensures the library stays responsive to educational needs and continues to grow with clinically relevant content. Another infrastructural innovation is that RAIL operates on a multi-modal distribution model, physical, desktop, and XR, without requiring software licenses for end users. By negotiating the integration of tools like the Mimics Viewer and custom visualization software ELUCIS, RAIL ensures any student with an internet connection can access the content, which democratizes advanced surgical education tools. In summary, the infrastructural innovation of RAIL lies in the creation of a collaborative, nation-wide platform that unites data, technology, and people (students, educators, surgeons) into a single ecosystem for surgical training and medical education. This breaks new ground in how educational content is curated and shared across institutional boundaries.

5.4 Benchmark Cases

As a proof of concept, the RAIL platform initially launched with four case studies, each showcasing the system's capabilities in a different anatomical region and clinical scenario. These cases demonstrate how real-world medical data can be transformed into teaching and training material. Below are the four featured cases available on the RAIL website, which collectively span neurosurgery, oncology, cardiology, and orthopedics:

Head: The first case study is centered on the head, providing a detailed 3D model of cranial anatomy derived from CT and MRI. This model includes the skull, brain, ventricles, and white matter branches, segmented in different colors for clarity. A cross-sectional view of the brain is incorporated, allowing users to inspect internal structures in 3D. This head model also features a pathological finding, an intracranial tumor, demonstrating the spatial interaction with the surrounding tissues. In addition, a jaw malformation is depicted together with the nerves, serving as a scaffold for a distractive osteogenesis. Medical students can use the AR/VR interface to explore this model, reinforcing neuroanatomy lessons by visualizing the brain from any angle and observing how a lesion relates to surrounding anatomy. Neurosurgery residents, on the other hand, can use the model to plan approaches for skull base surgery or practice interpreting scans in 3D. Maxillo-facial surgeons can study the curvature of the facial nerve to plan the position of the distractor, and eventually request a 3D printed copy to pretension the device onto the model.
The head case thus exemplifies the educational value of linking radiological data to a tangible model: it bridges the gap between reading a 2D brain MRI/CT and actually seeing the anatomy in 3D space, improving comprehension and spatial reasoning.

Heart: The second case study showcases the heart, highlighting RAIL's utility in cardiac education and surgical planning. This 3D heart models are segmented from a high-resolution cardiac CT scan and presents an anatomically accurate rendering of the heart chambers, valves, and major vessels. Different components (myocardial walls, septum, valves) are color-coded in the model to aid identification. As a proof of concept of pathology integration, the heart model includes a congenital defect scenario, a ventricular septal defect (a hole in the wall between left and right ventricles) or an aneurysm of the aorta and an aortic stenosis. Moreover, a giant tumor developing from the upper myocardium is compressing the aorta and the heart chambers. Lastly, a rare malformation known as aberrant tendinous cords with tethering of the tricuspid leaflets, likely representing an atypical form of Ebstein's anomaly is presented.
In AR, a cardiology trainee can enlarge the virtual heart to human size or bigger and walk around it to see the defect from both ventricular sides, an impossibility with cadaveric hearts or textbooks. Surgeons can use the model for planning interventions (e.g. device closure of the septal defect or surgical repair), and even for patient education – showing a patient their heart model with the problem clearly visualized. This cardiac case underlines how RAIL integrates imaging and 3D modeling to improve understanding of complex 3D relationships in the heart, which is vital for training in cardiothoracic surgery.

Pelvis: The third case focuses on the thoraco-pelvic region, demonstrating RAIL's application in neuro-orthopedic and oncology surgical training. The model is derived from a CT scan of the pelvis (hip bones, sacrum, and femur heads) and includes a pathological example such as a pelvic bone tumor (for example, an osteosarcoma in the ilium) or a complex neurofibromatosis. In addition, a total hip artoplasty with a prostetic implants is presented on one side, whereas on the other an Osteogenesis Imperfecta is shown as alternative to the implant.
This case is particularly challenging anatomically, as the pelvis has a complicated 3D shape and is difficult to visualize with traditional methods. Using RAIL, orthopedic residents can study the pelvis model in VR to understand the spatial orientation of the tumor or fracture fragments. The AR view allows an instructor to point out key structures, for instance, how a tumor abuts critical nerves or blood vessels, by overlaying the model with the images. For surgical planning, having a 3D model of a pelvic tumor is invaluable; surgeons can practice the resection on a 3D print of the pelvis, ensuring clear margins while preserving as much healthy tissue as possible. This pelvic case demonstrates the integration of RAIL with surgical planning: after practicing virtually, the team can print the pelvis model to guide the actual surgery. Clinically, such an approach can improve accuracy in tumor removal and is a clear proof-of-concept of how the library content can translate to real patient care. Pedagogically, the case gives learners a concrete grasp of pelvic anatomy and pathology, which is otherwise hard to obtain short of seeing it in an actual surgery.

Knee: The fourth case study is a knee model, emphasizing arthroscopic anatomy and common pathology in the knee joint. Figure 5.3 shows the web-page of the case. Derived from MRI and CT imaging, these models includes the distal femur, proximal tibia, patella, and soft tissues such as menisci and cruciate ligaments, each reconstructed in 3D. A typical pathology included is a degenerative changes from osteoarthritis or different types of tumors around the joint.
In an AR simulation, users can visualize the knee's internal structures as if they had X-ray vision, rotating the joint and virtually "peeling back" layers to see the ligament inside. Orthopedic trainees can benefit by correlating what they see through an arthroscope in surgery with the 3D model in VR, improving their mental mapping of 2D arthroscopic views to 3D anatomy. The RAIL knee case also allows quantitative measurements: for example, the degree of tibial plateau coverage by the meniscus can be measured on the digital model, or the alignment angles can be checked, reinforcing concepts from orthopedic biomechanics classes. Moreover, this model can be used with 3D printing to create a knee phantom for practicing arthroscopy skills or evaluating implant fit for knee replacements. As a proof of concept, the knee case confirms that RAIL can cover not just hard organs like brain or heart, but also musculoskeletal structures with both bone and soft tissue – broadening the platform's applicability to various surgical fields.

Each of these four cases was carefully chosen to validate a different use scenario of RAIL. Together, they serve as an existence proof that the platform's pipeline (from imaging to AR/VR to 3D print) works across different body systems and clinical questions. They have been used in demonstrations and early user testing, with feedback indicating that the 3D interactive models significantly aid in comprehension of anatomy and pathology. These cases form the foundation of the RAIL library, which is expected to expand with many more entries as the project continues.

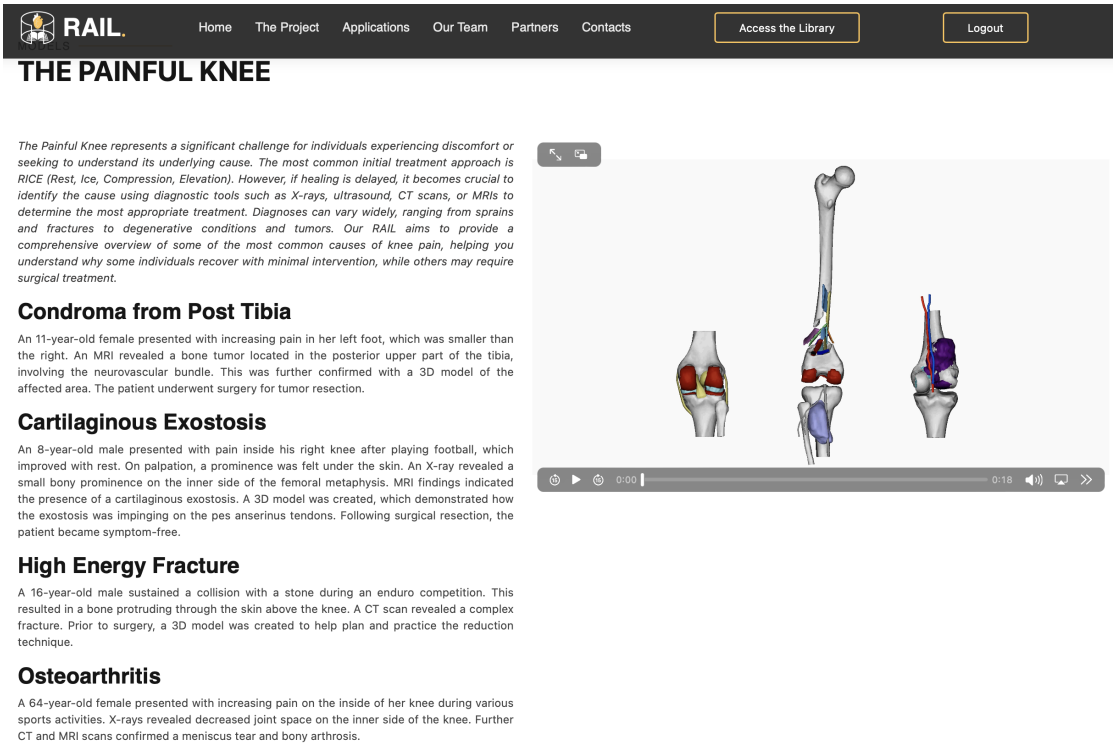

Figure 5.3: Painful Knee case outlook.

5.5 Impact and Future Directions

In its current state, RAIL is almost ready to transform surgical education practices in Iceland. The current challenges are in the identification of what data can be retrospectively included into the database and how to integrate new scans. The work is in identifying the correct platform to let patients decided wether they give consent in using their anonymized data for teaching or not. Pedagogically, RAIL's impact is seen in the shift toward a more interdisciplinary learning environment. Medical students, radiology trainees, and surgical residents may meet in joint sessions to discuss a case from their different perspectives, breaking down traditional departmental barriers in teaching. This kind of collaboration in XR was previously hard to achieve, but RAIL has provided a platform for it. Moving forward, the future directions for RAIL are expansive. One major avenue is to broaden the content: the team plans to continuously add new cases to the library, aiming for a comprehensive atlas of human anatomy and pathology. This will involve scanning and modeling more cases across specialties, from neurology (e.g. spinal deformities) to ENT (sinus anatomy), from oncology (various tumors) to trauma (complex fractures). As the library grows, it will increase in educational value, allowing comparative learning (e.g. normal vs. pathological models side by side). Additionally, there is interest in integrating more advanced visualization techniques. For example, future development may include mixed reality holographic overlays onto actual patients or manikins for enhanced simulation (imagine seeing the hologram of a patient's internal anatomy projected onto their body during a physical exam skills session). The platform might also incorporate haptic feedback devices in the future so that users can feel resistance when interacting with virtual tissues, addressing the current limitation of lacking tactile sensation. Technologically, as AR/VR hardware evolves (lighter headsets, higher resolution displays), RAIL will adapt to leverage these improvements.

Another future direction is rigorous evaluation and research. Being a pioneering project, RAIL offers an opportunity to formally study the outcomes of XR-based training versus traditional methods. The team might plans to assess metrics such as exam performance, skill acquisition speed, or surgical error rates among those trained with RAIL resources. This could contribute to the growing body of evidence supporting XR in medical education, helping to address calls in the literature for more validation of AR/VR effectiveness. Early indications, including systematic reviews, are positive but emphasize the need for high-quality studies. RAIL could serve as a testbed for such studies, given its controlled roll-out across institutions.

In terms of infrastructure, a future goal is to make RAIL sustainable and expandable beyond Iceland. The concept of a shared anatomical library with AR/VR support could be extended to international collaborations, for example, partnering with medical schools in other countries to exchange cases or co-develop content. Since the platform is online, additional institutions could join, turning RAIL into a global repository of surgical training models. This raises the potential for a network effect: as more users contribute unique cases (different pathologies might be more common in different regions), the library becomes richer for everyone. Ensuring patient privacy and data security will remain a priority in this expansion, likely involving continued de-identification protocols and possibly synthetic data generation for rare pathologies.

From a clinical perspective, the adoption of platforms like RAIL hints at a future where extended reality becomes a standard adjunct in surgical practice. We may envision routine surgical team briefings in AR, reviewing the patient-specific model before an operation, much like pilots go through simulations before a flight. As XR hardware becomes more common in hospitals (some operating rooms are already experimenting with AR guidance systems), RAIL's content could integrate with live surgery, for example, overlaying the 3D model onto a surgeon's AR headset during the procedure for real-time navigation assistance. This blurs the line between training and practice, fostering a continuous learning loop.

In conclusion, the RAIL platform's innovative integration of existing technologies may have a significant impact on surgical education by making learning more interactive, collaborative, and case-based. It serves as a model for how to modernize training without exorbitant cost, indeed, by smart use of in-house resources and digital distribution, it lowers barriers for advanced simulation. As RAIL evolves, it is poised to contribute substantially to the future of surgical training, where learning is increasingly immersive, data-driven, and interdisciplinary. The project underscores that innovation in education often stems not from creating something entirely new, but from intelligently combining proven tools in a way that amplifies their collective value. RAIL's journey thus far validates the approach of integration over invention, and its trajectory suggests that the coming years will bring even deeper integration of technology into the art and science of surgical education, to the ultimate benefit of both practitioners and patients.

Chapter 6

Discussion

6.1 Digital Transformation in Medical Imaging: Unlocking New Information

Medical imaging has entered a digital age characterized by fast, inexpensive, and powerful technologies that are fundamentally reshaping the field. The transition from analog film to digital images and the broader digitalization of workflows (e.g., Picture Archiving and Communication Systems, PACS) have not only improved efficiency but also enabled clinicians and researchers to extract clinical information that was once inaccessible or left to subjective interpretation. A prime example is the emergence of radiomics, which leverages computational analysis to quantify imaging features. Radiomics techniques can automatically extract subtle attributes of lesions, such as shape irregularities, textural patterns, or intensity distributions, that are not discernible to the naked eye [271]. By converting images into high-dimensional data, radiomics provides objective information and has been shown to overcome the limitations of human visual assessment and inter-reader variability [272].

Modern imaging allows for the extraction of advanced features such as radiodensity values (in Hounsfield Units) and frequency-domain texture components, which have been shown to reflect underlying tissue characteristics. For example, first-order statistical measures of radiodensity can help distinguish between fat, water-equivalent, and muscular tissues, based on their specific attenuation profiles. This is particularly useful in CT imaging, where quantitative analysis of radiodensity distributions enables the estimation of tissue composition and the assessment of pathological changes.

In summary, digital transformation turns medical images into rich data sources: what was formerly a static picture on a lightbox can now be mined for quantitative biomarkers, revealing patterns linked to disease characteristics or prognosis that clinicians might otherwise miss.

Equally important is how digital imaging enhances consistency and reproducibility in diagnostics. In traditional practice, image interpretation heavily relied on radiologist expertise and qualitative judgment. This subjectivity meant that findings could vary between observers or across institutions. Digital imaging, however, lays the groundwork for more standardized and data-driven evaluations. For instance, the development of quantitative imaging biomarkers allows measurements (like tumor volume, texture, or tissue-specific density) to be made objectively and repeatedly. Studies highlight that radiomics and other quantitative imaging approaches yield measurable features that improve diagnostic and

prognostic assessments in a way that is far more reproducible than manual interpretation [273]. By capturing numeric values from pixels and voxels, digital tools reduce the ambiguity of descriptive terms and enable direct comparisons over time or between patients. This capability, impossible in the era of analog film, underscores the transformative power of digitalization: it changes medical imaging from a primarily qualitative art into a quantitative science. Clinically, this means additional information can be extracted from routine scans (for example, texture indices correlating with tumor heterogeneity, perfusion metrics in tissue, or fat/muscle ratio alterations in cardiomyopathy) to guide decision-making.

The importance of digitalization thus lies not only in convenience but in the fundamental enrichment of what imaging can tell us about a patient's condition. In summary, the digital transformation of medical imaging provides a foundation for innovation, where data-driven analyses yield insights that were previously beyond reach or too reliant on observer experience.

Artificial Intelligence: Among the advances propelled by digital transformation, the rise of artificial intelligence (AI) in medical imaging stands out as a transformative force. AI encompasses a broad range of computational techniques, including traditional machine learning, rule-based algorithms, and deep learning (DL) models, which together enable machines to interpret, learn from, and act upon complex medical data. The relationship between digital transformation and AI is inherently synergistic: digitalization provides the infrastructure and standardized data, while AI unlocks sophisticated analysis, interpretation, and decision support.

The digital transformation of radiology has established the foundation for AI integration, with fully digital workflows, high-resolution scanners, structured reporting, and centralized data repositories such as Picture Archiving and Communication Systems (PACS). These advancements have not only streamlined imaging operations but also ensured the availability of vast, high-quality, and annotated datasets—essential fuel for training and deploying AI models. For example, standardized formats like DICOM and the expansion of cloud-based storage facilitate multi-institutional data sharing, a key enabler for scalable and generalizable AI solutions.

AI excels in extracting insights from medical images that are difficult for human observers to quantify. It supports a wide range of applications, including the detection of abnormalities, disease classification, image segmentation, reconstruction, and predictive analytics. Convolutional neural networks (CNNs), support vector machines (SVMs), and ensemble classifiers have shown high accuracy in identifying pathologies such as lung nodules, mammographic microcalcifications, and brain tumors, in some cases matching or surpassing the diagnostic accuracy of experienced radiologists [274], [275]. Additionally, AI tools can analyze hundreds of slices from CT or MRI scans rapidly, consistently flagging subtle findings like early infarcts or small lesions that might elude human detection. Unlike clinicians, AI does not suffer from fatigue, maintaining consistent performance and mitigating human-related diagnostic errors.

Deep learning models, particularly CNNs and their variants such as U-Net, ResNet, and DenseNet, are capable of learning hierarchical representations from raw image data [276], [277]. These architectures can perform end-to-end tasks, from raw pixel input to disease probability output, and are particularly effective for tasks like lesion detection, organ segmentation, and tumor classification [278], [279]. Recurrent neural networks (RNNs) and attention-based models such as

transformers are also being explored for temporal imaging tasks, such as dynamic MRI or longitudinal CT analysis, where time-series data are involved [280].

Generative models, including variational autoencoders (VAEs) and generative adversarial networks (GANs), are increasingly employed for data augmentation, image reconstruction, and anomaly detection. These models are capable of synthesizing realistic medical images, filling missing data, or simulating pathological scenarios for training and evaluation [281].

Beyond interpretation, AI is increasingly embedded across the entire imaging pipeline. During acquisition, AI-based reconstruction algorithms can enhance image quality while reducing scan times or radiation doses [282]. At the interpretation stage, AI systems can triage studies by urgency, highlight suspicious regions, suggest differential diagnoses, or even draft preliminary reports, effectively acting as a second reader or assistant [283]–[286]. This integration allows radiologists to allocate more time to complex cases, improving both diagnostic efficiency and patient outcomes.

Despite their performance, deep learning models face several limitations in medical imaging. These include a lack of transparency, dependency on large labeled datasets, high computational costs, and difficulty in interpreting model outputs. Saliency maps and output probability distributions are often employed to enhance explainability, yet they remain imperfect proxies of the model's reasoning [287]. Furthermore, DL systems often process entire image volumes indiscriminately, analyzing all pixels even when most are clinically irrelevant, which leads to inefficiencies and reduced explainability.

To address these issues, alternative interpretable approaches have emerged, offering increased transparency and clinical alignment. Among them, explanation by example and semantic explanation methods attempt to mimic human reasoning by retrieving comparable cases or translating internal model features into meaningful clinical terms. Rule-based systems are used in automated measurement tools and structured reporting, while classical machine learning continues to be valuable where data volume or labeling is limited. Hybrid approaches that combine clinical knowledge with data-driven learning offer practical and explainable solutions, especially in settings where transparency and interpretability are essential [288].

6.2 Implications for Clinical Practice

The convergence of digital transformation and advanced analytics has far-reaching implications in clinical environments. Key areas of impact include diagnostic accuracy and speed, education and training of medical professionals, personalized patient care, and overall operational efficiency in healthcare delivery. Below, we discuss each of these in turn, highlighting how the digital imaging revolution is reshaping practice on the ground.

6.2.1 Enhanced Diagnostic and Personalized Care

The digital transformation of medical imaging has significantly enhanced diagnostic accuracy and enabled a paradigm shift toward personalized, patient-centered care. High-resolution digital images, when combined with computer-aided detection and artificial intelligence (AI), empower clinicians to detect pathologies earlier and more reliably. Deep learning models have demonstrated expert-level performance in identifying a wide range of conditions—from lung nodules on CT

scans to diabetic retinopathy in fundus photographs [289], [290]. Clinical studies have shown that AI systems can detect abnormalities such as pneumothorax, tumors, or fractures on chest X-rays and MRIs with sensitivity and specificity comparable to radiologists, offering a valuable second opinion that reduces diagnostic errors [291]. These tools excel at exhaustive pixel-level analysis, surpassing the limitations of human observers. Moreover, unlike clinicians, AI systems do not experience fatigue, allowing for uniform application of diagnostic criteria.

AI integration into digital workflows also improves consistency, for instance by automatically generating preliminary findings or measurements in radiology reports [292]. This consistency enhances the likelihood of accurate initial diagnoses and supports reliable quantitative comparisons across timepoints. Digital platforms facilitate multimodal image integration—such as PET and CT fusion—while enabling immediate access to prior studies. Tools that align scans and highlight changes over time help radiologists make more informed interpretations [293].

Quantitative analysis further supports clinical decision-making. Lesion size, volume, and growth metrics can be extracted automatically and reproducibly, enabling standardized tracking of disease progression or treatment response [294]. For example, algorithms aligned with RECIST criteria can assess tumor responses with objectivity and consistency [295], [296]. Automated triage systems also prioritize urgent findings (e.g., intracranial hemorrhage), reducing time to intervention in emergencies.

By transforming images into mineable data, clinicians can extract patient-specific biomarkers and stratify risk profiles. Radiomic features derived from CT or MRI scans have been correlated with gene expression patterns and clinical outcomes, supporting a form of imaging-based phenotyping [297]. These insights enable personalized treatment strategies, such as selecting chemotherapy regimens or tailoring radiation therapy based on tumor heterogeneity or radiosensitivity [298]. For example, researchers have shown that integrating radiomics, PET-derived metabolic data, and genomic information allows for customized radiation dosing, maximizing tumor control while minimizing toxicity [48].

Beyond oncology, quantitative metrics from cardiac MRI—such as ejection fraction or scar burden—can feed predictive models to guide therapeutic interventions in heart disease. In neurology, quantitative MRI enables disease activity tracking in multiple sclerosis. These individualized approaches are no longer confined to clinical trials but are increasingly adopted in routine practice due to scalable digital tools.

Digital imaging also enhances patient-centered care. Since imaging data are digital, clinicians can share annotated or 3D-rendered scans with patients, improving transparency, understanding, and adherence. In summary, the convergence of digital transformation and AI enhances diagnostic precision, supports risk stratification, and enables tailored therapeutic approaches. These tools promote timely, reproducible, and individualized care while fostering deeper patient engagement—ultimately improving outcomes across diverse clinical contexts.

6.2.2 Education and Training of Clinicians

Digital transformation is not only changing how we diagnose, but also how we train the next generation of medical professionals. In radiology, anatomopathology and related fields, educational paradigms should evolved accordingly to digital tools. However, several studies report teaching methods falling behind the advancement in technology due to limitations in changing paradigm. What is

unanimously agreed is that interactive, case-based learning is the most promising teaching method, since it resemble real life scenarios, especially for radiologist but not limited to. In this scenario, the instructors share cases, providing clinical history and letting the students figure out the situation [299].
Residents and medical students today might access vast digital archives of imaging cases, interactive learning platforms, and even simulation environments that were unavailable to previous generations. For instance, online case libraries and teaching file systems (often integrated with PACS) allow trainees to study thousands of annotated cases spanning a wide range of pathologies at their own pace. This exposure helps them recognize both common and rare conditions more readily. The ability to share and access images globally means a trainee in one hospital can learn from unique cases that occurred elsewhere, vastly expanding the learning opportunities beyond what a single institution's experience might offer. A three years study with almost 300 fourth-year students on transitioning to a case-based learning with radiological images and team collaboration instead of frontal lecture for oral and maxillofacial radiology reported that more then 70% of participants reported that the new method helped them in learn the content in a more comprehensive manner and almost 80% felt the in-class discussion increased their knowledge of radiographic interpretation. National Board Dental Examination results for these classes showed slight improvement when compared to national scores [300].
In addition to the shift of teaching method, simulation and virtual training technologies can benefit to medical imaging education. Digital simulation software can mimic the experience of performing imaging-guided procedures or interpreting studies in a risk-free setting. For radiology residents and fellows, a core component of their training is applying anatomy and pathology to accurately interpret medical images of various modalities, and immersive environment enhance their engagement [301], [302]. Trainees can, for example, practice reading trauma CT scans or performing ultrasound-guided biopsies on virtual patients using realistic scenarios. These tools provide immediate feedback and can be repeated until proficiency is achieved.
These approaches are not only innovative, but provide an interesting experience for students and residents improving their learning curve. Virtual Reality lab for undergraduates medical students impacted they learning outcome by increasing the success in weekly quizzes from 75% (national average) to 96%. [303]. Second year medical students trained with HoloAnatomy (Figure 6.1) spent less time in lab (4.1hours) compared to the cadaveric dissection lab (7.4 hours) achieving the same overall end of class score [304]. A randomized study on long term retention of skills and knowledge acquired during breast anatomy class reported that mixed reality outperformed cadaveric dissection even though the two groups scored the same at end of class test. [305]. Distance learning alone, with virtual reality simulation, allowed during COVID-19 pandemic to keep the learning outcome pf anatomy class on the same standards then previous years, pointing out that even alone can be a beneficial tool [306]. Moreover, mobile app combined with AR models enhanced students' engagement in anatomy class, favoring individual studies and highlighted the interactive feature as the real benefit of the application [307]. The solution I proposed in 5 is based on these principles, merging together interaction, case-based scenarios, engaging technology as XR and encyclopedic knowledge for reference.

Additionally, AI is beginning to play a role in education: intelligent tutoring systems can quiz trainees on cases, and some educational software uses AI to adjust the difficulty of cases presented based on the learner's performance. There

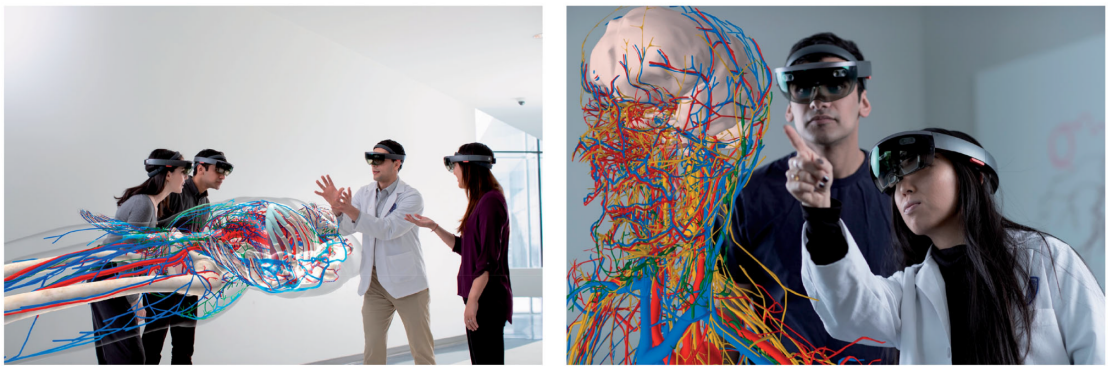

Figure 6.1: HoloAnatomy class. Image from "Mixed reality as a time-efficient alternative to cadaveric dissection" [304]

are even AI tools that can provide a second opinion to a trainee's interpretation, effectively acting as a virtual "co-pilot" and pointing out missed findings to accelerate learning. The practical impact of these digital training advances is a workforce that is better prepared for modern practice. However, we are still far from there. Almost 80% of radiologist interviewed in a study from Collado et. al. believe that in one or two decades their job will be drastically changed due to AI and ML in diagnostic, the 30% reported of using AI/ML daily in their clinical routine and none of them is trained on AI/ML for big data analytics, some of them never heard this terms before the survey [308]. A recent review study highlighted the need for better training about AI in radiology and medical field. Many AI training programs offered to radiologists, yet most of them (80%) are short, stand-alone sessions, which are not part of a longer-term learning trajectory. The training programs mainly (around 85%) focus on the basic concepts of AI and are offered in passive mode. Professional institutions and commercial companies are active in offering the programs (91%), though academic institutes are limitedly involved [309].

Digital platforms will facilitate interactive and case-based learning and will support remote and collaborative teaching. Through video conferencing and cloud-based image viewers, trainees and experts can discuss cases in real time, even if they are continents apart. This means mentorship and specialist input are no longer bound by geography, a significant boon for training programs in areas that may lack local subspecialists.
New radiologists and clinicians will graduate with familiarity in advanced imaging analytics and AI, understanding not only how to use these tools but also their limitations. The training emphasis has shifted to ensure clinicians can effectively work alongside AI and interpret its outputs, an important skill as these technologies become routine in practice. All told, digital transformation will revolutionized medical education by making it more accessible, interactive, and aligned with real-world demands. This ultimately improves patient care, as well-trained professionals are more adept at using cutting-edge imaging technologies and interpreting results accurately.

6.3 Thesis Contribution

The studies presented in Chapters 2, 3 and 4 collectively demonstrate how pixel-intensity analysis of medical images can yield quantitative biomarkers to enhance diagnosis across diverse clinical domains. In each case, raw grayscale values –

whether Hounsfield units (HU) in computed tomography (CT) or gray levels in infrared imaging – were leveraged to extract meaningful information about tissue composition and pathology. For example, Chapter 2 showed that analyzing CT radiodensity of aging skeletal muscle can quantify intramuscular fat and muscle quality, complementing traditional muscle volume measures. Chapter 3 extended this concept to the heart, where radiomics (high-dimensional features derived from pixel intensity distributions and textures) was applied to cardiac CT images to perform "virtual histology," identifying subtle myocardial patterns that differentiate acute myocardial infarction (AMI) and hypertrophic cardiomyopathy (HCM). Likewise, Chapter 4 introduced an automated Meibography analysis in which infrared image intensity profiles of the eyelids were used to detect and measure Meibomian glands, yielding objective metrics of gland atrophy in dry eye disease. Despite spanning musculoskeletal, cardiac, and ophthalmic fields, all three studies share a unifying approach: converting pixel intensity data into quantitative indicators of tissue health, thereby moving beyond qualitative image interpretation and towards more data-driven, reproducible diagnostics.

6.3.1 Novel Pixel-Intensity Analysis Methodologies

A key contribution of this thesis is the development of innovative methodologies that harness pixel intensity information in novel ways. In Chapter 2 (Aging Muscle), a custom CT image segmentation and densitometry pipeline was created to assess sarcopenia. By thresholding CT voxels by their HU values, the muscle tissue was distinguished from fat and connective tissue, enabling 3D reconstruction of muscle volumes and calculation of average muscle density. This yielded a detailed "radiodensiometric" profile of muscle composition – for instance, fat was identified in the HU range –200 to –10, versus muscle in 40 to 200 HU – providing an objective gauge of muscle quality in aging limbs. In Chapter 3 (Virtual Cardiac Histology), the methodology shifted to advanced radiomic feature extraction from coronary CT angiography images. Here, first-order intensity statistics (mean, skewness, entropy of HU distributions) and texture patterns (e.g. gray-level co-occurrence metrics) were computed from the myocardium. These features serve as a quantitative signature of tissue state, capturing changes like the increased heterogeneity and lowered skewness indicative of infarcted myocardium with fatty infiltration or the platykurtic (flattened) intensity profiles associated with diffuse fibrosis in HCM. Machine learning models (e.g. LightGBM and QDA ensembles) were then trained on these radiomic signatures, a novel approach that achieved high accuracy in distinguishing HCM patients – with an AUC up to 0.93 for subject-level classification.

Finally, Chapter 4 (Meibomian Gland Analysis) introduced a new algorithm exploiting gray-value distribution profiles in infrared meibography. Instead of deep learning, which can be resource-intensive, a lightweight pixel-based method was used: the intensity along the eyelid was sampled to detect peaks corresponding to glands and valleys to inter-gland tissue. This allowed automatic tracing of each gland's outline and computation of metrics like gland length, width, and a novel "atrophy index." The atrophy index – defined from pixel brightness patterns – quantifies gland dropout or degeneration across the eyelid, representing the first objective, instrument-derived measure of Meibomian gland health. Each of these methodologies is innovative in replacing subjective or coarse assessments with pixel-level quantitative analysis: from CT histogram thresholding for muscle/fat composition to radiomic feature mining in cardiac tissue and

intensity-profile scanning in ocular imaging. They illustrate the versatility of pixel-intensity analysis as a toolkit, adaptable to different imaging modalities and clinical problems.

6.3.2 Enhanced Diagnostic Capabilities and Clinical Impact

Importantly, these pixel-based approaches were shown to improve diagnostic insight and have clear potential to support clinical decision-making. In the musculoskeletal study, CT intensity analysis provided a more nuanced picture of sarcopenia and its mitigation through intervention. The ten-year longitudinal case in Chapter 2 revealed that, despite an exercise program leading to muscle hypertrophy, there was a mild decline in muscle density (increased intramuscular fat) that was substantially slower than typical age-related decay. This finding, made possible by measuring HU-based radiodensity, underscores how interventions can preserve muscle quality, and it offers a quantitative way to monitor sarcopenia beyond simple mass or strength tests. Clinically, such CT-derived metrics could be used opportunistically (from routine scans) to flag early muscle degeneration or assess the efficacy of a therapy, supporting decisions on geriatric care and rehabilitation.

In the cardiac radiomics study, the enhanced diagnostic capability is even more pronounced: by analyzing myocardial pixel intensities, Chapter 3 demonstrated that routine coronary CT scans (widely available in emergency and outpatient settings) can be repurposed to detect myocardial damage that normally requires specialized MRI. The radiomics-based virtual histology differentiated pathological myocardial tissue from normal with high sensitivity. This quantitative tissue characterization augments what clinicians can glean from CT alone, potentially enabling earlier or more accessible diagnosis. A trained model integrating these features could alert a physician to the presence of an infarct or cardiomyopathic change on a CT scan, prompting timely intervention or further testing. Moreover, because the analysis is quantitative, it reduces observer variability and bias: multiple studies cited in Chapter 3 indicate that integrating radiomic analysis into CT interpretation improves consistency and accuracy of identifying disease features that radiologists might overlook.

Similarly, the automated meibography analysis in Chapter 4 stands to transform clinical dry eye diagnostics. By converting an infrared eyelid image into objective gland measures, it addresses the long-standing issue of subjective grading in Meibomian Gland Dysfunction (MGD). The atrophy index and gland length metrics provide a continuous scale to assess severity of gland loss, replacing coarse categorical "meiboscores" and greatly improving inter-observer agreement. In practical terms, an eye care practitioner could use this tool to instantly quantify a patient's glandular health during an exam – for example, detecting early gland dropout before it becomes obvious, or tracking improvement in gland structure after treatment (e.g. after warm compress therapy). This real-time feedback enables more informed clinical decisions, such as initiating therapy when a threshold of atrophy index is exceeded, or educating patients with visual, numeric evidence of their condition and its response to interventions. Across all three applications, the common impact is a shift toward more precise and objective diagnostics. Pixel-intensity analysis effectively turns standard medical images into sources of rich, quantitative biomarkers. These biomarkers, be it average muscle HU, myocardial texture patterns, or gland brightness profiles, enhance

diagnostic sensitivity (by revealing subtle changes), specificity (by characterizing tissue type or pathology), and consistency (by minimizing subjective interpretation). Ultimately, the methodologies proposed in this thesis can support clinical decision-making by providing additional evidence: for instance, identifying a sarcopenic patient who might otherwise be missed by conventional screening, stratifying a cardiac patient's risk by quantifying fibrosis load on CT, or confirming MGD as the cause of a patient's dry eye symptoms through objective gland analysis.

6.3.3 Implications for Clinical Practice and Future Directions

The success of these studies in extracting diagnostic value from pixel intensities carries several broader implications. First, they exemplify the growing paradigm of "image-based biomarkers", quantitative indicators derived from imaging data that can complement biochemical tests or functional exams in healthcare. The work here shows that even without new imaging hardware, existing modalities can be pushed further with smart analysis: a standard CT scan can double as a muscle quality assay or a cardiac fibrosis detector with the right post-processing algorithms. This opens the door to more integrated care pathways, where a patient's single scan is used to screen for multiple conditions (e.g. using a chest CT to evaluate coronary arteries, myocardial health, and even muscle status in the same sitting). Second, the methodologies are designed with clinical feasibility in mind. The meibography algorithm was explicitly developed to be computationally lightweight for real-time use in clinic, and radiomics analyses, while complex, can be automated in the background of PACS (Picture Archiving and Communication Systems) to assist radiologists without disrupting workflow. Implementing these tools could improve efficiency (by reducing the manual labor of image grading) and enable personalized medicine, as clinicians receive quantitative profiles unique to each patient rather than one-size-fits-all scores. Moreover, the studies highlight how pixel analysis can discover patterns that align with underlying pathology. For instance, Chapter 3's finding that the intraventricular septum in AMI cases showed increased fat-related low-density pixels, versus HCM cases showing high-density fibrotic tails in the histogram, directly links image features to histopathological changes. Such insight builds confidence that these imaging biomarkers truly reflect disease processes, which is crucial for clinical adoption. In the future, these pixel-derived markers might be incorporated into risk models or diagnostic criteria (e.g., a radiodensity threshold for sarcopenia, or an atrophy index cutoff for diagnosing MGD severity). Of course, to reach routine clinical use, further validation is needed. Each study noted the importance of larger, diverse cohorts to ensure generalizability of the findings, for example, the virtual histology approach should be tested in multi-center trials to confirm that radiomic signatures of HCM and AMI hold across imaging protocols and populations. Additionally, integrating these tools with other data (such as clinical risk factors or genomic information) could amplify their diagnostic power. Despite these considerations, the trajectory is clear: pixel-intensity analysis is emerging as a powerful adjunct in diagnostics, turning medical images into quantitative maps of disease. By bridging the gap between qualitative observation and quantitative assessment, the work in this thesis contributes to more data-driven and objective clinical decision-making. Embracing these techniques in practice – whether by radiologists assessing body composition from CT,

cardiologists utilizing radiomic analysis for "virtual biopsy" of the heart, or ophthalmologists quantifying glandular health – can lead to earlier detection, more accurate diagnoses, and better monitoring of treatment outcomes. In summary, the unified contribution of Chapters 3–5 is a demonstration of how novel pixel-based image analysis methodologies can enhance diagnostic capabilities across medicine, laying groundwork for more informed and precision-driven healthcare. Each represents a step toward imaging not just as a visual tool, but as a quantitative science that supports clinical decisions and ultimately improves patient care.

6.3.4 RAIL as an Integrative Platform for Translational Imaging Research

The RadioAnatomical Interactive Library (RAIL, `www.rail.ru.is`) represents a practical extension of the core contributions presented in this thesis, serving as both a digital archive and an interactive dissemination tool for medical imaging cases derived from pixel-based analysis. Unlike traditional repositories, RAIL is designed to facilitate translational integration, enabling clinically annotated image-based case studies, such as those in musculoskeletal aging, cardiac radiomics, and ocular surface disorders, to be shared in formats that support both education and clinical decision-making.

From a research perspective, RAIL embodies a digital infrastructure where results from advanced pixel intensity analysis, such as those detailed in Chapters 2 to 4, can be operationalized. Segmented CT volumes, annotated ROIs, and radiomic profiles generated during the thesis are available through the platform as interactive cases, allowing clinicians and students to engage with them not only visually, but also analytically. This supports a continuum of research-to-clinic translation, where novel methodologies, such as HU-based muscle quality assessment, myocardial virtual histology, or automated Meibomian gland detection, are not merely published but made explorable and reproducible. Researchers can use RAIL to benchmark, validate, or even test AI algorithms on real-world data structures, while clinicians can compare patient cases against digitally archived reference models.

Importantly, RAIL also reflects the clinical integration potential of digital transformation. By connecting directly to the national PACS system and enabling access via hospital and university workstations, the platform facilitates a bidirectional exchange between diagnostic practice and research innovation. For instance, a radiologist interpreting a standard CT scan can consult archived cases with known muscle or myocardial pathology, augmented with the radiodensiometric profiles derived from this thesis. Conversely, new clinical cases uploaded to the system can contribute to expanding the radiomic or morphometric datasets used for machine learning or phenotypic stratification.

The inclusion of augmented reality (AR) viewers further enhances its utility, bridging traditional image review with immersive visualization. This capability supports surgical planning and anatomical education while anchoring it in real patient-derived data. In this way, RAIL does not merely store images, it contextualizes quantitative findings, promotes reproducibility of methods, and fosters adoption of digital diagnostics in real-world clinical settings. By functioning at the intersection of education, research, and care delivery, RAIL exemplifies how digital platforms can operationalize the thesis vision of using image-based

biomarkers to enhance personalized medicine and support informed clinical decisions.

6.4 Challenges, Ethical and Regulatory Considerations

While the digital transformation of medical imaging and the integration of AI offer remarkable benefits, they also introduce new challenges and considerations that must be addressed. It is essential to navigate these issues to ensure that technology is leveraged responsibly and effectively in healthcare. Key challenges include data security and privacy, standardization and interoperability, and the risk of over-reliance on automated systems, among others (such as regulatory approval and ethical considerations of AI, which also warrant attention).

Data Security and Privacy: As imaging has moved into the digital realm, protecting patient data has become a paramount concern. Digital images (and their associated metadata) are part of the patient's health record and often include sensitive personal information. The connectivity that allows easy sharing of images also opens potential vulnerabilities for unauthorized access or cyberattacks. Incidents have been reported where unsecured servers or PACS systems left imaging data exposed to the internet, underscoring the need for robust cybersecurity measures. Hospitals must implement strict access controls, encryption, and robust network security protocols to safeguard imaging archives and other digital assets. Protecting Protected Health Information (PHI) and Personally Identifiable Information (PII) is a legal and ethical responsibility, particularly as healthcare systems become increasingly digitized. In addition to defending against external threats, healthcare organizations must establish strong internal governance to comply with privacy regulations such as the Health Insurance Portability and Accountability Act (HIPAA) in the U.S. and the General Data Protection Regulation (GDPR) in Europe.

Three key frameworks and regulations form the foundation of cybersecurity governance in healthcare: the HITECH Act, the NIST Cybersecurity Framework, and ISO/IEC 27001. Each plays a complementary role in securing health IT systems—from legal compliance to technical standards and global best practices.

The HITECH Act, enacted in 2009, was designed to modernize healthcare IT infrastructure by encouraging the adoption of Electronic Health Records (EHRs) and reinforcing HIPAA's privacy and security requirements. In practical terms, this led providers to migrate from paper to certified digital systems, implement breach notification protocols, and train staff on secure data practices. Organizations demonstrating "meaningful use" of EHRs became eligible for federal incentive programs, while also assuming greater responsibility for protecting patient information.

The NIST Cybersecurity Framework (CSF) provides a structured, risk-based approach to managing cybersecurity threats. Centered around five core functions—Identify, Protect, Detect, Respond, and Recover—it guides hospitals in tasks such as maintaining asset inventories, monitoring systems for threats like ransomware, restricting access to sensitive data, and establishing disaster recovery protocols to ensure continuity of care in the event of a breach.

For global standardization, ISO/IEC 27001 defines the requirements for implementing an Information Security Management System (ISMS). Hospitals that

adopt this framework develop formal security policies, conduct risk assessments, assign clear roles and responsibilities, and perform regular audits. This transforms cybersecurity from an ad-hoc collection of controls into a coherent, auditable governance system.

Together, these initiatives support not only regulatory compliance but also the delivery of secure, resilient, and patient-centered care in an increasingly connected healthcare environment.

Beyond regulatory alignment, practical cybersecurity measures are critical for day-to-day operations. For example, de-identification of medical images is essential when using data for research or AI development, protecting patient privacy while enabling innovation. Additionally, ensuring system uptime and data integrity is vital; a ransomware attack on a PACS (Picture Archiving and Communication System) could severely disrupt clinical workflows. As a result, significant investments in IT infrastructure, staff training, and redundant systems are necessary.

Ultimately, while digital imaging and health IT offer tremendous benefits, they come with serious responsibilities. Effective cybersecurity requires continuous vigilance, strategic planning, and the integration of legal, technical, and operational frameworks to protect patient data and maintain trust.

Ethical & Legal: Beyond the major technical and clinical themes, several ethical and legal considerations must be addressed when integrating computer-assisted detection tools, decision support systems, and other advanced medical technologies into healthcare workflows. One critical issue is the allocation of liability—for instance, determining responsibility if a system fails to flag a serious condition, such as a missed cancer diagnosis, particularly when both the clinician and the technology overlook it. Questions also arise around informed patient consent, especially when data are used for automated analysis, algorithm training, or third-party processing.

Regulatory agencies such as the FDA in the U.S. and CE marking authorities in Europe are developing frameworks for the approval and monitoring of these tools. However, ensuring that these technologies are clinically validated, bias-mitigated, and generalizable across diverse populations remains a major challenge. Many systems are trained or configured using data that may not represent all demographic groups or clinical contexts, potentially leading to inequities in performance.

There is also the matter of workflow integration. Any new digital system—whether for diagnostics, planning, or monitoring—must enhance rather than disrupt clinical operations. Tools that create additional steps or interface poorly with existing infrastructure can increase cognitive load or lead to resistance among healthcare professionals. Seamless integration, including interoperability with existing electronic health records and imaging platforms, is therefore essential.

In certain domains such as digital pathology or high-resolution imaging, the volume and size of data introduce additional concerns, such as storage requirements, processing speed, and transmission capabilities. These often necessitate cloud-based solutions, which, while powerful, raise their own security, compliance, and cost issues.

Another key concern is accessibility. The financial investment required to implement advanced digital tools can be substantial, and not all institutions—particularly in low-resource settings—can afford immediate adoption. This may exacerbate disparities in care quality and access, creating a digital divide in healthcare.

Stakeholders, including policymakers, vendors, and healthcare providers, must work collaboratively to ensure equitable access to technology across different regions and institutions.

The medical imaging and healthcare technology communities are actively engaged in research, standard-setting, and consensus-building to address these concerns. With thoughtful planning, such as adopting robust cybersecurity measures, adhering to international standards, providing training for clinicians, and requiring rigorous clinical validation, the risks associated with digital transformation can be mitigated. Addressing these issues proactively helps ensure that the adoption of digital and computer-assisted systems enhances clinical care, supports professionals, and protects patients.

6.5 Limitation

Despite its promise, the present work is subject to several important limitations. First, the reliance on computed tomography inherently introduces exposure to ionizing radiation, which constrains the feasibility of repeated examinations and limits applicability in younger populations or in large-scale screening programs. The frequent use of iodinated contrast media further narrows the patient pool, as it may pose risks in subjects with impaired renal function or contrast allergies, and creates additional variability depending on injection protocols and timing. Second, CT is intrinsically less sensitive than MRI in soft-tissue characterization, which means that tissue-specific density values may overlap substantially and reduce diagnostic specificity. In particular, musculoskeletal tissues exhibit high inter- and intra-patient variability: muscle attenuation is influenced not only by age and water content but also by comorbidities, hydration status, fat infiltration, and acquisition parameters such as tube voltage or reconstruction kernels. These biological and technical confounders complicate the standardization of Hounsfield Unit thresholds across studies and limit the generalizability of findings. Third, the analysis presented here depended on third-party software for segmentation and feature extraction, which may restrict reproducibility, introduce proprietary bias, and limit integration with clinical workflows. The lack of harmonized protocols across scanners, institutions, and software versions remains a critical barrier to widespread clinical adoption. Moreover, the retrospective and opportunistic use of CT images, while advantageous in terms of availability, comes with heterogeneous acquisition conditions, variable slice thickness, and incomplete metadata, which together may weaken the robustness of quantitative biomarkers. Finally, the limited sample size and restricted pathological cohorts investigated reduce the statistical power of the findings and underscore the need for larger, multi-center validation studies.

Chapter 7

Conclusion and Future Development

The digital transformation of medical imaging, coupled with technological advances in detection algorithm and computer vision tools, represents a pivotal chapter in the evolution of healthcare. This final discussion has explored how digitalization has turned medical imaging into a rich source of data, enabling new insights and more objective analysis than ever before. It has compared the foundational impact of going digital with the analytical revolution brought by AI, illustrating that the synergy of the two is reshaping diagnostic medicine. This thesis demonstrated how the systematic analysis of pixel intensity in medical images can yield robust, quantitative biomarkers to enhance diagnostic precision across diverse clinical domains. Through three applied studies, targeting aging muscle, cardiac pathology, and ocular gland dysfunction, it was shown that raw image data, when processed with tailored segmentation, radiomic, and signal analysis techniques, can reveal subtle pathological changes not discernible to the human eye. These methodologies not only improve diagnostic sensitivity and reproducibility, but also hold promise for real-time clinical decision support. The development of the RadioAnatomical Interactive Library (RAIL) further operationalized these advances, offering a translational platform where imaging data, algorithmic outputs, and educational content converge. Taken together, the contributions of this work position pixel-intensity analysis as a cornerstone of future image-based diagnostics, supporting the broader movement toward personalized and data-driven medicine.

We have seen that in clinical practice, these changes translate to more accurate and earlier diagnoses, more tailored treatments, more efficient operations, and improved training of healthcare professionals. The broader significance of this transformation is profound: it is driving a shift toward precision, efficiency, and connectivity in healthcare that stands to benefit patients and providers alike. From a healthcare perspective, digital imaging and computational software are accelerating a move to evidence-driven, personalized care. Decisions that once relied heavily on physician intuition can now be supported by quantitative metrics and predictive models. A radiologist's role is evolving from solely interpreting images to also curating and integrating data, guided by AI-derived findings. This not only enhances patient outcomes (through early detection and targeted therapy) but also reduces unnecessary procedures and costs by increasing diagnostic confidence.

For patients, the transformation means more consistent care, they are less subject to the luck of which radiologist reads their exam or which hospital they visit,

as standards and AI assistance help level the field. It also means potentially more predictive care; for instance, algorithms might flag individuals at high risk for certain diseases before symptoms arise, enabling preventive measures. In the long run, as imaging merges with other digital health data (genomics, electronic health records, wearable sensor data), we approach a model of care that is proactive and personalized, with medical imaging as a central pillar.
From a medical engineering and innovation perspective, the digital transformation has been a catalyst for interdisciplinary collaboration and technological progress. Engineers, computer scientists, and clinicians are now working hand-in-hand to develop imaging hardware that produces better digital data, and software that intelligently interprets it. This cross-pollination has given rise to new subfields (like biomedical informatics, imaging data science, and computational radiology) and spurred the creation of sophisticated tools ranging from AI-enabled scanners to virtual reality visualization of medical images.
The ripple effect on the industry is significant: companies are racing to build smarter imaging devices and smarter analysis platforms, driving rapid innovation. Moreover, the needs identified in this transformation, such as the demand for greater standardization, security, and interoperability, are informing global efforts to create robust frameworks and infrastructure for the next generation of healthcare technology. We are witnessing investments in things like quantitative imaging centers, open datasets for AI training, and cloud-based health information exchanges, all of which owe at least part of their momentum to the progress in digital medical imaging. Crucially, this transformation also prompts a reflection on the human element in medicine. We conclude that technology is most powerful when it complements healthcare professionals rather than replaces them. The thesis of this discussion reinforces that while algorithms can crunch numbers and recognize patterns at superhuman speed, it is the clinicians who provide context, empathic judgment, and holistic decision-making. The future of medical imaging will likely be a model of augmented intelligence: radiologists and AI working in concert, each compensating for the other's limitations. Ensuring that doctors are trained to use these tools effectively, and that patients trust the combined expertise of human and machine, will be a priority in the coming years.

In conclusion, the digital transformation of medical imaging is far more than a technical upgrade of scanners and software; it is a paradigm shift that is influencing the entire healthcare continuum. It enables a cycle of continuous improvement: the more we digitize and analyze, the more we learn, and the more we can improve subsequent care. The thesis presented here ties together the threads of technology, clinical practice, benefits, and challenges to provide a holistic view of this landscape. Standing at this nexus of medicine and digital innovation, one can foresee a future healthcare system that is smarter, more personalized, and more efficient, a future in which medical imaging plays a formative role not just in diagnosing illness, but in predicting, monitoring, and fundamentally changing the way we manage disease. For medical engineering, this means ongoing opportunities to innovate and refine the tools that make such a future possible. As we move forward, the lessons learned and the foundations laid during this transformative period will guide us in harnessing technology's full potential while keeping patient care and safety at the center. In the grand scope of medical history, the digital transformation of imaging will stand out as a turning point that propelled healthcare into a new era of possibility, combining the precision of machines with the insight of humans to ultimately improve lives.

List of Publications from the Author

Riccardo Forni's list of peer-reviewed publications as main or contributor author in scientific journals or conferences, presented in chronological order from the most recent:

- Forni, Riccardo, Andrea Colacino, Bruna Punzo, Carlo Cavaliere, Monica Franzese, Aevar Orn Ulfarsson, Cristiana Corsi, and Paolo Gargiulo. "Virtual cardiac histology: Towards a radiodensitometric characterization of left ventricular cardiac muscle in healthy and pathological conditions." Computer Methods and Programs in Biomedicine (2025): 108876.
- Forni, Riccardo, Ida Maruotto, Anna Zanuccoli, Riccardo Nicoletti, Luca Trimigno, Matteo Corbellino, Sònia Travé-Huarte, Giuseppe Giannaccare, and Paolo Gargiulo. "Advancing Meibography Assessment and Automated Meibomian Gland Detection Using Gray Value Profiles." Diagnostics 15, no. 10 (2025): 1199.
- Forni, Riccardo, Paolo Gargiulo, Gabriele Boretti, Marco Quadrelli, Tommaso Baccaglini, Aldo Morra, Barbara Ravara et al. "The Impact of Persevering Home Full-Body In-Bed Gym Exercise on Body Muscles in Aging: A Case Report by Quantitative Radio-Densitometric Study Using 3D and 2D Color CT." Diagnostics 14, no. 24 (2024): 2808.
- Forni, Riccardo, Daniela Bruno, Marco Palanca, Luca Cristofolini, and Paolo Gargiulo. "Replicating Healthy and Metastatic Behavior: A Biomechanical Investigation Using 3D Printed Vertebrae Models." In 2024 IEEE International Conference on Metrology for eXtended Reality, Artificial Intelligence and Neural Engineering (MetroXRAINE), pp. 1010-1015. IEEE, 2024.
- Forni, Riccardo, Danilo Calderonel, Damiano Coato, Gianmarco Dolino, Giuseppe Cesarelli, Carlo Ricciardi, Mario Cesarelli, and Paolo Gargiulo. "Towards Bio-Mimetic 3D Printable Human Anatomies." In 2024 IEEE International Conference on Metrology for eXtended Reality, Artificial Intelligence and Neural Engineering (MetroXRAINE), pp. 1016-1021. IEEE, 2024.
- Dolino, Gianmarco, Damiano Coato, Riccardo Forni, Gabriele Boretti, Federica Kiyomi Ciliberti, and Paolo Gargiulo. "Designing a Synthetic 3D-Printed Knee Cartilage: FEA Model, Micro-Structure and Mechanical Characteristics." Applied Sciences 14, no. 1 (2023): 331.
- Ciliberti, Federica Kiyomi, Riccardo Forni, Damiano Coato, Gianmarco Dolino, Lorena Guerrini, Vincenzo Minutolo, and Paolo Gargiulo. "Development of synthetic 3D printed knee joint to assess mechanical and functional properties of degenerative cartilage." In 2023 IEEE International

Conference on Metrology for eXtended Reality, Artificial Intelligence and Neural Engineering (MetroXRAINE), pp. 628-633. IEEE, 2023.

- Forni, Riccardo, Giacomo Pavan, Arnar Gunnarsson, Carlo Ricciardi, Cristiana Corsi, and Paolo Gargiulo. "Advanced 3d printing of patient-specific human heart for improved surgical planning." In 2023 IEEE International Conference on Metrology for eXtended Reality, Artificial Intelligence and Neural Engineering (MetroXRAINE), pp. 473-478. IEEE, 2023.
- Forni, Riccardo, Carmine Gelormini, Cristiana Corsi, and Paolo Gargiulo. "Virtual Histology of the Heart Through CT Imaging: Preliminary Results of a Novel Noninvasive Approach for Cardiac Tissue Characterization." In 2023 Computing in Cardiology (CinC), vol. 50, pp. 1-4. IEEE, 2023.
- Recenti, Marco, Deborah Jacob, Romain Aubonnet, Bérangère Burgunder, Itziar Mengual i Escalona, Arnar Evgení Gunnarsson, Federica Kiyomi Ciliberti et al. "Predicting lifestyle using BioVRSea multi-biometric paradigms." In 2022 IEEE International Conference on Metrology for Extended Reality, Artificial Intelligence and Neural Engineering (MetroXRAINE), pp. 329-334. IEEE, 2022.
- Gunnarsson, Arnar Evgení, Federica Kiyomi Ciliberti, Chiara Belfiori, Alessia Lindemann, Riccardo Forni, Halldór Jónsson, and Paolo Gargiulo. "Assessment of Femoral Cartilage Morphological and Topological Features Using Machine Learning." In 2022 IEEE International Conference on Metrology for Extended Reality, Artificial Intelligence and Neural Engineering (MetroXRAINE), pp. 277-282. IEEE, 2022.
- Ciliberti, Federica Kiyomi, Giuseppe Cesarelli, Lorena Guerrini, Arnar Evgeni Gunnarsson, Riccardo Forni, Romain Aubonnet, Marco Recenti et al. "The role of bone mineral density and cartilage volume to predict knee cartilage degeneration." European Journal of Translational Myology 32, no. 2 (2022): 10678.

Bibliography

[1] W. C. Röntgen, "On a new kind of rays", *Science*, vol. 3, no. 59, pp. 227–231, 1896.

[2] G. N. Hounsfield, "Computerized transverse axial scanning (tomography): Part 1. description of system", *The British journal of radiology*, vol. 46, no. 552, pp. 1016–1022, 1973.

[3] A. M. Cormack, "Representation of a function by its line integrals, with some radiological applications", *Journal of applied physics*, vol. 34, no. 9, pp. 2722–2727, 1963.

[4] M. A. Flower, *Webb's physics of medical imaging*. CRC press, 2012.

[5] D. F. Jackson and D. J. Hawkes, "X-ray attenuation coefficients of elements and mixtures", *Physics Reports*, vol. 70, no. 3, pp. 169–233, 1981.

[6] S. R. Cherry, J. A. Sorenson, and M. E. Phelps, *Physics in nuclear medicine*. Saunders, 2013.

[7] Y. F. Tai and P. Piccini, "Applications of positron emission tomography (pet) in neurology", *Journal of Neurology, Neurosurgery & Psychiatry*, vol. 75, no. 5, pp. 669–676, 2004.

[8] E. M. Rohren, T. G. Turkington, and R. E. Coleman, "Clinical applications of pet in oncology", *Radiology*, vol. 231, no. 2, pp. 305–332, 2004.

[9] M. T. Vlaardingerbroek and J. A. Boer, *Magnetic resonance imaging: theory and practice*. Springer Science & Business Media, 2013.

[10] G. H. Glover, "Overview of functional magnetic resonance imaging", *Neurosurgery Clinics of North America*, vol. 22, no. 2, p. 133, 2011.

[11] J. A. Jensen, "Medical ultrasound imaging", *Progress in biophysics and molecular biology*, vol. 93, no. 1-3, pp. 153–165, 2007.

[12] P. N. Wells, "Ultrasound imaging", *Physics in medicine & biology*, vol. 51, no. 13, R83, 2006.

[13] R. A. NISHIMURA, F. A. MILLER Jr, M. J. CALLAHAN, R. C. BENASSI, J. B. SEWARD, and A. J. TAJIK, "Doppler echocardiography: Theory, instrumentation, technique, and application", in *Mayo Clinic Proceedings*, Elsevier, vol. 60, 1985, pp. 321–343.

[14] E. Ring and K. Ammer, "Infrared thermal imaging in medicine", *Physiological measurement*, vol. 33, no. 3, R33, 2012.

[15] B. B. Lahiri, S. Bagavathiappan, T. Jayakumar, and J. Philip, "Medical applications of infrared thermography: A review", *Infrared physics & technology*, vol. 55, no. 4, pp. 221–235, 2012.

[16] J. T. Bushberg and J. M. Boone, *The essential physics of medical imaging*. Lippincott Williams & Wilkins, 2011.

[17] M. Spahn, "X-ray detectors in medical imaging", *Nuclear Instruments and Methods in Physics Research Section A: Accelerators, Spectrometers, Detectors and Associated Equipment*, vol. 731, pp. 57–63, 2013.

[18] M. K. Kalra, M. M. Maher, T. L. Toth, *et al.*, "Strategies for ct radiation dose optimization", *Radiology*, vol. 230, no. 3, pp. 619–628, 2004.

[19] R. W. Brown, Y.-C. N. Cheng, E. M. Haacke, M. R. Thompson, and R. Venkatesan, *Magnetic resonance imaging: physical principles and sequence design*. John Wiley & Sons, 2014.

[20] D. W. McRobbie, E. A. Moore, M. J. Graves, and M. R. Prince, *MRI from Picture to Proton*. Cambridge university press, 2017.

[21] T. L. Szabo, *Diagnostic ultrasound imaging: inside out*. Academic press, 2013.

[22] W. D. Bidgood Jr, S. C. Horii, F. W. Prior, and D. E. Van Syckle, "Understanding and using dicom, the data interchange standard for biomedical imaging", *Journal of the American Medical Informatics Association*, vol. 4, no. 3, pp. 199–212, 1997.

[23] R. V. Dandu, "Storage media for computers in radiology", *Indian Journal of Radiology and Imaging*, vol. 18, no. 04, pp. 287–289, 2008.

[24] M. Mustra, K. Delac, and M. Grgic, "Overview of the dicom standard", in *2008 50th international symposium ELMAR*, IEEE, vol. 1, 2008, pp. 39–44.

[25] G. N. Hounsfield, "Computed medical imaging", *Science*, vol. 210, no. 4465, pp. 22–28, 1980.

[26] J. A. Thie, "Understanding the standardized uptake value, its methods, and implications for usage", *Journal of Nuclear Medicine*, vol. 45, no. 9, pp. 1431–1434, 2004.

[27] C. E. Kahn, J. A. Carrino, M. J. Flynn, D. J. Peck, and S. C. Horii, "Dicom and radiology: Past, present, and future", *Journal of the American College of Radiology*, vol. 4, no. 9, pp. 652–657, 2007.

[28] H. K. Huang, *PACS and imaging informatics: basic principles and applications*. John Wiley & Sons, 2011.

[29] I. Bankman, *Handbook of medical image processing and analysis*. Elsevier, 2008.

[30] R. Adams and L. Bischof, "Seeded region growing", *IEEE Transactions on pattern analysis and machine intelligence*, vol. 16, no. 6, pp. 641–647, 1994.

[31] L. Vincent and P. Soille, "Watersheds in digital spaces: An efficient algorithm based on immersion simulations", *IEEE Transactions on Pattern Analysis & Machine Intelligence*, vol. 13, no. 06, pp. 583–598, 1991.

[32] M. B. Dillencourt, H. Samet, and M. Tamminen, "A general approach to connected-component labeling for arbitrary image representations", *Journal of the ACM (JACM)*, vol. 39, no. 2, pp. 253–280, 1992.

[33] K. Krishna and M. N. Murty, "Genetic k-means algorithm", *IEEE Transactions on Systems, Man, and Cybernetics, Part B (Cybernetics)*, vol. 29, no. 3, pp. 433–439, 1999.

[34] Y. Cheng, "Mean shift, mode seeking, and clustering", *IEEE transactions on pattern analysis and machine intelligence*, vol. 17, no. 8, pp. 790–799, 1995.

[35] Y.-J. Zhang, "A survey on evaluation methods for image segmentation", *Pattern recognition*, vol. 29, no. 8, pp. 1335–1346, 1996.

[36] W. M. Wells, W. E. L. Grimson, R. Kikinis, and F. A. Jolesz, "Adaptive segmentation of mri data", *IEEE transactions on medical imaging*, vol. 15, no. 4, pp. 429–442, 1996.

[37] R. Malladi, J. A. Sethian, and B. C. Vemuri, "Shape modeling with front propagation: A level set approach", *IEEE transactions on pattern analysis and machine intelligence*, vol. 17, no. 2, pp. 158–175, 2002.

[38] L. A. Vese and T. F. Chan, "A multiphase level set framework for image segmentation using the mumford and shah model", *International journal of computer vision*, vol. 50, pp. 271–293, 2002.

[39] S. Z. Li, *Markov random field modeling in image analysis*. Springer Science & Business Media, 2009.

[40] Y. Boykov and G. Funka-Lea, "Graph cuts and efficient nd image segmentation", *International journal of computer vision*, vol. 70, no. 2, pp. 109–131, 2006.

[41] S. Minaee, Y. Boykov, F. Porikli, A. Plaza, N. Kehtarnavaz, and D. Terzopoulos, "Image segmentation using deep learning: A survey", *IEEE transactions on pattern analysis and machine intelligence*, vol. 44, no. 7, pp. 3523–3542, 2021.

[42] O. Ronneberger, P. Fischer, and T. Brox, "U-net: Convolutional networks for biomedical image segmentation", in *Medical image computing and computer-assisted intervention–MICCAI 2015: 18th international conference, Munich, Germany, October 5-9, 2015, proceedings, part III 18*, Springer, 2015, pp. 234–241.

[43] N. Siddique, S. Paheding, C. P. Elkin, and V. Devabhaktuni, "U-net and its variants for medical image segmentation: A review of theory and applications", *IEEE access*, vol. 9, pp. 82 031–82 057, 2021.

[44] R. J. Gillies, P. E. Kinahan, and H. Hricak, "Radiomics: Images are more than pictures, they are data", *Radiology*, vol. 278, no. 2, pp. 563–577, 2016. DOI: 10.1148/radiol.2015151169.

[45] C. G. Peterfy, A. Guermazi, S. Zaim, *et al.*, "Whole-organ magnetic resonance imaging score (worms) of the knee in osteoarthritis", *Osteoarthritis and Cartilage*, vol. 12, no. 3, pp. 177–190, 2004. DOI: 10.1016/j.joca.2003.12.005.

[46] P. Lambin, E. Rios-Velazquez, R. Leijenaar, *et al.*, "Radiomics: Extracting more information from medical images using advanced feature analysis", *European Journal of Cancer*, vol. 48, no. 4, pp. 441–446, 2012. DOI: 10.1016/j.ejca.2011.11.036.

[47] R. Thawani, M. McLane, N. Beig, *et al.*, "Radiomics and radiogenomics in lung cancer: A review for the clinician", *Lung cancer*, vol. 115, pp. 34–41, 2018.

[48] H. J. Aerts, E. R. Velazquez, R. T. Leijenaar, *et al.*, "Decoding tumour phenotype by noninvasive imaging using a quantitative radiomics approach", *Nature communications*, vol. 5, no. 1, p. 4006, 2014.

[49] Y. Sun, H. M. Reynolds, B. Parameswaran, *et al.*, "Multiparametric mri and radiomics in prostate cancer: A review", *Australasian physical & engineering sciences in medicine*, vol. 42, pp. 3–25, 2019.

[50] P. Kickingereder, D. Bonekamp, M. Nowosielski, *et al.*, "Radiogenomics of glioblastoma: Machine learning–based classification of molecular characteristics by using multiparametric and multiregional mr imaging features", *Radiology*, vol. 281, no. 3, pp. 907–918, 2016.

[51] I. Cetin, Z. Raisi-Estabragh, S. E. Petersen, *et al.*, "Radiomics signatures of cardiovascular risk factors in cardiac mri: Results from the uk biobank", *Frontiers in Cardiovascular Medicine*, vol. 7, p. 591 368, 2020.

[52] M. Marwan, S. Koenig, K. Schreiber, *et al.*, "Quantification of epicardial adipose tissue by cardiac ct: Influence of acquisition parameters and contrast enhancement", *European journal of radiology*, vol. 121, p. 108 732, 2019.

[53] J. C. Moon, D. R. Messroghli, P. Kellman, *et al.*, "Myocardial t1 mapping and extracellular volume quantification: A society for cardiovascular magnetic resonance (scmr) and cmr working group of the european society of cardiology consensus statement", *Journal of Cardiovascular Magnetic Resonance*, vol. 15, no. 1, p. 92, 2013.

[54] K. Engelke, T. Lang, S. Khosla, *et al.*, "Clinical use of quantitative computed tomography (qct) of the hip in the management of osteoporosis in adults: The 2015 iscd official positions—part i", *Journal of clinical densitometry*, vol. 18, no. 3, pp. 338–358, 2015.

[55] J. Ashburner and K. J. Friston, "Voxel-based morphometry—the methods", *Neuroimage*, vol. 11, no. 6, pp. 805–821, 2000. DOI: 10.1006/nimg.2000.0582.

[56] P. Ravanfar, S. M. Loi, W. T. Syeda, *et al.*, "Systematic review: Quantitative susceptibility mapping (qsm) of brain iron profile in neurodegenerative diseases", *Frontiers in neuroscience*, vol. 15, p. 618 435, 2021.

[57] A. Zwanenburg, M. Vallières, M. A. Abdalah, and et al., "The image biomarker standardization initiative: Standardized quantitative radiomics for high-throughput image-based phenotyping", *Radiology*, vol. 295, no. 2, pp. 328–338, 2020. DOI: 10.1148/radiol.2020191145.

[58] G. Litjens, T. Kooi, B. E. Bejnordi, *et al.*, "A survey on deep learning in medical image analysis", *Medical image analysis*, vol. 42, pp. 60–88, 2017.

[59] B. J. Erickson, P. Korfiatis, Z. Akkus, and T. L. Kline, "Machine learning for medical imaging", *radiographics*, vol. 37, no. 2, pp. 505–515, 2017.

[60] A. Hosny, C. Parmar, J. Quackenbush, L. H. Schwartz, and H. J. Aerts, "Artificial intelligence in radiology", *Nature Reviews Cancer*, vol. 18, no. 8, pp. 500–510, 2018.

[61] N. Hampe, S. G. van Velzen, J.-P. Aben, C. Collet, and I. Išgum, "Deep learning-based prediction of fractional flow reserve along the coronary artery", *arXiv preprint arXiv:2308.04923*, 2023.

[62] A. Esteva, A. Robicquet, B. Ramsundar, *et al.*, "A guide to deep learning in healthcare", *Nature medicine*, vol. 25, no. 1, pp. 24–29, 2019.

[63] F. Cabitza, A. Campagner, F. Soares, *et al.*, "The importance of being external. methodological insights for the external validation of machine learning models in medicine", *Computer methods and programs in biomedicine*, vol. 208, p. 106 288, 2021.

[64] U. Mezger, C. Jendrewski, and M. Bartels, "Navigation in surgery", *Langenbeck's archives of surgery*, vol. 398, pp. 501–514, 2013.

[65] D. Guha, N. M. Alotaibi, N. Nguyen, S. Gupta, C. McFaul, and V. X. Yang, "Augmented reality in neurosurgery: A review of current concepts and emerging applications", *Canadian Journal of Neurological Sciences*, vol. 44, no. 3, pp. 235–245, 2017.

[66] F. A. Jolesz, *Intraoperative imaging and image-guided therapy*. Springer Science & Business Media, 2014.

[67] N. J. Mankovich, D. Samson, W. Pratt, D. Lew, and J. Beumer III, "Surgical planning using three-dimensional imaging and computer modeling", *Otolaryngologic Clinics of North America*, vol. 27, no. 5, pp. 875–889, 1994.

[68] F. Galbusera, A. Cina, M. Panico, D. Albano, and C. Messina, "Image-based biomechanical models of the musculoskeletal system", *European radiology experimental*, vol. 4, no. 1, p. 49, 2020.

[69] A. Krishnamurthy, C. T. Villongco, J. Chuang, *et al.*, "Patient-specific models of cardiac biomechanics", *Journal of computational physics*, vol. 244, pp. 4–21, 2013.

[70] C. M. Augustin, A. Crozier, A. Neic, *et al.*, "Patient-specific modeling of left ventricular electromechanics as a driver for haemodynamic analysis", *EP Europace*, vol. 18, no. suppl_4, pp. iv121–iv129, 2016.

[71] S. Barteit, L. Lanfermann, T. Bärnighausen, F. Neuhann, C. Beiersmann, *et al.*, "Augmented, mixed, and virtual reality-based head-mounted devices for medical education: Systematic review", *JMIR serious games*, vol. 9, no. 3, e29080, 2021.

[72] P. Gargiulo, *Handbook of Surgical Planning and 3D Printing: Applications, Integration, and New Directions*. Elsevier, 2023.

[73] G. Litjens, C. I. Sánchez, N. Timofeeva, *et al.*, "Deep learning as a tool for increased accuracy and efficiency of histopathological diagnosis", *Scientific reports*, vol. 6, no. 1, p. 26 286, 2016.

[74] D. Komura and S. Ishikawa, "Machine learning methods for histopathological image analysis", *Computational and structural biotechnology journal*, vol. 16, pp. 34–42, 2018.

[75] V. Brancato, C. Cavaliere, N. Garbino, F. Isgrò, M. Salvatore, and M. Aiello, "The relationship between radiomics and pathomics in glioblastoma patients: Preliminary results from a cross-scale association study", *Frontiers in Oncology*, vol. 12, p. 1 005 805, 2022.

[76] L. Feng, Z. Liu, C. Li, *et al.*, "Development and validation of a radiopathomics model to predict pathological complete response to neoadjuvant chemoradiotherapy in locally advanced rectal cancer: A multicentre observational study", *The Lancet Digital Health*, vol. 4, no. 1, e8–e17, 2022.

[77] M. A. Kadir, "Role of telemedicine in healthcare during covid-19 pandemic in developing countries", *Telehealth and Medicine Today*, vol. 5, no. 2, 2020.

[78] R. S. Weinstein, A. R. Graham, L. C. Richter, *et al.*, "Overview of telepathology, virtual microscopy, and whole slide imaging: Prospects for the future", *Human pathology*, vol. 40, no. 8, pp. 1057–1069, 2009.

[79] J. M. Chatterjee and R. Sujatha, "Transforming healthcare: The synergy of telemedicine, telehealth, and artificial intelligence", in *Role of Artificial Intelligence, Telehealth, and Telemedicine in Medical Virology*, Springer, 2025, pp. 1–29.

[80] K. Bruynseels, F. Santoni de Sio, and J. van den Hoven, "Digital twins in health care: Ethical implications of an emerging engineering paradigm", *Frontiers in Genetics*, vol. 9, p. 31, 2018. DOI: 10.3389/fgene.2018.00031.

[81] E. Katsoulakis, Q. Wang, H. Wu, *et al.*, "Digital twins for health: A scoping review", *NPJ digital medicine*, vol. 7, no. 1, p. 77, 2024.

[82] J. Corral-Acero, F. Margara, M. Marciniak, *et al.*, "The 'digital twin' to enable the vision of precision cardiology", *European Heart Journal*, vol. 41, no. 48, pp. 4556–4564, 2020. DOI: 10.1093/eurheartj/ehaa159.

[83] M. Viceconti, A. Henney, and E. Morley-Fletcher, "In silico clinical trials: How computer simulation will transform the biomedical industry", *International Journal of Clinical Trials*, vol. 3, no. 2, pp. 37–46, 2016.

[84] M. J. Cluitmans, G. Plank, and J. Heijman, "Digital twins for cardiac electrophysiology: State of the art and future challenges", *Herzschrittmachertherapie+ Elektrophysiologie*, vol. 35, no. 2, pp. 118–123, 2024.

[85] C. Wu, G. Lorenzo, D. A. Hormuth, *et al.*, "Integrating mechanism-based modeling with biomedical imaging to build practical digital twins for clinical oncology", *Biophysics reviews*, vol. 3, no. 2, 2022.

[86] I. Voigt, H. Inojosa, A. Dillenseger, R. Haase, K. Akgün, and T. Ziemssen, "Digital twins for multiple sclerosis", *Frontiers in immunology*, vol. 12, p. 669 811, 2021.

[87] J. E. Morley, A. M. Abbatecola, J. M. Argiles, *et al.*, "Sarcopenia with limited mobility: An international consensus", *Journal of the American Medical Directors Association*, vol. 12, no. 6, pp. 403–409, 2011.

[88] D. J. Wilkinson, M. Piasecki, and P. Atherton, "The age-related loss of skeletal muscle mass and function: Measurement and physiology of muscle fibre atrophy and muscle fibre loss in humans", *Ageing research reviews*, vol. 47, pp. 123–132, 2018.

[89] A. J. Cruz-Jentoft and A. A. Sayer, "Sarcopenia", *The Lancet*, vol. 393, no. 10191, pp. 2636–2646, 2019.

[90] S. K. Papadopoulou, "Sarcopenia: A contemporary health problem among older adult populations", *Nutrients*, vol. 12, no. 5, p. 1293, 2020.

[91] G. Guglielmi, F. Ponti, M. Agostini, M. Amadori, G. Battista, and A. Bazzocchi, "The role of dxa in sarcopenia", *Aging clinical and experimental research*, vol. 28, pp. 1047–1060, 2016.

[92] J. A. Shepherd, B. K. Ng, M. J. Sommer, and S. B. Heymsfield, "Body composition by dxa", *Bone*, vol. 104, pp. 101–105, 2017.

[93] O. Di Vincenzo, M. Marra, A. Di Gregorio, F. Pasanisi, and L. Scalfi, "Bioelectrical impedance analysis (bia)-derived phase angle in sarcopenia: A systematic review", *Clinical Nutrition*, vol. 40, no. 5, pp. 3052–3061, 2021.

[94] D. Albano, C. Messina, J. Vitale, and L. M. Sconfienza, "Imaging of sarcopenia: Old evidence and new insights", *European radiology*, vol. 30, pp. 2199–2208, 2020.

[95] S. Wang, H. Xie, Y. Gong, *et al.*, "The value of l3 skeletal muscle index in evaluating preoperative nutritional risk and long-term prognosis in colorectal cancer patients", *Scientific Reports*, vol. 10, no. 1, p. 8153, 2020.

[96] Y. Jin, X. Ma, Z. Yang, and N. Zhang, "Low l3 skeletal muscle index associated with the clinicopathological characteristics and prognosis of ovarian cancer: A meta-analysis", *Journal of cachexia, sarcopenia and muscle*, vol. 14, no. 2, pp. 697–705, 2023.

[97] K. Edmunds, M. Gíslason, S. Sigurðsson, *et al.*, "Advanced quantitative methods in correlating sarcopenic muscle degeneration with lower extremity function biometrics and comorbidities", *PloS one*, vol. 13, no. 3, e0193241, 2018.

[98] J. L. Sánchez-Sánchez, L. He, J. S. Morales, *et al.*, "Association of physical behaviours with sarcopenia in older adults: A systematic review and meta-analysis of observational studies", *The Lancet Healthy Longevity*, vol. 5, no. 2, e108–e119, 2024.

[99] *Who global status report on physical activity 2022. available online:* accessed on 25 October 2024). [Online]. Available: `http://www.who.int/publications/i/item/9789240059153`.

[100] C. Ricciardi, K. J. Edmunds, M. Recenti, *et al.*, "Assessing cardiovascular risks from a mid-thigh ct image: A tree-based machine learning approach using radiodensitometric distributions", *Scientific reports*, vol. 10, no. 1, p. 2863, 2020.

[101] M. C. Maccarone, A. Caregnato, G. Regazzo, *et al.*, "Effects of the full-body in-bed gym program on quality of life, pain and risk of sarcopenia in elderly sedentary individuals: Preliminary positive results of a padua prospective observational study", *European Journal of Translational Myology*, vol. 33, no. 3, p. 11 780, 2023.

[102] M. Quadrelli, T. Baccaglini, and A. Morra, "Quantitative 3d-ct imaging of sarcopenia mitigation in the elderly: Evidence from a case report", *European Journal of Translational Myology*, vol. 34, no. 2, p. 12 715, 2024.

[103] U. Carraro, M. S. Alberty, S. Anton, *et al.*, "State of art of mobility medicine: Some more abstracts and evidence that the success of pdm3 is based on extra-session relationships", *European Journal of Translational Myology*, vol. 34, no. 1, p. 12 492, 2024.

[104] C. Ziebart, J. MacDermid, D. Bryant, M. Szekeres, and N. Suh, "Hands up program: Results of a feasibility study of a randomized controlled trial of a bone health exercise and education program for adults aged 50–65 post distal radius fracture", *PloS one*, vol. 19, no. 11, e0313013, 2024.

[105] F. Qi, M. A. Nitsche, X. Ren, D. Wang, and L. Wang, "Top-down and bottom-up stimulation techniques combined with action observation treatment in stroke rehabilitation: A perspective", *Frontiers in neurology*, vol. 14, p. 1 156 987, 2023.

[106] H. Chaabene, O. Prieske, M. Herz, *et al.*, "Home-based exercise programmes improve physical fitness of healthy older adults: A prisma-compliant systematic review and meta-analysis with relevance for covid-19", *Ageing research reviews*, vol. 67, p. 101 265, 2021.

[107] R. Danielsen, G. Thorgeirsson, H. Einarsson, *et al.*, "Prevalence of heart failure in the elderly and future projections: The ages-reykjavík study", *Scandinavian Cardiovascular Journal*, vol. 51, no. 4, pp. 183–189, 2017.

[108] K. J. Edmunds, O. C. Okonkwo, S. Sigurdsson, *et al.*, "Soft tissue radiodensity parameters mediate the relationship between self-reported physical activity and lower extremity function in ages-reykjavík participants", *Scientific Reports*, vol. 11, no. 1, p. 20 173, 2021.

[109] K. Edmunds, M. Gíslason, S. Sigurðsson, *et al.*, "Advanced quantitative methods in correlating sarcopenic muscle degeneration with lower extremity function biometrics and comorbidities", *PloS one*, vol. 13, no. 3, e0193241, 2018.

[110] D. Gallagher, P. Kuznia, S. Heshka, *et al.*, "Adipose tissue in muscle: A novel depot similar in size to visceral adipose tissue2", *The American journal of clinical nutrition*, vol. 81, no. 4, pp. 903–910, 2005.

[111] M. Zamboni, G. Mazzali, F. Fantin, A. Rossi, and V. Di Francesco, "Sarcopenic obesity: A new category of obesity in the elderly", *Nutrition, metabolism and cardiovascular diseases*, vol. 18, no. 5, pp. 388–395, 2008.

[112] J. Aubrey, N. Esfandiari, V. E. Baracos, *et al.*, "Measurement of skeletal muscle radiation attenuation and basis of its biological variation", *Acta physiologica*, vol. 210, no. 3, pp. 489–497, 2014.

[113] U. Carraro, K. J. Edmunds, and P. Gargiulo, "3d false color computed tomography for diagnosis and follow-up of permanent denervated human muscles submitted to home-based functional electrical stimulation", *European Journal of Translational Myology*, vol. 25, no. 2, p. 5133, 2015.

[114] F. Buckinx, J.-Y. Reginster, N. Dardenne, *et al.*, "Concordance between muscle mass assessed by bioelectrical impedance analysis and by dual energy x-ray absorptiometry: A cross-sectional study", *BMC musculoskeletal disorders*, vol. 16, pp. 1–7, 2015.

[115] R. D. Boutin, L. Yao, R. J. Canter, and L. Lenchik, "Sarcopenia: Current concepts and imaging implications", *American Journal of Roentgenology*, vol. 205, no. 3, W255–W266, 2015.

[116] P. Reeves, K. Edmunds, C. Levi, *et al.*, "Cost-effectiveness of targeted thrombolytic therapy for stroke patients using multi-modal ct compared to usual practice", *PLoS One*, vol. 13, no. 10, e0206203, 2018.

[117] A. J. Cruz-Jentoft, G. Bahat, J. Bauer, *et al.*, "Sarcopenia: Revised european consensus on definition and diagnosis", *Age and ageing*, vol. 48, no. 1, pp. 16–31, 2019.

[118] M. Recenti, C. Ricciardi, K. J. Edmunds, *et al.*, "Healthy aging within an image: Using muscle radiodensitometry and lifestyle factors to predict diabetes and hypertension", *IEEE Journal of Biomedical and Health Informatics*, vol. 25, no. 6, pp. 2103–2112, 2020.

[119] H. Oba, Y. Matsui, H. Arai, *et al.*, "Evaluation of muscle quality and quantity for the assessment of sarcopenia using mid-thigh computed tomography: A cohort study", *BMC geriatrics*, vol. 21, pp. 1–8, 2021.

[120] Y. W. Jung, N. Hong, J. C. Na, W. K. Han, and Y. Rhee, "Computed tomography-derived skeletal muscle radiodensity is an early, sensitive marker of age-related musculoskeletal changes in healthy adults", *Endocrinology and Metabolism*, vol. 36, no. 6, pp. 1201–1210, 2021.

[121] S. B. Heymsfield, M. Adamek, M. C. Gonzalez, G. Jia, and D. M. Thomas, "Assessing skeletal muscle mass: Historical overview and state of the art", *Journal of cachexia, sarcopenia and muscle*, vol. 5, pp. 9–18, 2014.

[122] C. M. Prado, J. R. Lieffers, L. J. McCargar, *et al.*, "Prevalence and clinical implications of sarcopenic obesity in patients with solid tumours of the respiratory and gastrointestinal tracts: A population-based study", *The lancet oncology*, vol. 9, no. 7, pp. 629–635, 2008.

[123] S. Mortellaro, S. Triggiani, F. Mascaretti, *et al.*, "Quantitative and qualitative radiological assessment of sarcopenia and cachexia in cancer patients: A systematic review", *Journal of personalized medicine*, vol. 14, no. 3, p. 243, 2024.

[124] J. Lexell, C. C. Taylor, and M. Sjöström, "What is the cause of the ageing atrophy?: Total number, size and proportion of different fiber types studied in whole vastus lateralis muscle from 15-to 83-year-old men", *Journal of the neurological sciences*, vol. 84, no. 2-3, pp. 275–294, 1988.

[125] T. J. Doherty, A. A. Vandervoort, and W. F. Brown, "Effects of ageing on the motor unit: A brief review", *Canadian journal of applied physiology*, vol. 18, no. 4, pp. 331–358, 1993.

[126] B. F. Grogan, J. R. Hsu, S. T. R. Consortium, *et al.*, "Volumetric muscle loss", *JAAOS-Journal of the American Academy of Orthopaedic Surgeons*, vol. 19, S35–S37, 2011.

[127] G. Sirago, M. A. Pellegrino, R. Bottinelli, M. V. Franchi, and M. V. Narici, "Loss of neuromuscular junction integrity and muscle atrophy in skeletal muscle disuse", *Ageing Research Reviews*, vol. 83, p. 101 810, 2023.

[128] M. A. Minetto, C. Busso, G. Gamerro, P. Lalli, G. Massazza, and M. Invernizzi, "Quantitative assessment of volumetric muscle loss: Dual-energy x-ray absorptiometry and ultrasonography", *Current opinion in pharmacology*, vol. 57, pp. 148–156, 2021.

[129] S. Ciciliot, A. C. Rossi, K. A. Dyar, B. Blaauw, and S. Schiaffino, "Muscle type and fiber type specificity in muscle wasting", *The international journal of biochemistry & cell biology*, vol. 45, no. 10, pp. 2191–2199, 2013.

[130] W. J. Evans and J. Lexell, "Human aging, muscle mass, and fiber type composition", *The Journals of Gerontology Series A: Biological Sciences and Medical Sciences*, vol. 50, no. Special_Issue, pp. 11–16, 1995.

[131] K. Downing, R. Prisby, V. Varanasi, J. Zhou, Z. Pan, and M. Brotto, "Old and new biomarkers for volumetric muscle loss", *Current opinion in pharmacology*, vol. 59, pp. 61–69, 2021.

[132] B. T. Corona, J. C. Wenke, and C. L. Ward, "Pathophysiology of volumetric muscle loss injury", *Cells Tissues Organs*, vol. 202, no. 3-4, pp. 180–188, 2016.

[133] A. Ticinesi, T. Meschi, M. V. Narici, F. Lauretani, and M. Maggio, "Muscle ultrasound and sarcopenia in older individuals: A clinical perspective", *Journal of the American Medical Directors Association*, vol. 18, no. 4, pp. 290–300, 2017.

[134] B. T. Wall, M. L. Dirks, and L. J. Van Loon, "Skeletal muscle atrophy during short-term disuse: Implications for age-related sarcopenia", *Ageing research reviews*, vol. 12, no. 4, pp. 898–906, 2013.

[135] C. D. Reimers, T. Harder, and H. Saxe, "Age-related muscle atrophy does not affect all muscles and can partly be compensated by physical activity: An ultrasound study", *Journal of the neurological sciences*, vol. 159, no. 1, pp. 60–66, 1998.

[136] D. J. Wilkinson, M. Piasecki, and P. Atherton, "The age-related loss of skeletal muscle mass and function: Measurement and physiology of muscle fibre atrophy and muscle fibre loss in humans", *Ageing research reviews*, vol. 47, pp. 123–132, 2018.

[137] T. Ikezoe, N. Mori, M. Nakamura, and N. Ichihashi, "Age-related muscle atrophy in the lower extremities and daily physical activity in elderly women", *Archives of gerontology and geriatrics*, vol. 53, no. 2, e153–e157, 2011.

[138] C. D. Reimers, G. Knapp, and A. K. Reimers, "Does physical activity increase life expectancy? a review of the literature", *Journal of aging research*, vol. 2012, no. 1, p. 243 958, 2012.

[139] S. Trappe, D. Costill, B. Goodpaster, and D. Pearson, "Calf muscle strength in former elite distance runners", *Scandinavian journal of medicine & science in sports*, vol. 6, no. 4, pp. 205–210, 1996.

[140] H. Klitgaard, M. Mantoni, S. Schiaffino, *et al.*, "Function, morphology and protein expression of ageing skeletal muscle: A cross-sectional study of elderly men with different training backgrounds", *Acta Physiologica Scandinavica*, vol. 140, no. 1, pp. 41–54, 1990.

[141] G. Distefano and G. Bret H, *Effects of exercise and aging on skeletal muscle*, 2018.

[142] L. Allen, J. Williams, N. Townsend, *et al.*, "Socioeconomic status and non-communicable disease behavioural risk factors in low-income and lower-middle-income countries: A systematic review", *The Lancet Global Health*, vol. 5, no. 3, e277–e289, 2017.

[143] C. E. Practice, O. of Care Group, M. Velez, *et al.*, "Factors that influence the provision of home-based rehabilitation services for people needing rehabilitation: A qualitative evidence synthesis", *Cochrane Database of Systematic Reviews*, vol. 2023, no. 2, 1996.

[144] A. Mahmood, P. Nayak, C. English, *et al.*, "Adherence to home exercises and rehabilitation (adhere) after stroke in low-to-middle-income countries: A randomized controlled trial", *Topics in Stroke Rehabilitation*, vol. 29, no. 6, pp. 438–448, 2022.

[145] N. Chaudhary and N. Kreiger, "Nutrition and physical activity interventions for low-income populations", *Canadian Journal of Dietetic Practice and Research*, vol. 68, no. 4, pp. 201–206, 2007.

[146] D. Gothi and J. Joshi, "Pulmonary rehabilitation in resource poor settings", *Indian Journal of Chest Diseases and Allied Sciences*, vol. 53, no. 3, p. 163, 2011.

[147] S. P. Vlachopoulos, "Contextual measurement of sources of exercise amotivation: The revised amotivation toward exercise scale-2", *Journal of Sport and Exercise Psychology*, vol. 46, no. 6, pp. 353–361, 2024.

[148] A.-G. Mittaz Hager, N. Mathieu, C. Lenoble-Hoskovec, J. Swanenburg, R. de Bie, and R. Hilfiker, "Effects of three home-based exercise programmes regarding falls, quality of life and exercise-adherence in older adults at risk of falling: Protocol for a randomized controlled trial", *BMC geriatrics*, vol. 19, pp. 1–11, 2019.

[149] F. Landi, E. Marzetti, A. M. Martone, R. Bernabei, and G. Onder, "Exercise as a remedy for sarcopenia", *Current Opinion in Clinical Nutrition & Metabolic Care*, vol. 17, no. 1, pp. 25–31, 2014.

[150] C. Adjetey, B. Karnon, R. S. Falck, H. Balasubramaniam, K. Buschert, and J. C. Davis, "Cost-effectiveness of exercise versus multimodal interventions that include exercise to prevent falls among community-dwelling older adults: A systematic review and meta-analysis", *Maturitas*, vol. 169, pp. 16–31, 2023.

[151] R. W. Yeh, S. Sidney, M. Chandra, M. Sorel, J. V. Selby, and A. S. Go, "Population trends in the incidence and outcomes of acute myocardial infarction", *New England Journal of Medicine*, vol. 362, no. 23, pp. 2155–2165, 2010.

[152] S. Bhaskar, P. Stanwell, D. Cordato, J. Attia, and C. Levi, "Reperfusion therapy in acute ischemic stroke: Dawn of a new era?", *BMC neurology*, vol. 18, pp. 1–26, 2018.

[153] Y. Hong, W. W. Su, and X. Li, "Risk factors of sudden cardiac death in hypertrophic cardiomyopathy", *Current Opinion in Cardiology*, vol. 37, no. 1, pp. 15–21, 2022.

[154] C. M. Kramer, J. Barkhausen, C. Bucciarelli-Ducci, S. D. Flamm, R. J. Kim, and E. Nagel, "Standardized cardiovascular magnetic resonance imaging (cmr) protocols: 2020 update", *Journal of Cardiovascular Magnetic Resonance*, vol. 22, no. 1, p. 17, 2020.

[155] G. Chery, N. Kamp, A. S. Kosinski, *et al.*, "Prognostic value of myocardial fibrosis on cardiac magnetic resonance imaging in patients with ischemic cardiomyopathy: A systematic review", *American Heart Journal*, vol. 229, pp. 52–60, 2020.

[156] R. O'Hanlon, A. Grasso, M. Roughton, *et al.*, "Prognostic significance of myocardial fibrosis in hypertrophic cardiomyopathy", *Journal of the American College of Cardiology*, vol. 56, no. 11, pp. 867–874, 2010.

[157] B. Ambale-Venkatesh and J. A. Lima, "Cardiac mri: A central prognostic tool in myocardial fibrosis", *Nature reviews cardiology*, vol. 12, no. 1, pp. 18–29, 2015.

[158] U. Hoffmann, M. Ferencik, R. C. Cury, and A. J. Pena, "Coronary ct angiography", *Journal of nuclear medicine*, vol. 47, no. 5, pp. 797–806, 2006.

[159] D. De Stefano, F. Vaccarino, D. Santucci, *et al.*, "Delayed enhancement in cardiac ct: A potential alternative to cardiac mri? technical updates and clinical considerations", *Applied Sciences*, vol. 14, no. 10, p. 4275, 2024.

[160] B. Ruzsics, H. Lee, P. L. Zwerner, M. Gebregziabher, P. Costello, and U. J. Schoepf, "Dual-energy ct of the heart for diagnosing coronary artery stenosis and myocardial ischemia-initial experience", *European radiology*, vol. 18, pp. 2414–2424, 2008.

[161] T. Aikawa, N. Oyama-Manabe, M. Naya, *et al.*, "Delayed contrast-enhanced computed tomography in patients with known or suspected cardiac sarcoidosis: A feasibility study", *European Radiology*, vol. 27, pp. 4054–4063, 2017.

[162] C. Bouleti, G. Baudry, B. Iung, *et al.*, "Usefulness of late iodine enhancement on spectral ct in acute myocarditis", *JACC: Cardiovascular Imaging*, vol. 10, no. 7, pp. 826–827, 2017.

[163] S. Leng, M. Bruesewitz, S. Tao, *et al.*, "Photon-counting detector ct: System design and clinical applications of an emerging technology", *Radiographics*, vol. 39, no. 3, pp. 729–743, 2019.

[164] V. Kumar, Y. Gu, S. Basu, *et al.*, "Radiomics: The process and the challenges", *Magnetic resonance imaging*, vol. 30, no. 9, pp. 1234–1248, 2012.

[165] P. Payot, M. Bickel, and G. Cimasoni, "Longitudinal quantitative radiodensitometric study of treated and untreated lower molar furcation involvements", *Journal of clinical periodontology*, vol. 14, no. 1, pp. 8–18, 1987.

[166] K. J. Edmunds, Í. Árnadóttir, M. K. Gíslason, U. Carraro, and P. Gargiulo, "Nonlinear trimodal regression analysis of radiodensitometric distributions to quantify sarcopenic and sequelae muscle degeneration", *Computational and Mathematical Methods in Medicine*, vol. 2016, 2016.

[167] F. Y. Yap, B. A. Varghese, S. Y. Cen, *et al.*, "Shape and texture-based radiomics signature on ct effectively discriminates benign from malignant renal masses", *European radiology*, vol. 31, pp. 1011–1021, 2021.

[168] I. Ayx, H. Tharmaseelan, A. Hertel, *et al.*, "Myocardial radiomics texture features associated with increased coronary calcium score—first results of a photon-counting ct", *Diagnostics*, vol. 12, no. 7, p. 1663, 2022.

[169] B.-H. Chen, D.-A. An, J. He, *et al.*, "Myocardial extracellular volume fraction radiomics analysis for differentiation of reversible versus irreversible myocardial damage and prediction of left ventricular adverse remodeling after st-elevation myocardial infarction", *European Radiology*, vol. 31, pp. 504–514, 2021.

[170] A. Chaddad, P. Daniel, and T. Niazi, "Radiomics evaluation of histological heterogeneity using multiscale textures derived from 3d wavelet transformation of multispectral images", *Frontiers in oncology*, vol. 8, p. 96, 2018.

[171] T. Polidori, D. De Santis, C. Rucci, *et al.*, "Radiomics applications in cardiac imaging: A comprehensive review", *La radiologia medica*, vol. 128, no. 8, pp. 922–933, 2023.

[172] L. Qin, C. Chen, S. Gu, *et al.*, "A radiomic approach to predict myocardial fibrosis on coronary ct angiography in hypertrophic cardiomyopathy", *International Journal of Cardiology*, vol. 337, pp. 113–118, 2021.

[173] F. Denzinger, M. Wels, N. Ravikumar, *et al.*, "Coronary artery plaque characterization from ccta scans using deep learning and radiomics", in *Medical Image Computing and Computer Assisted Intervention–MICCAI 2019: 22nd International Conference, Shenzhen, China, October 13–17, 2019, Proceedings, Part IV 22*, Springer, 2019, pp. 593–601.

[174] Z.-Y. Shu, S.-J. Cui, Y.-Q. Zhang, *et al.*, "Predicting chronic myocardial ischemia using ccta-based radiomics machine learning nomogram", *Journal of Nuclear Cardiology*, vol. 29, no. 1, pp. 262–274, 2022.

[175] W. Hu, X. Wu, D. Dong, *et al.*, "Novel radiomics features from ccta images for the functional evaluation of significant ischaemic lesions based on the coronary fractional flow reserve score", *The International Journal of Cardiovascular Imaging*, vol. 36, pp. 2039–2050, 2020.

[176] C. Parmar, P. Grossmann, J. Bussink, P. Lambin, and H. J. Aerts, "Machine learning methods for quantitative radiomic biomarkers", *Scientific reports*, vol. 5, no. 1, p. 13 087, 2015.

[177] L. H. T. Lam, N. T. Chu, T.-O. Tran, D. T. Do, and N. Q. K. Le, "A radiomics-based machine learning model for prediction of tumor mutational burden in lower-grade gliomas", *Cancers*, vol. 14, no. 14, p. 3492, 2022.

[178] W. Wang, R. Sheng, S. Liao, *et al.*, "Lightgbm is an effective predictive model for postoperative complications in gastric cancer: A study integrating radiomics with ensemble learning", *Journal of Imaging Informatics in Medicine*, vol. 37, no. 6, pp. 3034–3048, 2024.

[179] A. Aıdoud, W. Gana, F. Poitau, *et al.*, "High prevalence of geriatric conditions among older adults with cardiovascular disease", *Journal of the American Heart Association*, e026850, 2023.

[180] E. O. Kharbanda, "Epidemiology of hypertension and cardiovascular disease in children and adolescents", *Pediatric Hypertension*, p. 367, 2023.

[181] M. Recenti, C. Ricciardi, K. J. Edmunds, *et al.*, "Healthy aging within an image: Using muscle radiodensitometry and lifestyle factors to predict diabetes and hypertension", *IEEE Journal of Biomedical and Health Informatics*, vol. 25, no. 6, pp. 2103–2112, 2020.

[182] C. Ricciardi, K. J. Edmunds, M. Recenti, *et al.*, "Assessing cardiovascular risks from a mid-thigh ct image: A tree-based machine learning approach using radiodensitometric distributions", *Scientific reports*, vol. 10, no. 1, p. 2863, 2020.

[183] M. Marwan and S. Achenbach, "Quantification of epicardial fat by computed tomography: Why, when and how?", *Journal of cardiovascular computed tomography*, vol. 7, no. 1, pp. 3–10, 2013.

[184] M. Mazonakis and J. Damilakis, "Computed tomography: What and how does it measure?", *European journal of radiology*, vol. 85, no. 8, pp. 1499–1504, 2016.

[185] A. F. Zuur, E. N. Ieno, N. J. Walker, A. A. Saveliev, G. M. Smith, *et al.*, *Mixed effects models and extensions in ecology with R*. Springer, 2009, vol. 574.

[186] R. R Core Team *et al.*, "R: A language and environment for statistical computing", 2013.

[187] D. Bates, M. Mächler, B. Bolker, and S. Walker, "Fitting linear mixed-effects models using lme4", *arXiv preprint arXiv:1406.5823*, 2014.

[188] A. Kuznetsova, P. B. Brockhoff, and R. H. Christensen, "Lmertest package: Tests in linear mixed effects models", *Journal of Statistical Software*, vol. 82, pp. 1–26, 2017.

[189] F. Triposkiadis, A. Xanthopoulos, K. D. Boudoulas, G. Giamouzis, H. Boudoulas, and J. Skoularigis, "The interventricular septum: Structure, function, dysfunction, and diseases", *Journal of Clinical Medicine*, vol. 11, no. 11, p. 3227, 2022.

[190] B. J. Maron and M. S. Maron, "Hypertrophic cardiomyopathy", *The Lancet*, vol. 381, no. 9862, pp. 242–255, 2013.

[191] L. J. Shaw, J. K. Min, R. Hachamovitch, *et al.*, "Cardiovascular imaging research at the crossroads", *JACC: Cardiovascular Imaging*, vol. 3, no. 3, pp. 316–324, 2010.

[192] E. A. Hulten, S. Carbonaro, S. P. Petrillo, J. D. Mitchell, and T. C. Villines, "Prognostic value of cardiac computed tomography angiography: A systematic review and meta-analysis", *Journal of the American College of Cardiology*, vol. 57, no. 10, pp. 1237–1247, 2011.

[193] D. P. Boyd and M. J. Lipton, "Cardiac computed tomography", *Proceedings of the IEEE*, vol. 71, no. 3, pp. 298–307, 1983.

[194] M. Dewey, M. Siebes, M. Kachelrieß, *et al.*, "Clinical quantitative cardiac imaging for the assessment of myocardial ischaemia", *Nature Reviews Cardiology*, vol. 17, no. 7, pp. 427–450, 2020.

[195] Y. J. Hong, J. Hur, K. Han, *et al.*, "Quantitative analysis of a whole cardiac mass using dual-energy computed tomography: Comparison with conventional computed tomography and magnetic resonance imaging", *Scientific reports*, vol. 8, no. 1, p. 15 334, 2018.

[196] S. J. Buss, F. Schulz, D. Mereles, *et al.*, "Quantitative analysis of left ventricular strain using cardiac computed tomography", *European journal of radiology*, vol. 83, no. 3, e123–e130, 2014.

[197] L. P. Badano, K. Addetia, G. Pontone, *et al.*, "Advanced imaging of right ventricular anatomy and function", *Heart*, vol. 106, no. 19, pp. 1469–1476, 2020.

[198] Y. Song, D. H. Yang, B. Ó Hartaigh, *et al.*, "Geometric predictors of left ventricular outflow tract obstruction in patients with hypertrophic cardiomyopathy: A 3d computed tomography analysis", *European Heart Journal-Cardiovascular Imaging*, vol. 19, no. 10, pp. 1149–1156, 2018.

[199] P. Lambin, R. T. Leijenaar, T. M. Deist, *et al.*, "Radiomics: The bridge between medical imaging and personalized medicine", *Nature reviews Clinical oncology*, vol. 14, no. 12, pp. 749–762, 2017.

[200] T. S. Poltronieri, N. S. de Paula, and G. V. Chaves, "Assessing skeletal muscle radiodensity by computed tomography: An integrative review of the applied methodologies", *Clinical Physiology and Functional Imaging*, vol. 40, no. 4, pp. 207–223, 2020.

[201] B. Sjøblom, B. H. Grønberg, T. Wentzel-Larsen, *et al.*, "Skeletal muscle radiodensity is prognostic for survival in patients with advanced non-small cell lung cancer", *Clinical Nutrition*, vol. 35, no. 6, pp. 1386–1393, 2016.

[202] J. Xiao, B. J. Caan, E. M. C. Feliciano, *et al.*, "Association of low muscle mass and low muscle radiodensity with morbidity and mortality for colon cancer surgery", *JAMA surgery*, vol. 155, no. 10, pp. 942–949, 2020.

[203] C. Hanley, K. J. Shields, K. A. Matthews, *et al.*, "Associations of cardiovascular fat radiodensity and vascular calcification in midlife women: The swan cardiovascular fat ancillary study", *Atherosclerosis*, vol. 279, pp. 114–121, 2018.

[204] S. S. Kwon, K. Choi, B. Da Nam, *et al.*, "Epicardial adipose tissue radiodensity is associated with all-cause mortality in patients undergoing hemodialysis", *Scientific Reports*, vol. 11, no. 1, p. 23 090, 2021.

[205] R. Forni, C. Gelormini, C. Corsi, and P. Gargiulo, "Virtual histology of the heart through ct imaging: Preliminary results of a novel noninvasive approach for cardiac tissue characterization", in *2023 Computing in Cardiology (CinC)*, IEEE, vol. 50, 2023, pp. 1–4.

[206] J. L. van Vugt, R. R. C. van den Braak, H. J. Schippers, *et al.*, "Contrast-enhancement influences skeletal muscle density, but not skeletal muscle mass, measurements on computed tomography", *Clinical Nutrition*, vol. 37, no. 5, pp. 1707–1714, 2018.

[207] M. Cerqueira, N. Weissman, V. Dilsizian, *et al.*, "Standardized myocardial segmentation and nomenclature for tomographic imaging of the heart: A statement for healthcare professionals from the cardiac imaging committee of the council on clinical cardiology of the american heart association", *Circulation*, vol. 105, no. 4, pp. 539–542, 2002.

[208] R. M. Gray, *Entropy and information theory*. Springer Science & Business Media, 2011.

[209] A. Depeursinge, O. S. Al-Kadi, and J. R. Mitchell, *Biomedical texture analysis: fundamentals, tools and challenges*. Academic Press, 2017.

[210] A. J. Moss, M. C. Williams, D. E. Newby, and E. D. Nicol, "The updated nice guidelines: Cardiac ct as the first-line test for coronary artery disease", *Current cardiovascular imaging reports*, vol. 10, pp. 1–7, 2017.

[211] R. Greenbaum, S. Y. Ho, D. Gibson, A. Becker, and R. Anderson, "Left ventricular fibre architecture in man.", *Heart*, vol. 45, no. 3, pp. 248–263, 1981.

[212] S. Kaul, "The interventricular septum in health and disease", *American heart journal*, vol. 112, no. 3, pp. 568–581, 1986.

[213] M. Steenman and G. Lande, "Cardiac aging and heart disease in humans", *Biophysical reviews*, vol. 9, no. 2, pp. 131–137, 2017.

[214] E. G. Lakatta and D. Levy, "Arterial and cardiac aging: Major shareholders in cardiovascular disease enterprises: Part ii: The aging heart in health: Links to heart disease", *Circulation*, vol. 107, no. 2, pp. 346–354, 2003.

[215] D. U. Akasheva, E. V. Plokhova, O. N. Tkacheva, *et al.*, "Age-related left ventricular changes and their association with leukocyte telomere length in healthy people", *PloS one*, vol. 10, no. 8, e0135883, 2015.

[216] P. Elliott and W. J. McKenna, "Hypertrophic cardiomyopathy", *The Lancet*, vol. 363, no. 9424, pp. 1881–1891, 2004.

[217] S. Y. Ho, "Anatomy and myoarchitecture of the left ventricular wall in normal and in disease", *European Journal of Echocardiography*, vol. 10, no. 8, pp. iii3–iii7, 2009.

[218] P. Kong, P. Christia, and N. G. Frangogiannis, "The pathogenesis of cardiac fibrosis", *Cellular and molecular life sciences*, vol. 71, pp. 549–574, 2014.

[219] M. S. Nacif, Y. Liu, J. Yao, *et al.*, "3d left ventricular extracellular volume fraction by low-radiation dose cardiac ct: Assessment of interstitial myocardial fibrosis", *Journal of cardiovascular computed tomography*, vol. 7, no. 1, pp. 51–57, 2013.

[220] A. Yamada, K. Kitagawa, S. Nakamura, *et al.*, "Quantification of extracellular volume fraction by cardiac computed tomography for noninvasive assessment of myocardial fibrosis in hemodialysis patients", *Scientific Reports*, vol. 10, no. 1, p. 15 367, 2020.

[221] C. Carbucicchio, D. Andreini, G. Piperno, *et al.*, "Stereotactic radioablation for the treatment of ventricular tachycardia: Preliminary data and insights from the stra-mi-vt phase ib/ii study", *Journal of Interventional Cardiac Electrophysiology*, vol. 62, pp. 427–439, 2021.

[222] S. Frantz, M. J. Hundertmark, J. Schulz-Menger, F. M. Bengel, and J. Bauersachs, "Left ventricular remodelling post-myocardial infarction: Pathophysiology, imaging, and novel therapies", *European heart journal*, vol. 43, no. 27, pp. 2549–2561, 2022.

[223] A. Ganau, R. B. Devereux, M. J. Roman, *et al.*, "Patterns of left ventricular hypertrophy and geometric remodeling in essential hypertension", *Journal of the American College of Cardiology*, vol. 19, no. 7, pp. 1550–1558, 1992.

[224] B. J. Maron, E. J. Rowin, J. E. Udelson, and M. S. Maron, "Clinical spectrum and management of heart failure in hypertrophic cardiomyopathy", *JACC: Heart Failure*, vol. 6, no. 5, pp. 353–363, 2018.

[225] J. B. Geske, S. R. Ommen, and B. J. Gersh, "Hypertrophic cardiomyopathy: Clinical update", *JACC: heart failure*, vol. 6, no. 5, pp. 364–375, 2018.

[226] S. Jiang, L. Zhang, J. Wang, *et al.*, "Differentiating between cardiac amyloidosis and hypertrophic cardiomyopathy on non-contrast cine-magnetic resonance images using machine learning-based radiomics", *Frontiers in Cardiovascular Medicine*, vol. 9, p. 1 001 269, 2022.

[227] Q. Zhao, Z. Chen, C. Qi, *et al.*, "Cardiac magnetic resonance imaging for discrimination of hypertensive heart disease and hypertrophic cardiomyopathy: A systematic review and meta-analysis", *Frontiers in Cardiovascular Medicine*, vol. 11, p. 1 421 013, 2024.

[228] U. Neisius, H. El-Rewaidy, S. Nakamori, J. Rodriguez, W. J. Manning, and R. Nezafat, "Radiomic analysis of myocardial native t1 imaging discriminates between hypertensive heart disease and hypertrophic cardiomyopathy", *JACC: Cardiovascular Imaging*, vol. 12, no. 10, pp. 1946–1954, 2019.

[229] W.-W. Chen, L. Kuo, Y.-X. Lin, *et al.*, "A deep learning approach to classify fabry cardiomyopathy from hypertrophic cardiomyopathy using cine imaging on cardiac magnetic resonance", *International Journal of Biomedical Imaging*, vol. 2024, no. 1, p. 6 114 826, 2024.

[230] A. S. Fahmy, E. J. Rowin, A. Arafati, T. Al-Otaibi, M. S. Maron, and R. Nezafat, "Radiomics and deep learning for myocardial scar screening in hypertrophic cardiomyopathy", *Journal of Cardiovascular Magnetic Resonance*, vol. 24, no. 1, p. 40, 2022.

[231] A. S. Fahmy, E. J. Rowin, N. Jaafar, *et al.*, "Radiomics of late gadolinium enhancement reveals prognostic value of myocardial scar heterogeneity in hypertrophic cardiomyopathy", *Cardiovascular Imaging*, vol. 17, no. 1, pp. 16–27, 2024.

[232] R. Forni, A. Colacino, B. Punzo, *et al.*, "Virtual cardiac histology: Towards a radiodensitometric characterization of left ventricular cardiac muscle in healthy and pathological conditions", *Available at SSRN 5056628 - under revision*,

[233] S. M. Lundberg and S.-I. Lee, "A unified approach to interpreting model predictions", *Advances in neural information processing systems*, vol. 30, 2017.

[234] M. A. Lemp, G. N. Foulks, *et al.*, "The definition and classification of dry eye disease", *Ocul Surf*, vol. 5, no. 2, pp. 75–92, 2007.

[235] J. A. Clayton, "Dry eye", *New England Journal of Medicine*, vol. 378, no. 23, pp. 2212–2223, 2018.

[236] P. J. Driver and M. A. Lemp, "Meibomian gland dysfunction", *Survey of ophthalmology*, vol. 40, no. 5, pp. 343–367, 1996.

[237] C. Baudouin, "The pathology of dry eye", *Survey of ophthalmology*, vol. 45, S211–S220, 2001.

[238] *Review of optometry*. [Online]. Available: `https://www.reviewofoptometry.com/`.

[239] Y. Deng, Q. Wang, Z. Luo, *et al.*, "Quantitative analysis of morphological and functional features in meibography for meibomian gland dysfunction: Diagnosis and grading", *EClinicalMedicine*, vol. 40, 2021.

[240] F. Fineide, R. Arita, and T. P. Utheim, "The role of meibography in ocular surface diagnostics: A review", *The ocular surface*, vol. 19, pp. 133–144, 2021.

[241] J. Wang, T. N. Yeh, R. Chakraborty, S. X. Yu, and M. C. Lin, "A deep learning approach for meibomian gland atrophy evaluation in meibography images", *Translational vision science & technology*, vol. 8, no. 6, pp. 37–37, 2019.

[242] R. Forni, I. Maruotto, A. Zanuccoli, *et al.*, "Advancing meibography assessment and automated meibomian gland detection using gray value profiles", *Diagnostics*, vol. 15, no. 10, p. 1199, 2025.

[243] J. D. Nelson, J. Shimazaki, J. M. Benitez-del-Castillo, *et al.*, "The international workshop on meibomian gland dysfunction: Report of the definition and classification subcommittee", *Investigative ophthalmology & visual science*, vol. 52, no. 4, pp. 1930–1937, 2011.

[244] K. K. Nichols, G. N. Foulks, A. J. Bron, *et al.*, "The international workshop on meibomian gland dysfunction: Executive summary", *Investigative ophthalmology & visual science*, vol. 52, no. 4, pp. 1922–1929, 2011.

[245] H. Pult, B. H. Riede-Pult, and P. J. Murphy, "The relation between blinking and conjunctival folds and dry eye symptoms", *Optometry and Vision Science*, vol. 90, no. 10, pp. 1034–1039, 2013.

[246] J. D. Sheppard and K. K. Nichols, "Dry eye disease associated with meibomian gland dysfunction: Focus on tear film characteristics and the therapeutic landscape", *Ophthalmology and therapy*, vol. 12, no. 3, pp. 1397–1418, 2023.

[247] Y.-S. Yoo, K.-S. Na, Y.-S. Byun, *et al.*, "Examination of gland dropout detected on infrared meibography by using optical coherence tomography meibography", *The ocular surface*, vol. 15, no. 1, pp. 130–138, 2017.

[248] Y. Wang, F. Shi, S. Wei, and X. Li, "A deep learning model for evaluating meibomian glands morphology from meibography", *Journal of Clinical Medicine*, vol. 12, no. 3, p. 1053, 2023.

[249] H. Zhang and Y. Qie, "Applying deep learning to medical imaging: A review", *Applied Sciences*, vol. 13, no. 18, p. 10 521, 2023.

[250] T. M. Buzug, "Computed tomography", in *Springer handbook of medical technology*, Springer, 2011, pp. 311–342.

[251] J. F. Schenck, "The role of magnetic susceptibility in magnetic resonance imaging: Mri magnetic compatibility of the first and second kinds", *Medical physics*, vol. 23, no. 6, pp. 815–850, 1996.

[252] F. Angelone, F. K. Ciliberti, G. P. Tobia, *et al.*, "Innovative diagnostic approaches for predicting knee cartilage degeneration in osteoarthritis patients: A radiomics-based study", *Information Systems Frontiers*, pp. 1–23, 2024.

[253] R. Aubonnet, J. Ramos, M. Recenti, *et al.*, "Toward new assessment of knee cartilage degeneration", *Cartilage*, vol. 14, no. 3, pp. 351–374, 2023.

[254] T. S. Poltronieri, N. S. de Paula, and G. V. Chaves, "Assessing skeletal muscle radiodensity by computed tomography: An integrative review of the applied methodologies", *Clinical Physiology and Functional Imaging*, vol. 40, no. 4, pp. 207–223, 2020.

[255] K. Edmunds, M. Gíslason, S. Sigurðsson, *et al.*, "Advanced quantitative methods in correlating sarcopenic muscle degeneration with lower extremity function biometrics and comorbidities", *PloS one*, vol. 13, no. 3, e0193241, 2018.

[256] C. Ricciardi, K. J. Edmunds, M. Recenti, *et al.*, "Assessing cardiovascular risks from a mid-thigh ct image: A tree-based machine learning approach using radiodensitometric distributions", *Scientific reports*, vol. 10, no. 1, p. 2863, 2020.

[257] R. M. Schiffman, M. D. Christianson, G. Jacobsen, J. D. Hirsch, and B. L. Reis, "Reliability and validity of the ocular surface disease index", *Archives of ophthalmology*, vol. 118, no. 5, pp. 615–621, 2000.

[258] G. Giannaccare, M. Pellegrini, G. C. Scalzo, M. Borselli, D. Ceravolo, and V. Scorcia, "Low-level light therapy versus intense pulsed light for the treatment of meibomian gland dysfunction: Preliminary results from a prospective randomized comparative study", *Cornea*, vol. 42, no. 2, pp. 141–144, 2023.

[259] K. L. Miller, J. G. Walt, D. R. Mink, *et al.*, "Minimal clinically important difference for the ocular surface disease index", *Archives of ophthalmology*, vol. 128, no. 1, pp. 94–101, 2010.

[260] E. W. Dijkstra, "A note on two problems in connexion with graphs", in *Edsger Wybe Dijkstra: his life, work, and legacy*, 2022, pp. 287–290.

[261] M. A. K. Setu, J. Horstmann, S. Schmidt, M. E. Stern, and P. Steven, "Deep learning-based automatic meibomian gland segmentation and morphology assessment in infrared meibography", *Scientific reports*, vol. 11, no. 1, p. 7649, 2021.

[262] K. He, G. Gkioxari, P. Dollár, and R. Girshick, "Mask r-cnn", in *Proceedings of the IEEE international conference on computer vision*, 2017, pp. 2961–2969.

[263] N. Ouyang, W. Wang, L. Ma, *et al.*, "Diagnosing acute promyelocytic leukemia by using convolutional neural network", *Clinica chimica acta*, vol. 512, pp. 1–6, 2021.

[264] G. A. Truskey, "The potential of deep learning to advance clinical applications of computational biomechanics", *Bioengineering*, vol. 10, no. 9, p. 1066, 2023.

[265] Í. Árnadóttir, R. Forni, I. Ólafsson, D. Jacob, and P. Gargiulo, "3d printing to advance neurosurgery planning", in *Handbook of Surgical Planning and 3D Printing*, Elsevier, 2023, pp. 125–141.

[266] R. Forni, S. Agnarsdóttir, B. Torfason, and P. Gargiulo, "Heart surgery: Septal defect", in *Handbook of Surgical Planning and 3D Printing*, Elsevier, 2023, pp. 143–169.

[267] Z. Deng, N. Xiang, and J. Pan, "State of the art in immersive interactive technologies for surgery simulation: A review and prospective", *Bioengineering*, vol. 10, no. 12, p. 1346, 2023.

[268] E. Toni, E. Toni, M. Fereidooni, and H. Ayatollahi, "Acceptance and use of extended reality in surgical training: An umbrella review", *Systematic Reviews*, vol. 13, no. 1, pp. 1–28, 2024.

[269] T. Punyaratabandhu, P. C. Liacouras, and S. Pairojboriboon, "Using 3d models in orthopedic oncology: Presenting personalized advantages in surgical planning and intraoperative outcomes", *3D printing in medicine*, vol. 4, pp. 1–13, 2018.

[270] M. B. Shenai, M. Dillavou, C. Shum, *et al.*, "Virtual interactive presence and augmented reality (vipar) for remote surgical assistance", *Operative Neurosurgery*, vol. 68, ons200–ons207, 2011.

[271] M. Zhou, J. Scott, B. Chaudhury, *et al.*, "Radiomics in brain tumor: Image assessment, quantitative feature descriptors, and machine-learning approaches", *American Journal of Neuroradiology*, vol. 39, no. 2, pp. 208–216, 2018.

[272] R. W. Granzier, N. M. Verbakel, A. Ibrahim, *et al.*, "Mri-based radiomics in breast cancer: Feature robustness with respect to inter-observer segmentation variability", *scientific reports*, vol. 10, no. 1, p. 14 163, 2020.

[273] C. Parmar, E. Rios Velazquez, R. Leijenaar, *et al.*, "Robust radiomics feature quantification using semiautomatic volumetric segmentation", *PloS one*, vol. 9, no. 7, e102107, 2014.

[274] A. Rodríguez-Ruiz, E. Krupinski, J.-J. Mordang, *et al.*, "Detection of breast cancer with mammography: Effect of an artificial intelligence support system", *Radiology*, vol. 290, no. 2, pp. 305–314, 2019.

[275] D. Wang, A. Khosla, R. Gargeya, H. Irshad, and A. H. Beck, "Deep learning for identifying metastatic breast cancer", *arXiv preprint arXiv:1606.05718*, 2016.

[276] M. Z. Alom, C. Yakopcic, M. Hasan, T. M. Taha, and V. K. Asari, "Recurrent residual u-net for medical image segmentation", *Journal of medical imaging*, vol. 6, no. 1, pp. 014 006–014 006, 2019.

[277] A. Akter, N. Nosheen, S. Ahmed, *et al.*, "Robust clinical applicable cnn and u-net based algorithm for mri classification and segmentation for brain tumor", *Expert Systems with Applications*, vol. 238, p. 122 347, 2024.

[278] N. Zakaria, F. Mohamed, R. Abdelghani, and K. Sundaraj, "Three resnet deep learning architectures applied in pulmonary pathologies classification", in *2021 International Conference on Artificial Intelligence for Cyber Security Systems and Privacy (AI-CSP)*, IEEE, 2021, pp. 1–8.

[279] A. Riasatian, M. Babaie, D. Maleki, *et al.*, "Fine-tuning and training of densenet for histopathology image representation using tcga diagnostic slides", *Medical image analysis*, vol. 70, p. 102 032, 2021.

[280] I. D. Apostolopoulos, S. Aznaouridis, and M. Tzani, "An attention-based deep convolutional neural network for brain tumor and disorder classification and grading in magnetic resonance imaging", *Information*, vol. 14, no. 3, p. 174, 2023.

[281] K. Armanious, C. Jiang, M. Fischer, *et al.*, "Medgan: Medical image translation using gans", *Computerized medical imaging and graphics*, vol. 79, p. 101 684, 2020.

[282] F. Knoll, J. Zbontar, A. Sriram, *et al.*, "Fastmri: A publicly available raw k-space and dicom dataset of knee images for accelerated mr image reconstruction using machine learning", *Radiology: Artificial Intelligence*, vol. 2, no. 1, e190007, 2020.

[283] S. Farahmand, O. Shabestari, M. Pakrah, H. Hossein-Nejad, M. Arbab, and S. Bagheri-Hariri, "Artificial intelligence-based triage for patients with acute abdominal pain in emergency department; a diagnostic accuracy study", *Advanced journal of emergency medicine*, vol. 1, no. 1, e5, 2017.

[284] R. A. Taylor, C. Chmura, J. Hinson, *et al.*, "Impact of artificial intelligence–based triage decision support on emergency department care", *NEJM AI*, vol. 2, no. 3, AIoa2400296, 2025.

[285] Z. Liu, Y. Li, P. Shu, *et al.*, "Radiology-gpt: A large language model for radiology", *Meta-Radiology*, p. 100 153, 2025.

[286] Z. Liu, A. Zhong, Y. Li, *et al.*, "Tailoring large language models to radiology: A preliminary approach to llm adaptation for a highly specialized domain", in *International workshop on machine learning in medical imaging*, Springer, 2023, pp. 464–473.

[287] N. Arun, N. Gaw, P. Singh, *et al.*, "Assessing the trustworthiness of saliency maps for localizing abnormalities in medical imaging", *Radiology: Artificial Intelligence*, vol. 3, no. 6, e200267, 2021.

[288] M. Reyes, R. Meier, S. Pereira, *et al.*, "On the interpretability of artificial intelligence in radiology: Challenges and opportunities", *Radiology: artificial intelligence*, vol. 2, no. 3, e190043, 2020.

[289] J.-Z. Cheng, D. Ni, Y.-H. Chou, *et al.*, "Computer-aided diagnosis with deep learning architecture: Applications to breast lesions in us images and pulmonary nodules in ct scans", *Scientific reports*, vol. 6, no. 1, p. 24 454, 2016.

[290] R. Gargeya and T. Leng, "Automated identification of diabetic retinopathy using deep learning", *Ophthalmology*, vol. 124, no. 7, pp. 962–969, 2017.

[291] Y. Akhter, R. Singh, and M. Vatsa, "Ai-based radiodiagnosis using chest x-rays: A review", *Frontiers in big data*, vol. 6, p. 1 120 989, 2023.

[292] T. Jorg, M. C. Halfmann, F. Stoehr, *et al.*, "A novel reporting workflow for automated integration of artificial intelligence results into structured radiology reports", *Insights into Imaging*, vol. 15, no. 1, p. 80, 2024.

[293] Y. Ming, X. Dong, J. Zhao, Z. Chen, H. Wang, and N. Wu, "Deep learning-based multimodal image analysis for cervical cancer detection", *Methods*, vol. 205, pp. 46–52, 2022.

[294] K. Parodi, T. Yamaya, and P. Moskal, "Experience and new prospects of pet imaging for ion beam therapy monitoring", *Zeitschrift für Medizinische Physik*, vol. 33, no. 1, pp. 22–34, 2023.

[295] J. Dana, V. Agnus, F. Ouhmich, and B. Gallix, "Multimodality imaging and artificial intelligence for tumor characterization: Current status and future perspective", in *Seminars in nuclear medicine*, Elsevier, vol. 50, 2020, pp. 541–548.

[296] Z. Guo, X. Li, H. Huang, N. Guo, and Q. Li, "Deep learning-based image segmentation on multimodal medical imaging", *IEEE Transactions on Radiation and Plasma Medical Sciences*, vol. 3, no. 2, pp. 162–169, 2019.

[297] J. P. O'Connor, A. Jackson, M.-C. Asselin, D. L. Buckley, G. J. Parker, and G. C. Jayson, "Quantitative imaging biomarkers in the clinical development of targeted therapeutics: Current and future perspectives", *The lancet oncology*, vol. 9, no. 8, pp. 766–776, 2008.

[298] S. Rodrigues-Ferreira and C. Nahmias, "Predictive biomarkers for personalized medicine in breast cancer", *Cancer Letters*, vol. 545, p. 215 828, 2022.

[299] M. D. Sugi, T. A. Kennedy, V. Shah, and M. P. Hartung, "Bridging the gap: Interactive, case-based learning in radiology education", *Abdominal radiology*, vol. 46, no. 12, pp. 5503–5508, 2021.

[300] V. Kumar and C. C. Gadbury-Amyot, "A case-based and team-based learning model in oral and maxillofacial radiology", *Journal of dental education*, vol. 76, no. 3, pp. 330–337, 2012.

[301] M. Bazelmans, N. C. Peters, A. H. Koning, A. J. Eggink, and T. E. Cohen-Overbeek, "Power doppler rendering of fetal bilateral accessory renal arteries in virtual reality", *Ultrasound Obstet Gynecol*, vol. 44, no. 3, pp. 375–376, 2014.

[302] R. N. Uppot, B. Laguna, C. J. McCarthy, *et al.*, "Implementing virtual and augmented reality tools for radiology education and training, communication, and clinical care", *Radiology*, vol. 291, no. 3, pp. 570–580, 2019.

[303] R. Galvez, R. C. Wallon, L. Shackelford, J. R. Amos, and J. L. Rowen, "Use of virtual reality to educate undergraduate medical students on cardiac peripheral and collateral circulation", *Medical Science Educator*, vol. 31, pp. 19–22, 2021.

[304] J. S. Ruthberg, G. Tingle, L. Tan, *et al.*, "Mixed reality as a time-efficient alternative to cadaveric dissection", *Medical teacher*, vol. 42, no. 8, pp. 896–901, 2020.

[305] G. Baratz, P. S. Sridharan, V. Yong, C. Tatsuoka, M. A. Griswold, and S. Wish-Baratz, "Comparing learning retention in medical students using mixed-reality to supplement dissection: A preliminary study", *International Journal of Medical Education*, vol. 13, p. 107, 2022.

[306] K. E. Brown, N. Heise, C. M. Eitel, *et al.*, "A large-scale, multiplayer virtual reality deployment: A novel approach to distance education in human anatomy", *Medical Science Educator*, vol. 33, no. 2, pp. 409–421, 2023.

[307] M. H. Kurniawan, G. Witjaksono, *et al.*, "Human anatomy learning systems using augmented reality on mobile application", *Procedia Computer Science*, vol. 135, pp. 80–88, 2018.

[308] F. Collado-Mesa, E. Alvarez, and K. Arheart, "The role of artificial intelligence in diagnostic radiology: A survey at a single radiology residency training program", *Journal of the American College of Radiology*, vol. 15, no. 12, pp. 1753–1757, 2018.

[309] F. Schuur, M. H. Rezazade Mehrizi, and E. Ranschaert, "Training opportunities of artificial intelligence (ai) in radiology: A systematic review", *European radiology*, vol. 31, pp. 6021–6029, 2021.

Department of Engineering, School of Technology
Reykjavík University
Menntavegur 1
102 Reykjavík, Iceland
Tel. +354 599 6200
Fax +354 599 6201
www.ru.is
ISBN: 978-9935-539-91-5 Electronic version
ISBN: 978-9935-539-90-8 Print version

ORCID Riccardo Forni
https://orcid.org/0000-0003-1297-6134